ACOUSTO-OPTIC LENS MICROSCOPY

MODELLING AND DEVELOPMENT

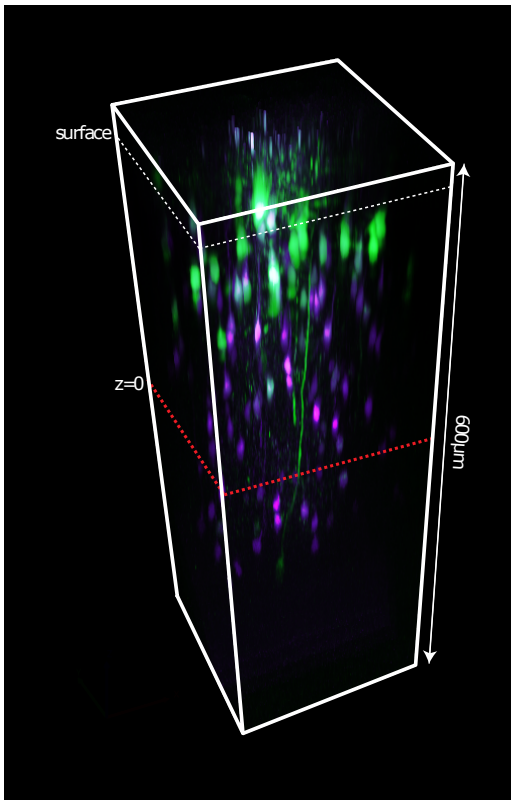

Geoffrey J. Evans

Neuroscience, Physiology and Pharmacology
University College London
2016

Ph.D. Thesis

Modelling and Development of Acousto-Optic Lens Microscopy

Geoffrey J. Evans

Ph.D. Thesis, University College London, 2016

SUPERVISORS:
R. Angus Silver
Paul A. Kirkby

DECLARATION

I, Geoffrey J. Evans, confirm that the work presented in this thesis is my own. Where information has been derived from other sources, I confirm that this has been indicated in the work.

ABSTRACT

Understanding how sensory information is processed in neural networks would mark a great leap forward for neuroscience. This has sparked a race to develop new technologies for performing 3D *in-vivo* brain imaging at high spatio-temporal resolution.

A spherical acousto-optic lens (AOL) consisting of four acousto-optic deflectors (AODs) can rapidly steer and focus the laser beam of a two-photon microscope in 3D space. AOLs use acoustic waves to deflect and focus an optical beam, enabling fast random-access imaging. This is well-suited to measuring sparsely-distributed brain activity using fluorescent reporter dyes. However, to date AOL-based imaging has been performed using only linearly-chirped acoustic frequency drives. Here I develop new wavefront propagation theory and demonstrate AOL microscope imaging using nonlinearly-chirped drives for the first time. Nonlinear drives enable focal trajectories to be more closely fitted to structures of interest, offering new approaches to high-speed imaging of neuronal structures.

A complete theoretical description of light propagation through an AOL has been missing, with only simplified principles to guide AOL design. To address this, I develop ray and wave models of optical transmission through an AOL. Using a ray model, I examine transmission efficiency and optimise the size of an AOL microscope's imaging volume. With a wave-based model, I show an alternative design of AOL using six AODs (6-AOD AOL) can theoretically correct spherical aberration, which is a major limitation of AOL microscopes. I further derive the drive equations needed by a 6-AOD AOL for basic microscope operation, opening the possibility of high-speed 3D deep-tissue imaging with diffraction limited resolution.

PUBLICATIONS

Most of Chapters 3 and 4 have been published in [1]. Some of Chapter 4 is currently under consideration in [2]. Parts of Chapters 6 and 8 have been published in [3].

Open source software described in Chapter 4 is available at [4] and in Chapter 8 at [5].

Permissions have been granted for all figures and tables reproduced in this thesis from published works.

ACKNOWLEDGMENTS

I am thankful to those I have worked with in the Silver Lab at UCL for their assistance and guidance over the past three years. My supervisors Prof. R. A. Silver and Dr. P. A. Kirkby have focused my attention on the key challenges in acousto-optic lens development, and their enthusiasm has motivated me throughout my PhD. The time and effort Dr. B. Marin has spent assisting me whilst working on his own separate project has gone beyond all reasonable expectations and for this I am very grateful. Many others in the lab are directly involved in the development of acousto-optic lens microscopes and their expertise has helped me along the way. Outside the lab, I thank my parents and my wife-to-be Tanya for their support and encouragement.

CONTENTS

LIST OF FIGURES

LIST OF TABLES

LISTINGS

ACRONYMS AND ABBREVIATIONS

3D-RAMP	RAMP excitation in 3D space
AOL	acousto-optic lens
AOD	acousto-optic deflector
ChR2	channelrhodopsin-2
DMD	digital micromirror device
EEG	electroencephalography
FFT	fast Fourier transform
FPGA	field-programmable gate array
FWHM	full-width at half-maximum
galvo	mirror galvanometer
LC-SLM	liquid crystal spatial light modulator
PMT	photo-multiplier tube
PSF	point spread function
RAMP	random access multi-photon
RF	radio frequency
TeO_2	paratellurite
xy	lateral
z	axial

Part I

INTRODUCTION

1 MICROSCOPY IN THE NEUROSCIENCES

1.1 A BRIEF HISTORY

Progress in neuroscience has been driven by the development of novel methods and improved instrumentation [6]. It was Golgi's *black reaction* that enabled the complete structure of neurons to be observed under a microscope for the first time at the end of the nineteenth century [7] and Golgi's contemporary, Cajal, who championed the neuron doctrine as the functional interpretation of their structure [8].

Further advancements in neuroscience came from the emergence of electrophysiology in the second quarter of the twentieth century, in which experiments involved electrical recordings from single nerve fibres and large-scale measurements of nervous system activity [6]. Hodgkin and Huxley used micro-electrodes to measure action potentials in individual giant axons of squids [9], leading to the Hodgkin-Huxley model [10], a cornerstone of theoretical and computational neuroscience [11]. In all their experiments, a microscope was needed in order to visualise the cells but the experimental data was derived from electrical, rather than optical, recordings. On the other hand, Berger, having invented electroencephalography (EEG), discovered spontaneous electrical activity in the human brain which he associated with the nervous system [12]. In these large-scale-aggregate measurements, no optical methods were used.

A step improvement in microscopy arrived at the end of the fifties with the invention of the confocal microscope [14]. The confocal microscope offered far superior axial optical sectioning than a conventional wide-field microscope that used a digital camera to record images frame-by-frame. Optical sectioning was achieved in a confocal microscope by using descanned detection illustrated in Fig. 1.1: collected light is filtered by a pinhole to pass only ballistic photons originating from the chosen focal plane in the sample [15]. This enabled far better image resolution, particularly for highly-scattering samples such as the brain [16]. The confocal microscope proved to be well-suited to imaging biological samples [17] and soon evolved to become a high-speed laser-scanning microscope [18].

With the introduction of fluorescent dyes in the seventies, light microscopy began its return to the forefront of research in neurophysiology. The demonstration of all-optical measurements of action potentials was first reported in 1973 using voltage-sensitive merocyanine dye [19]. The performance of voltage-sensitive dyes was found to vary depending on their environment so more robust calcium-

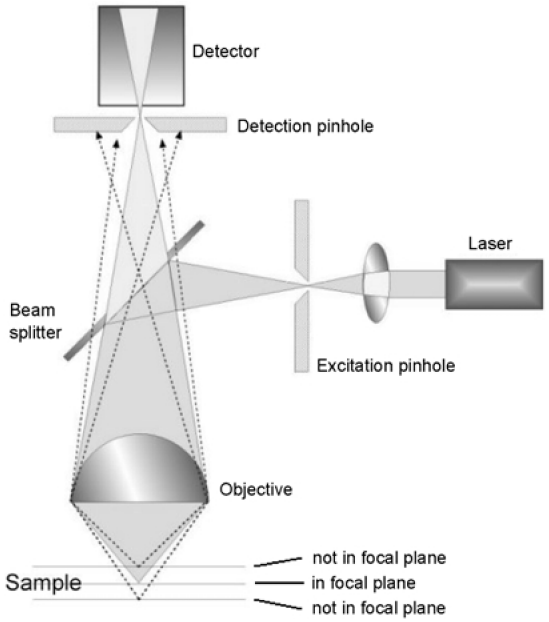

Figure 1.1: The confocal principle with spot illumination and spot observation for fluorescence light. The excitation light (produced by the laser, dark grey) is focused onto a small aperture, the excitation pinhole, by a first lens. The beam splitter directs the light emerging from this pinhole towards the sample. The objective focuses the light onto the specimen. The fluorescent light emitted by the sample (light grey) passes through the beam splitter due to the fact that its wavelength is longer than of the excitation light. The emission is focused onto the detection pinhole. Only light that passes the aperture finally reaches the detector. This light is derived only from the focal plane. All out-of-focus light is suppressed by the detection pinhole. (Reproduced from [13])

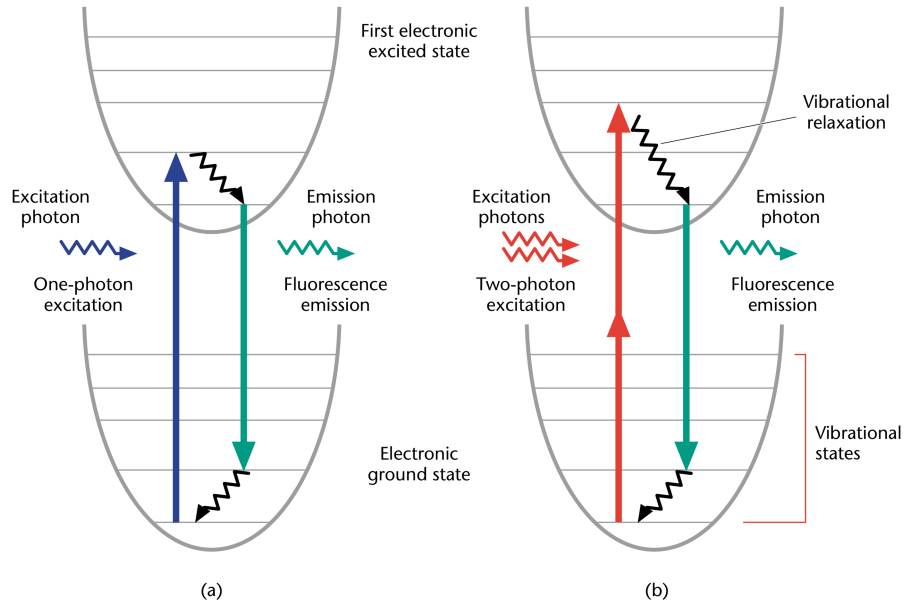

Figure 1.2: Jablonski diagram for one-photon (a) and two-photon (b) excitation. Excitations occur between the ground state and the vibrational levels of the first electronic excited state. One-photon excitation occurs through the absorption of a single photon. The initial and final states have opposite parity. Two-photon excitation occurs through the absorption of two lower-energy photons via short-lived intermediate states. The initial and final states have the same parity. After either excitation process, the fluorophore relaxes to the lowest energy level of the first excited electronic states via vibrational processes. The subsequent fluorescence emission processes for both relaxation modes are the same. (Reproduced from [26])

sensitive dyes were used to indirectly infer action potentials [20]. Dyes were loaded into the target cells by either direct injection or diffusion of membrane-permeable forms [21, 22]. Alternatively, cells could be made to synthesize fluorescent proteins [23]. Genes coding for fluorescent proteins can be inserted in neurons via viral transduction or they can be integrated into the genome of animals to produce transgenic lines. By the turn of the millennium, genetic encoding not only offered effective delivery of fluorescent probes for observing neuronal activity but also enabled cell-type specific targeting [24, 25].

New technology to compete with and in many ways out-perform confocal microscopes arrived with the nineties in the form of multi-photon microscopy [27]. Multi-photon microscopy involves a fluorescent process where two or more photons are absorbed by a fluorophore and a single photon is emitted of shorter wavelength. A Jablonski diagram is shown in Fig. 1.2 highlighting the difference between one-photon and two-photon excitation. A key benefit of two-photon excitation is intrinsic optical sectioning as shown in Fig. 1.3. This is because two-photon excitation is proportional to the fourth

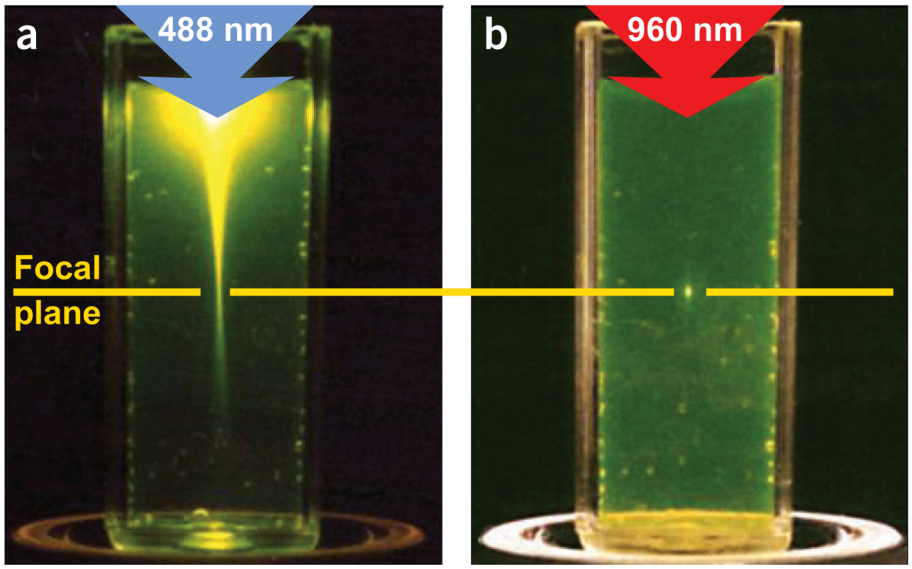

Figure 1.3: Localization of excitation by two-photon excitation. (a) Single-photon excitation of fluorescein by focused 488-nm light (0.16 NA). (b) Two-photon excitation using focused (0.16 NA) femtosecond pulses of 960-nm light. (Reproduced from [28])

power of optical field (intensity squared) rather than the square of the optical field (intensity) as for one-photon excitation.

The intrinsic optical sectioning of two-photon excitation means that the descanned detection used in confocal microscopes is unnecessary. Instead, non-descanned detection is used [29]: points in the sample are illuminated sequentially and the detected photons can be unambiguously associated with spot under illumination at their time of detection. This improves the signal to noise ratio and imaging depth since scattered photons can be included in the signal, whereas they would be blocked by the pinhole in descanned detection. In addition to intrinsic optical sectioning, two-photon excitation uses longer wavelengths than the corresponding one-photon process, allowing infrared wavelengths to be used. Infrared light is less scattered in biological tissue increasing the imaging depth further and is less photo-toxic [30]. The commercial availability of femtosecond lasers from 1996 sparked a dramatic increase in publications involving two-photon microscopy for biological imaging [28]. However, the adoption has not been so widespread, possibly because femtosecond lasers remain prohibitively expensive.

Further expansion of optical capabilities came during the noughties when optical activation of neurons was realised both indirectly and directly. Indirect activation could be achieved, for example, by optically uncaging ligands in the presence of a ligand-gated ion channel [31]. Direct activation of photo-sensitive ion channels with millisecond time-resolution was first achieved using channelrhodopsin-2 (ChR2) [32–34]. A large number of channelrhodopsin variants have

been developed [35] making it possible in this decade to optically activate different sets of neurons independently [36]. Thus, the potential for all-optical replication of electrophysiological experiments was realised and photophysiology was born: microscopes were not only able to identify neurons on a large scale but also induce and detect neuronal excitations, see [37] for example. New microscope designs were needed, capable of exploiting these developments in full [38].

A common limitation of wide-field, confocal and two-photon microscopes is the trade-off between spatial and temporal resolution. This has prevented direct investigation of how sensory information is distributed and processed in 3D space. In order to examine tens or hundreds of neurons concurrently as a single neural circuit [6], it was necessary to develop more powerful microscopes capable of imaging with both high spatial and temporal resolution. The past twenty years has seen a plethora of new designs, the mainstream of which are addressed in Section 1.2.

1.2 FUNCTIONAL MICROSCOPY

This thesis is focussed on the development of functional microscopy: microscopes primarily designed to image time-dependent signals in morphologically complex biological samples rather than their static physiological structures. In this Section I describe the present state of the field and the different approaches used to perform functional imaging.

1.2.1 *Laser scanning microscopy*

In laser scanning microscopy the focused beam of a laser is moved across a sample, which is typically fluorescent. At each time increment, the illuminated spot emits fluorescence, which is collected by the microscope to produce an image. A laser scanning microscope is almost always confocal or two-photon, since these use commercially available technology and achieve good resolution.

The conventional method to perform laser scanning microscopy is to use an orthogonal pair of mirror galvanometer (galvo) scanners. The orthogonal galvos scan the laser through a 2D slice of the sample to produce a complete 2D image. Typical galvos with a 10 mm aperture can reach line-scanning rates of 1 kHz [39] where the speed is limited by inertia. Thus, a galvo with a smaller aperture is faster than if it had a large aperture, all else being equal. A 3D image can be formed by combining a set of 2D images taken at different axial positions. Changing axial position is typically slow, often achieved using a piezo-mounted objective. However, this is not necessarily a problem because axial position only needs changing at the rate at which entire

2D images are acquired. The major advantage of galvo scanners is their wide and affordable commercial availability [39].

An issue with a standard galvo system is that functional events (calcium signals) can be fast and the temporal resolution is not high enough to sample them sufficiently. In order to increase the temporal resolution, faster scanners can be used. Images are often produced by raster scanning where lines in the x-direction are imaged sequentially at consecutive y-positions. Therefore a fast scanner is often used for the x-axis and a normal galvo is used for the y-axis. Fast scanners used for this purpose include resonant galvanometers with effective line-scanning speeds (double their resonant frequencies) of 16 kHz [40, 41], 24 kHz or 32 kHz [42], and polygonal mirrors (25 kHz) [43]. Resonant galvos and polygonal mirrors both necessarily operate at close to their resonant frequency.

1.2.2 *Lightsheet microscopy*

Lightsheet microscopy achieves optical sectioning by only illuminating a thin axial slice of the sample [44]. Unlike laser scanning microscopes which acquire image data point-by-point, lightsheet microscopes can image entire planes concurrently with a digital camera. This confers them with very fast acquisition speeds for imaging full-frame volumes [45]. Lightsheet microscopy has been used to image entire zebrafish brains at cellular resolution with acquisition rates of 0.8 Hz for the complete volume [46]. The field of view of lightsheet microscopes can be further increased by a factor of ten by using an Airy beam for illumination rather than the conventional Gaussian beam [47]. However, it is not possible to use a lightsheet microscope to image much larger and more scattering samples because it uses two orthogonal objectives (one for illumination and one for acquisition) and the lightsheet must permeate through the entire region to be imaged. This precludes it from being used on large living mammalian specimens, for example mice.

An epi-fluorescent adaption of lightsheet microscopy known as SCAPE [48] has been developed to enable fast *in vivo* volumetric imaging of larger samples using a single objective for both acquisition and orthogonal illumination. To achieve this, one side of the objective is used for illumination and the opposite side for acquisition. Volume acquisition rates of 10-24 Hz have been demonstrated at depths of up to 1 mm. However, the depth and resolution are still poorer than for a two-photon microscope. Although lightsheet provides good axial sectioning, the use of a camera to collect all pixels in a frame concurrently means that scattered photons contribute to noise instead of signal, unlike in a two-photon laser scanning microscope. Furthermore, despite the impressive frame acquisition speeds demonstrated using lightsheet microscopy, the volumetric imaging rates are still not suffi-

cient to guarantee that every neuronal signal that may be of interest in 3D space is detected.

1.2.3 *Selective 3D imaging*

One approach for laser scanning microscopes to reach higher functional imaging speeds to compete with lightsheet microscopes is to selectively image only a subset of the available volume. Much of the data collected in full-frame volume images is redundant because regions of interest are often spatially sparse. By efficiently moving between regions of interest, all relevant information can be acquired from a small fraction of the full-frame volume and functional imaging speeds can be increased by orders of magnitude. Similarly, the amount of data acquired is reduced, easing processing and future storage.

When selectively imaging regions of interest in 3D space, axial scan speed becomes much more important. A simple means of changing the axial focal position is to use a piezo-mounted objective. The motion of galvos can be synchronised with the piezo-mounted objective to scan a laser beam over intricate continuous trajectories through regions of interest (Lissajous curves for example) [49]. Axial scan speeds of 10 Hz have been achieved using this method [49]. Faster axial scan speeds can be achieved using non-mechanical means of moving the focus. An electrically-tunable lens was reported to achieve 30 Hz [50] axially, though this is still far slower than the galvos used for lateral scanning.

A further issue with the electrically-tunable lens was that of spherical aberration arising when focusing away from the front-focal plane of the objective (remote focusing) [50]. This is a well-known issue common to most remote focusing microscopes [51]. By careful design, a remote focusing method has been developed which avoids spherical aberration. Two matched microscope objectives and an oscillating mirror are used to achieve scanning rates of 2.7 kHz and an axial range of 200 μm [52]. In the focal plane of the first objective, the mirror oscillates axially at high-speed. In the simplest configuration, displacing the mirror in the focal region of the first objective by a particular distance displaces the the focal position of the second objective by twice the particular distance. Thus the focal position is related linearly to the mirror's axial position. This system enables comparable axial and lateral speeds and is therefore well-suited to selective 3D imaging of regions of interest. Very similar aberration-free methods have been reported based on this design [53].

1.2.4 *Random access imaging*

Whilst selectively imaging subsets of full-frame volumes can significantly increase acquisition speeds, continuously scanning will still waste imaging time travelling between regions of interest. Neuronal imaging requires rapidly and repeatedly shifting focus between small regions of interest separated by relatively large distances. Ideally then the focal spot would jump from point to point instantaneously without spending time in-between. Such a microscope can be described as random access since the ordering in which the points of interest are imaged makes no difference to the acquisition speed.

A random access multi-photon (RAMP) microscope can be made using a pair of orthogonal acousto-optic deflectors [54–56]. An acousto-optic deflector (AOD) is a crystal aperture with a continuous ultrasound acoustic wave propagating across it. Laser beam deflection is achieved via interaction between the light and the sound in the crystal, and the deflection angle is determined precisely by the optic and acoustic wavevectors. Such an AOD-based RAMP microscope rapidly moves the laser focus between points of interest by changing the frequency of the acoustic waves propagating across each AOD. The shifting is limited by the time taken for acoustic waves to propagate across the AOD apertures, known as the fill time. Thus, AOD-based RAMP microscopes achieve speeds in the region of $40/N$ kHz when imaging N points of interest.

For some experiments, it may be desirable to use confocal instead of two-photon microscopy because it supports a wider optical bandwidth (from near infrared to ultraviolet) and a larger range of fluorescent indicators. In these cases, a digital micromirror device (DMD) can be used as virtual pinhole arrays for random-access confocal microscopy [57]. Such a microscope has a high temporal resolution and can visit 20–40 spatially distributed points of interest at speeds of 0.5–1 kHz. Another benefit of confocal microscopy is that it is very affordable. However, two-photon microscopy offers greater imaging depth, reduced photo-bleaching and better signal, and is therefore the focus of this thesis.

For the AOD and DMD microscopes discussed so far, random access is constrained to points lying in a plane rather than a volume. It has been shown that two AODs aligned to have counter-propagating acoustic waves can behave as a cylindrical lens when the AODs are driven with linear chirps (acoustic frequency changes linearly with time) [58]. Such a configuration is known as a cylindrical acousto-optic lens (AOL). Two orthogonal cylindrical AOLs (four AODs in total) can behave as a spherical lens, and is analogously called a spherical AOL. An AOL microscope can thus perform RAMP excitation in 3D space (3D-RAMP) [59–63]. Because the physical mechanism is the

same, a spherical AOL can perform 3D-RAMP at the same speed as an orthogonal pair of AODs can perform RAMP in 2D.

Only two orthogonal AODs driven with chirped frequencies are needed for a 3D-RAMP microscope if time-locked single-laser-pulse illumination is used. Each of the two orthogonal AODs can modulate the laser pulses with an arbitrary 1D phase pattern [64, 65]. The single-laser-pulse illumination is required to 'freeze' the acoustic waves (and thus the phase patterns) as they propagate across the AODs: because the speed of light is much faster than that of acoustic waves, the laser-pulse effectively encounters a fixed diffraction grating at each AOD. A liquid crystal spatial light modulator (LC-SLM) might sound suitable for this task [66]. However, the speed of present liquid crystal technology is too slow for them to be used like AODs: refresh rates are typically under 300 Hz and certainly do not exceed 1 kHz (for example see OverDrive Plus [67]).

The single-laser-pulse AOD illumination method has been successfully used to manipulate optical wavefronts, including adding curvature as needed for 3D-RAMP. Whilst the strobing method avoids the complication of acoustic waves propagating across the AODs [68], it requires a pause between each pulse of at least an entire AOD fill time (the time for the acoustic wave to cross the crystal aperture). This limits point acquisition rate to the AOD fill rate, much like an AOD in a lateral scanning unit using constant acoustic frequencies. Higher speeds can be achieved with smaller crystals but this comes at the cost of a lower resolution (or more precisely the *number of resolvable points* [68]). Although very promising, 3D-RAMP has not yet been demonstrated on biological samples using this method.

Whilst random access microscopes are fast for imaging a small number of points, a key limitation is that acquiring full-frame images can take seconds and volumes can take minutes. This is problematic for *in vivo* imaging when there is movement. When spatially distributed points are imaged in isolation, the microscope user has no knowledge of the their surroundings. Without this contextual data (which is not of scientific interest itself) it is difficult to determine whether the sample has moved, and in the event that the sample does move the collected data is of no use.

1.2.5 *High-speed two-photon imaging*

To overcome the issue of moving samples faced by random access microscopes, laser scanning microscopes have been developed to image areas and volumes at high-speed. Whilst AODs have been used for (3D-)RAMP imaging, they can be used in other configurations to perform high-speed continuous straight-line scans. A linearly-chirped acoustic wave propagating across an AOD deflects a laser beam continuously along a lateral straight-line. However, the chirp gradient

introduces a proportional amount of astigmatism, which needs to be corrected using a fixed cylindrical lens. This effect has been exploited in an imaging method called LOTOS [69] reporting line-scan speeds of 100 kHz, 50 ns pixel dwell time and frame repetition rates of 80–1000 Hz, faster than reported using galvo or polygonal mirror scanning methods. By scanning the laser across the sample quickly and often, photo-bleaching was reduced and signal to noise could be kept high by temporal averaging.

A particularly inventive use of an AOD was reported in the method named FIRE [70]. FIRE enabled concurrent line imaging by leveraging the optical frequency shifts induced by the AOD to create optical beat-patterns. In FIRE, entire lines are acquired in parallel instead of point-by-point. This enables FIRE to achieve full-frame-rates of 4.4 kHz, which is extremely fast. This dramatic speed up is achieved by concurrently acquiring data. FIRE used only single-photon fluorescence but [70] claims that the technique is applicable to two-photon imaging also. A multiplexing system that could be incorporated more generally in other laser scanning microscopes uses an LC-SLM to tag multiple sub-beams such that the induced fluorescent signal could be decoded into different channels [71]. However, multiplexing reduces signal strength which is a problem if imaging speed is photon-limited, as it can be for high-speed two-photon microscopes.

Similar to LOTOS, AOLs are able to perform high-speed lateral line-scans [61, 68]. The additional AODs in an AOL enable it to self-correct astigmatism produced by individual AODs so no cylindrical lens is needed. A further advantage is that AOLs can theoretically perform lateral line at arbitrary axial positions, whereas LOTOS was confined to a fixed focal plane. However, the field of view of AOL line-scans performed away from the front focal plane of the microscope objective (the plane which the objective is designed to image) was found to be small for dwell times above 1 μs per pixel [61]. Full-frame line-scans were therefore practically limited to a fixed plane, similar to LOTOS. In summary, an AOL offers both the 3D-RAMP capability of the two-AOD-single-laser-pulse method and the fast lateral line-scanning of LOTOS.

More recently, it has been shown that the field of view for an AOL performing full-frame line-scanning could be kept constant over an axial range of $\pm$125 μm from the front focal plane of the objective by using brief pixel dwell times (very high speed scans) [2]. Line-scans close to full-frame length were still possible and usable over a much larger axial range. The improvement from reducing pixel dwell time follows because focusing and lateral scanning both require linearly-chirped drive frequencies. By using very high speed scans, the chirps needed for the scanning become much larger than the chirps needed for focusing. Thus, the field of view is broadly unaffected by changing the focus since its contribution to the chirps is negligible. AOL full-

frame line-scan speeds reach up to 20 kHz (512 pixels per line) and full frame imaging is 40 Hz [2, 3]. These figures are lower than that given for LOTOS which is due to differences in the number of pixels per line and are comparable with the fastest resonant galvos but with much greater flexibility. Thus, AOLs overcome a key limitation of both LOTOS and FIRE that the focal length is fixed so only a 2D slice of a sample can be imaged at high-speed; no separate mechanism is needed in an AOL microscope to image in 3D at high-speed.

Recently patented and published work on the use of nonlinearly-chirped acoustic waves in AOLs has shown that an AOL can also perform high-speed axial line-scanning [3, 72], in addition to lateral line-scans using linearly-chirped acoustic waves. Proof-of-principle axial line-scanning was experimentally demonstrated using a cylindrical AOL (cylindrical focusing rather than spherical) and further modelling indicated that axial line-scanning will be possible with a spherical AOL [3]. However, prior to this thesis, image acquisition using axial scanning had not been demonstrated using a AOL microscope. An alternative method of axial scanning was recently demonstrated using an optical phase-locked ultrasound lens [73]. The ultrasound lens confers extremely fast axial scanning at 455 kHz (~1 MHz if both up and down scans are counted separately) and size-dependent volume acquisition rates of 5-50 Hz. However, the axial range was comparatively small (~40 μm), extendable to ~130 μm if resolution was degraded. This contrasts with AOL microscopes which are able to image over axial ranges exceeding 500 μm, or even 1 mm if resolution is not critical.

A major feature recently developed for AOLs is real-time movement correction [74]. This enables microscope users to perform 3D-RAMP experiments even with a moving sample (assuming the total displacement of the sample is much less than the AOL field of view). This has been achieved by interleaving high-speed line-scans with the 3D-RAMP point measurements to track the movement of a small feature, and is an excellent example of a benefit from having both 3D-RAMP and line-scanning capabilities. Whilst AOLs are a promising versatile technology, they are not without their limitations. These are primarily a small field of view relative to galvos, remote focusing associated spherical aberration and relatively low duty cycle when performing 3D-RAMP.

1.3 THESIS STRUCTURE

In this thesis, I introduce new AOL microscope functionality and address several limitations. Chapter 2 continues the introduction by reviewing AOL-based microscopes and gives a more detailed discussion of AOL operating principles and limitations. In Chapter 3 I derive an analytic equation to describe AOL frequency drives. I iden-

tify a degree of freedom when choosing drive frequencies and show that AOL field of view depends sensitively on how this is done. In Chapter 4 I develop the first numerical model for calculating AOL transmission efficiency and use it to explore how AOL transmission efficiency varies across the imaging volume. Using both computer simulations and experimental measurements, I find that when optimal drive frequencies are used the lateral dimension of an AOL microscope's imaging volume is within a factor of two of a commercially available galvo-based microscope's field of view [75, 76].

In Chapter 5 I examine whether modulation of acoustic drive power can significantly enhance the size and uniformity of the imaging volume. For the first time, I extend such acoustic amplitude modulation to line-scanning and find that AOD transducer width should be matched to available acoustic power. For the existing compact AOL microscopes, I show transmission efficiency can be made near-uniform across a 350 μm field of view (20$\times$ objective) by modulating the acoustic drive power. However, I found using amplitude modulation on biological samples made the signal too weak, and more that 2 W of laser power would be needed to see the benefits.

Nonlinearly-chirped frequency drives have opened the possibility of new AOL microscope imaging modes. In Chapter 6 I overcome the key limitation of existing nonlinear drive theory: how to handle spacing between AODs in a compact AOL. I begin by establishing new geometric optical aberration propagation theory, which can be directly applied to AOLs. I derive the nonlinear drive relations in order for a compact AOL microscope to perform arbitrary-direction line and curved scanning. I demonstrate three nonlinear imaging modes (arbitrary-plane, curved-surface, glove) with a compact AOL for the first time. In Chapter 6 I experimentally verify the new nonlinear drive theory showing images acquired using nonlinear drives produce comparable image quality to linear drives. Furthermore, I demonstrate that an AOL can image a series of cubic volumes fitted tightly around dendrites (glove mode) at speeds of up to 10 kHz, which will enable new ways of probing dendritic activity.

In Chapter 8 I examine aberration correction using nonlinear frequency chirps: using a 2D fast Fourier transform (FFT) wave model which accounts for spatial chromatic aberrations, I simulate spherical aberration partial correction by a compact AOL and full correction by a new AOL design based on six AODs. I derive the linear chirp relations for six AODs to behave as a spherical lens, using a matrix formalism suitable for computer algebra systems. In Chapter 9 I propose AOL variations which have particular strengths and may be worth exploring further. Finally, Chapter 10 draws conclusions and discusses the future of AOLs in neuronal imaging.

2 ACOUSTO-OPTIC LENS MICROSCOPES

Having established the rationale for developing AOL-based microscopes in the preceding Chapter, in this Chapter I review AOL design including the particulars of AODs themselves. This Chapter sets out the state of AOL microscope development at the time I began my PhD.

2.1 MICROSCOPE OPERATION

AOL microscopes were first shown to be capable of performing near-instantaneous jumps between discrete points in 3D space at 40 kHz, making them suitable for 3D-RAMP microscopy [59]. However, the *duty cycle* (time spent acquiring data as a fraction of total operating time) of an AOL for imaging a series of spatially-discrete points is only 5–15% depending on the dwell time at each point. This is a general feature of all current AOL designs. Further work demonstrated AOLs could perform full-frame continuous line-scanning in the front focal plane of the microscope objective at 20 kHz [61, 68]. This mode of imaging can achieve a far greater duty cycle (up to 80%) and therefore enabled AOL microscopes to acquire structural images much faster.

In addition to full-frame line-scans in a single plane, it was shown that shorter continuous lateral line-scans could be performed out of the front focal plane [61, 62]. The main use of shorter line-scans out of the front focal plane is to efficiently image small regions of interests. Longer lines could be constructed from a series of shorter lines, but the duty cycle was reduced by doing this, and image brightness was far greater at the centre than at the edges of the individual lines producing an artificial oscillatory pattern. At the time I began my PhD (August 2013), the Silver Lab at UCL had upgraded their AOL microscope acquisition system to enable faster sampling (200 MHz, dual channel). This enabled the AOL microscope to perform faster continuous line-scanning for the first time and they found that full-frame lateral line-scans were possible if a dwell time of 0.1 μs per pixel or less was used [2].

These capabilities make AOL microscopes well-suited for imaging rapid neuronal signalling distributed in 3D space using activity-dependent fluorescent indicators. A typical use of the microscope would be to image a cuboid-shaped volume of a sample to determine its structure. Once the volume had been acquired, regions of interest would be selected for high-speed functional imaging. AOL-based mi-

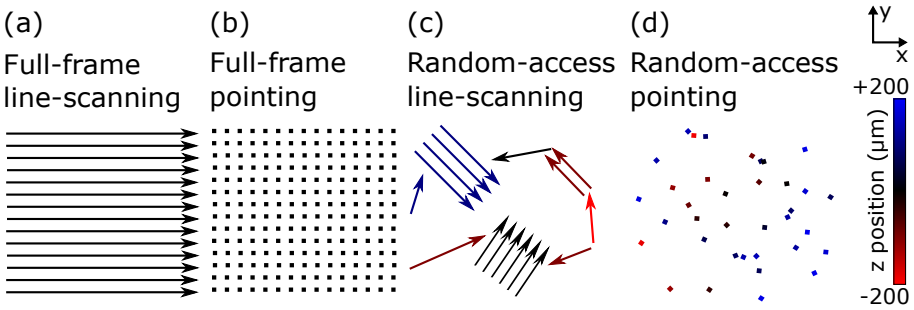

Figure 2.1: AOL imaging modes. Lines and points coloured to indicate axial (z) depth. Black indicates the front focal plane of the microscope, red below and blue above. Axial depth scale can vary and numbers are given for illustration only. (a) Full-frame line-scanning: an entire xy-plane is imaged in a raster-like fashion using a sequence of continuous horizontal line-scans. (b) Full-frame pointing: an entire xy-plane is imaged by sequentially acquiring a grid of spatially discrete points. Each point corresponds to a pixel in the image. Points are imaged sequentially from the top-left, row by row as in (a). (c) Random-access line-scanning: the microscope-user defines a pattern consisting of continuous straight-lines to be imaged. Individually, line-scans are in the xy-plane but different lines can be at different z depths, indicated by lines having different colours. (d) Random-access pointing: A microscope-user defines a pattern of discrete points distributed in 3D space to be imaged. Each point can be at an arbitrary z depth.

croscopes have four distinct operating modes as depicted in Fig. 2.1. The two first operating modes *full-frame line-scanning* and *full-frame pointing* are for imaging the static structure of the sample. The second two *random-access line-scanning* and *random-access pointing* are for high-speed functional imaging. The reason that structural and functional modes come in pairs is the first mode of each pair uses continuous straight-line scans (line-scanning) whilst the second sequentially images discrete spatial points by shifting the focal point discontinuously (pointing mode) [61]. All four of these modes can be described as *linear* imaging modes because they use linearly chirped acoustic waves (or even constant frequency) across the AODs. Recently published work has experimentally demonstrated proof-of-principle that nonlinearly chirped acoustic waves could enable *nonlinear* imaging modes [3], which I explore in Chapter 7.

Full-frame line-scanning mode is always used over full-frame pointing mode because it is significantly faster (typically by a factor in excess of 100). Full-frame pointing was primarily used before full-frame line-scanning mode had been implemented (for example [63]) but remains useful for microscope calibration and testing. Full-frame images are conventionally lateral (xy) planes because the axial (z) resolution is comparatively poor [61]. However, arbitrarily-oriented planes can be imaged in full-frame line-scanning mode, providing the scan remains in a lateral direction. In order to image a large 3D volume, frames are sequentially imaged at increasing or decreasing axial depths to create a *z-stack*. The axial position can be adjusted either by the AOL (high-speed, ~400 μm range) or by moving the motorised objective (low-speed, ~5 mm range) [63]. Thus the microscope has the capacity to image over large axial ranges with some trade-off between speed and range.

The selective imaging modes line-scanning and multi-point enable the microscope to image spatially distributed regions of interest at high-speed. They produce qualitatively different results and so the microscope user must choose appropriately. If multi-point mode is chosen, the user identifies a number of points of interest (typically 1-1000) and the microscope images the set of points one-by-one at high speed (25-30 μs per point). If line-scanning mode is chosen, the user marks out a series of lines for the microscope to image. These lines typically constitute small volumes or planes fitted around regions of interest. For example, to study the temporal correlation of neuronal excitations at different positions on individual or multiple neurons, points can be fitted along dendrites (in particular spine heads are just-resolved), axons and around somata [63]. If movement is an issue or spatial averaging is needed to improve signal quality, small patches can be imaged that contain the neurons of interest using line-scans [2].

Having described what AOL-based microscopes can do, I next discuss how they work. A detailed discussion of the design and operating principles of the compact AOL and the corresponding 3D two-photon microscope is given in [61], which I briefly summarise here. Referring to the schematic of the AOL microscope in Fig. 2.2, the key features are as follows: a femtosecond laser beam passes through a double pass prism-based prechirper before reaching the compact AOL. The prechirper preemptively compensates for the temporal dispersion introduced by the four paratellurite (TeO_2) AODs that make up the spherical AOL and the other optical components in the microscope. The AOL deflects and adds curvature to the optical wavefront, which is subsequently relayed to the back focal plane of the microscope objective by two *4f systems* (pairs of lenses with spacing either side equal to their respective focal lengths). The position of the focal point depends on the deflection and curvature added by the AOL; when no curvature is added by the AOL, the focus lies in the front focal plane of the microscope objective. The light emitted by the fluorophores (green lines in Fig. 2.2) following two-photon excitation is collected by the microscope objective, separated from the near infrared excitation light (red lines in Fig. 2.2) by a dichroic mirror and detected by a photo-multiplier tube (PMT).

Each AOD in an AOL must be driven with precise frequencies. To achieve the necessary precision with the compact AOL, custom software [63] and hardware [2, 3] have been developed. A software suite written in LabVIEW runs on a PC which communicates with the hardware. A field-programmable gate array (FPGA) generates the precise drive frequencies required and a second FPGA processes the detected fluorescence. The drive frequencies are calculated by a MATLAB script embedded in the LabVIEW program.

The use of AODs in two-photon microscopy requires consideration of chromatic dispersion because both TeO_2 and the diffractive process itself are dispersive. The dispersion can be divided into temporal and spatial dispersion [77]. As mentioned in the previous paragraph, a prechirper based on a pair of prisms are used to compensate the temporal dispersion in the AOL microscope. Systems using a pair of orthogonal AODs or a single AOD require a further AOD or grating to correct the spatial dispersion. However, the arrangement of AODs in an AOL with counter-propagating acoustic waves means that AOD-induced spatial dispersion is intrinsically compensated at the centre of the microscope's imaging volume [61]. Whilst additional correction can improve the image quality at the edges of the microscope's field of view [62], the resolution is already sufficient for most biological experiments.

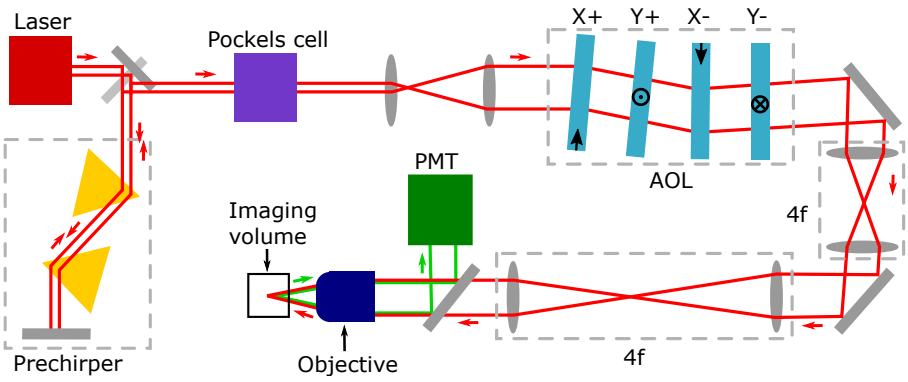

Figure 2.2: Schematic diagram of a 3D two-photon AOL microscope. Mirrors and lenses shown in grey. All other components coloured and labelled. The crossed mirrors to the right of the laser are at different elevations. The laser is a femtosecond pulsed laser suitable for two-photon excitation. The prechirper comprises two prisms and a mirror used to add temporal dispersion to the laser beam. The intensity of the laser beam is controlled by the Pockels cell. The AOL is shown as four AODs (X+, Y+, X-, Y-) with their acoustic directions indicated in black. The beam is relayed by two 4f systems from the AOL to the back focal plane of the microscope objective. The position of the focal point inside the imaging volume is precisely and rapidly controlled by the AOL. Green lines indicate two-photon fluorescence that is detected by the PMT. The mirror to the right of the objective is dichroic. Polarisers and wave plates are not shown but are as follows. Light from the laser is linearly polarised and remains so until just before the AOL. Immediately before each AOD, the polarisation is converted from linear to near-circular by a half-wave plate and quarter-wave plate. Immediately after each AOD, the polarisation is converted back to linear by a quarter-wave plate and unwanted diffraction modes are removed by a linear polariser. The polarisation leaving the AOL and is therefore linear and remains so as it propagates to the imaging volume. (Published in [1])

2.2 ACOUSTO-OPTIC LENSES

AOLs are dynamic diffractive devices that can focus and steer an optical beam with high speed and precision. AOLs have applications in high-speed 3D two-photon functional microscopy and are increasingly popular in neuroscience [60, 62, 63, 78–80]. There are other potential applications of AOLs such as in optical data storage [81] but to date these have not been explored.

AOLs were initially conceived as cylindrical lenses that used two AODs oriented to have their acoustic waves travelling in opposite directions (counter-propagating) [58]. Such pairs of AODs are called cylindrical AOLs. Furthermore, it was proposed that a spherical AOL could be constructed from two orthogonal cylindrical AOLs, as is possible with conventional long-focal-length lenses. The compact AOL design used for experiments in this thesis can focus light at $|z_{\mathrm{AOL}}| > 1$ m, where z_{AOL} is the axial displacement of the focus from the last AOD of the AOL, and achieve lateral deflections of ± 12 mrad ($\sim 1.5^{\mathrm{o}}$). In the context of a compact AOL microscope, this 3D region is typically mapped to an imaging volume of $250 \times 250 \times 400$ μm.

2.2.1 *Operating principle*

The focal position of an AOL is controlled by driving each AOD's transducer with either constant or linearly chirped frequencies. Each transducer generates an acoustic wave that propagates across the AOD's aperture. A ray of light passing through an AOD is deflected by an angle θ parallel or anti-parallel to its acoustic wave, where the angle is determined by the local acoustic frequency F, the optical wavelength in vacuum λ and the acoustic velocity V [59]:

$$\theta = \pm \frac{\lambda F}{V} \tag{2.1}$$

The positive or negative sign of Eq. (2.1) depends on whether the AOD is configured to operate in the $+1$ or -1 diffraction mode; this is determined by the orientation of the incident optical beam and the AOD as shown in Fig. 2.3. Some light is diffracted by multiples of θ, which are known as higher-order modes. Generally, the N^{th} diffraction mode is diffracted by an angle $N\lambda F/V$ where N is an integer. In an AOL, light diffracted into modes other than the operating mode (either $+1$ or -1) needs to be filtered out by using polarisers or blocked in the Fourier plane of a 4f system. Typically, 60-90% of light is diffracted into the operating mode, with the exact efficiency depending on acoustic frequency, drive power and transducer width. About 10-35% remains in the undiffracted 0 mode and a small amount ends up in the ± 2 modes. The physical origins of the diffraction modes are described in Section 2.5.2.

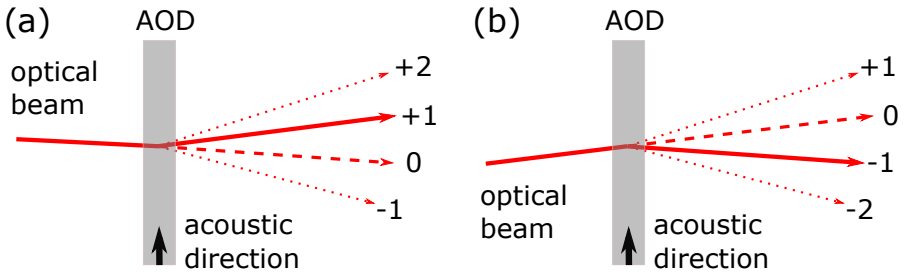

Figure 2.3: Diffraction of an optical beam into multiple modes by an AOD. (a) The incidence angle is adjusted to maximise diffraction into the $+1$ mode. Some light continues undiffracted in the 0 mode and small amounts of light are diffracted into the $+2$ and -1 modes. (b) As for (a) but the incidence angle is adjusted to maximise diffraction into the -1 mode. This is the configuration used for AODs in the AOLs described in this thesis.

When driven with constant frequencies, each AOD in an AOL deflects the optical beam by an angle proportional to the acoustic drive frequency as shown in Fig. 2.4(a). When linearly chirped drives are applied they produce a gradient of acoustic frequencies across the AOD. This adds curvature to the optical wavefront because the light rays are diffracted by different angles across the AOD aperture as shown in Fig. 2.4(b). Thus the strength of focusing increases with the steepness of the frequency chirp.

A challenge associated with acoustic waves propagating across the AODs is that the AOL focal position tends to move with them. It was shown for particular chirp gradients that the motion of the acoustic waves cancel out and a stationary focus is achieved [58, 59]. Alternatively, a focus with constant velocity can be produced which is faster or slower than the acoustic wave propagation speed and moves in any lateral direction by calculating chirp gradients using the *drive equations* [61]. Another problem due to acoustic wave propagation across an AOD is the drive frequency at the transducer must be continuously decreasing (or increasing) in order to maintain a constant frequency gradient. However, AODs operate within a finite frequency range, which imposes a ceiling on the duration of a linear chirp. To overcome this limitation and allow points to be imaged for an indefinitely long sequence of short intervals, AODs are driven with a series of frequency ramps (sawtooth) instead of a single, long, linear chirp.

2.2.2 *Design and configuration*

All spherical AOL designs have been based on two orthogonal cylindrical AOLs [60–62]. However, the designs differ in their use of optics between AODs as shown in Fig. 2.5. The AOL design used in [59, 60, 79, 80, 82] is shown in Fig. 2.5(a) where three 4f systems are used. The AOD spacing is effectively zero for an optical beam propagat-

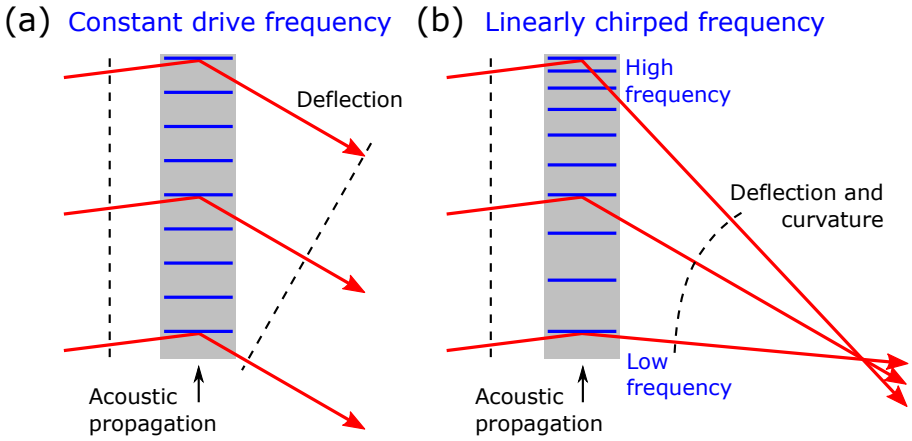

Figure 2.4: An AOD driven with constant and linearly-chirped frequencies diffracts an optical beam into the -1 mode. Rays are shown in red, optical wavefronts as dashed lines and acoustic wavefronts in blue. (a) The AOD transducer is driven with a constant frequency to produce an acoustic wave with constant frequency and wavelength. The optical beam is uniformly deflected with no change in curvature (parallel rays remain parallel). (b) The AOD transducer is driven with a linear chirp such that the acoustic wave's frequency and wavelength varies across the aperture. The central ray experiences the same local frequency as in (a) and is deflected by the same angle. However, the top ray experiences a higher frequency so it is deflected more and the bottom ray experiences a lower frequency so it is deflected less. The net effect is to introduce curvature (focus) as well as deflection. The curvature is proportional to the frequency gradient. (Published in [1])

ing through such an AOL, which simplifies the relationship between AOD drive frequencies and focal position. Furthermore, unwanted AOD diffraction modes are easily blocked in the Fourier plane of each 4f system. The main limitation is that the optical path for this design is very long and therefore needs careful optical alignment. In Fig. 2.5(b), a single 4f system is used in the middle of the AOL. AOD spacing can be made effectively zero for the two cylindrical AOLs. However, there is an offset between the cylindrical AOLs which needs to be accounted for when calculating the drive frequencies to avoid astigmatism. This is more compact than the triple system and still allows for easy filtering of unwanted AOD diffraction modes. This design was chosen in [62, 78]. In Fig. 2.5(c) the AOL uses no 4f systems to take a minimum of space. Thus it is called a compact AOL, and is the design of choice for the Silver Lab at UCL [1, 61, 63]. AOD spacing must be accounted for when calculating drive frequencies and unwanted AOD diffraction modes must be filtered using additional polarisers. The benefit is that the compact AOL is highly portable and makes AOL microscope construction more modular.

The AOLs I have used in the experiments described in this thesis were all compact designs. Nevertheless, the theory and methods reported are equally applicable to the AOLs which are not compact. The compact design was initially chosen to minimise the optical path length: a compact AOL fits into a $25 \times 25 \times 20$ cm box [61]. The major benefit of the compact design is that the AOL can be assembled and precisely aligned at a workstation away from the microscope itself. However, the majority of the assembly time in my experience has been aligning the polarisers and wave plates required to block unwanted undiffracted light (see caption of Fig. 2.2). The use of 4f systems in optical processing is common and using one in an AOL provides a simple means to remove the unwanted light without polarisers. For future AOLs, the single-relay AOL may lend itself to more efficient microscope assembly and perfect blocking of unwanted diffraction modes. It is not clear though if further practical challenges would arise from having a much longer optical path such as sensitivity to small beam perturbations that can be expected in a lab.

For the compact AOL used for experiments in this thesis, the acoustic directions of the four AODs (in the order that the optical beam passes through them) are taken to be $+x, +y, -x, -y$, where x, y, z are the axes of our lab reference frame (z is aligned with the optic axis and is therefore the axial direction; x and y are the lateral directions). The AODs are thus referred to in this thesis as X+, Y+, X-, Y- respectively, as shown in Fig. 2.2 (the AOD pairs X+, X- and Y+, Y- form orthogonal cylindrical AOLs). The AODs were made from TeO_2, chosen for its slow shear acoustic mode which has a very high acousto-optic figure of merit [83]. To make use of the slow acoustic mode, all of the AODs had the transducer normal to $\langle 110 \rangle$ in the basis of

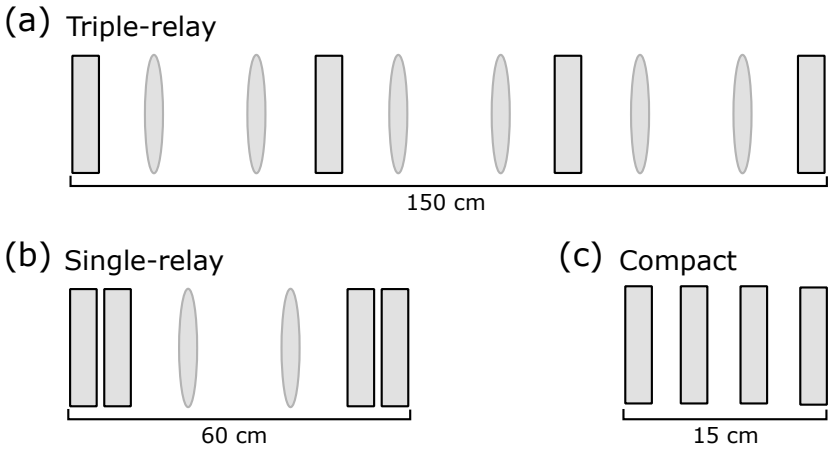

Figure 2.5: Possible use of unit magnification 4f relays between AODs in a spherical AOL. Not to scale: typical optical path lengths shown under AOLs for comparison.

the AOD's crystal lattice vectors and the aperture was normal to the crystal's optic axis ($\langle 001 \rangle$ in the crystal lattice vector basis). The AOD apertures had dimensions of $15 \times 15 \times 8$ mm. The first two AODs (X+ and Y+) are wide transducer designs (~3 mm) and the second two (X- and Y-) are narrow (~1 mm), the importance of which is discussed in Section 2.5.1. All AODs used were manufactured by Gooch and Housego. Each AOD in the AOL was aligned at its Bragg angle (the angle for peak diffraction efficiency) corresponding to 39 MHz drive frequencies and 920 nm optical wavelength. There were narrow gaps between the AODs (5 cm from centre-to-centre) containing polarising units used to convert the optical polarisation to near-circular as required for optimal coupling into the desired AOD modes [1].

2.3 LINEAR DRIVE THEORY

For over a decade, it has been known that two AODs aligned to have counter-propagating acoustic waves can focus light at precisely known focal lengths [58]. However, the derivation of the drive equations for a compact AOL was more recent and more complicated than for the other AOL designs in Fig. 2.5 because the space between AODs needs to be allowed for [61]. I begin by examining single-AODs, and proceed by extending first to compact cylindrical AOLs then compact spherical AOLs. Because the drive equations for compact AOLs allow variable AOD spacing, the simpler drive equations for the other two AOL designs can be found as a special cases by setting the AOD spacing parameter to zero.

2.3.1 *For a single acousto-optic deflector*

AODs have been used to manipulate light since before the 1960s [84]. The behaviour of an optical plane wave incident on an AOD is well-understood [85]: an acoustic wave propagating across the AOD aperture diffracts the optical wave by an angle θ proportional to the acoustic frequency F, as given by Eq. (2.1). To handle more general optical waves and time-varying acoustic frequencies, rays can be used [61]. Rays passing through an AOD are deflected by the same angle as a plane wave, where the local acoustic frequency at the ray's point of intersection with the AOD determines the deflection angle. If the AOD's transducer is driven with frequency $\mathscr{F}(t)$, the local acoustic frequency at a distance x from the transducer in the acoustic wave's direction of travel is $\mathscr{F}(t - x/V)$ where V is the acoustic speed. Thus the acoustic frequency across the entire AOD aperture can be inferred precisely from the time-dependent transducer frequency.

If an acoustic wave of constant frequency is driven across the AOD, the rays of an incident optical beam will be uniformly deflected by an angle given by Eq. (2.1). In order to shift the laser focus the AOD must be re-filled with a new constant frequency acoustic wave: the focus will jump discontinuously from point to point with a 10–30 μs transition period required for the acoustic wave to propagate across the aperture, inefficient when wanting images with high spatial resolution. Thus, by discontinuously switching the acoustic frequency, the focal position performs a discontinuous lateral jump. An alternative is to use linearly-chirped acoustic waves to continuously scan the focal spot laterally. When acoustic frequencies are linearly-chirped (change linearly with time), the local frequency and therefore the deflection angle varies across the aperture of each AOD. The frequency of an AOD's transducer driven with a linear chirp is described by

$$\mathscr{F}(t) = a + bt \tag{2.2}$$

where a is the frequency at $t = 0$ (the *centre frequency*) and b is the gradient of the linear chirp. The frequency of the acoustic wave F at a distance x from the transducer will therefore be

$$F(t, x) = \mathscr{F}\left(t - \frac{x}{V}\right) = a + bt - \frac{bx}{V} \tag{2.3}$$

A complication when driving an AOD with a linear chirp is that 2D curvature is added to an incident optical beam because the deflection angle varies across the aperture. The curvature is proportional to the chirp gradient b and can be corrected using a cylindrical lens or another AOD.

The AODs are only efficient in a limited range of acoustic frequencies due to the need for the wavevector matching described in Section 2.5.2. These frequencies are given by $|F - F_0| < \Delta F/2$, where F_0 is the *optimal frequency* and ΔF is the *bandwidth* of the AOD typically

defined by the full-width at half-maximum (FWHM) of the diffraction efficiency. For this reason, the AOD is driven by a series of ramps as illustrated in Fig. 2.6(a). An important drawback of using ramps is that the AOL is only focusing properly for a fraction of the time it operates, limiting the duty cycle. To understand why an AOL's duty cycle is necessarily less than 100%, consider a ramp propagating across an AOD: until the start of the ramp has propagated to the far side of the aperture, the AOD will not correctly deflect the optical beam. Thus, each time a new ramp is loaded into the AOD, it must remain idle for the *fill time* $\tau = W/V$, where W is the aperture width. For the AOD design considered in this thesis the fill time is 24.5 μs. For line-scans, frequency ramps can be long and the duty cycle can be high, up to 80%. For pointing mode, or even short line-scans, frequency ramps need changing often and the fill time means the duty cycle can be as low as 5%. One might want to reduce the fill time in order to improve the duty cycle. Unfortunately, there is a trade-off here: the number of resolvable points is given by the time-bandwidth product, $N = \tau\,\Delta F$ [68], and so increasing duty cycling comes at the price of reducing the number of resolvable points.

Having set out the rules for rays passing through an AOD with known drive frequency, I now show how a single AOD can create a 2D focus. Substituting Eq. (2.3) into Eq. (2.1) gives

$$\theta = \pm\frac{\lambda}{V}\left(a + bt - \frac{bx}{V}\right) \tag{2.4}$$

where the sign depends of whether the AOD is operating in the $+1$ or -1 diffraction mode. Experimentally, the AODs I have used were aligned to operate in the -1 mode. It is simple to convert theory derived for the $+1$ mode to theory for the -1 mode by changing the sign of F. An interesting implication of this is that when the AOD theory calculates negative frequencies, the result can be realised physically by operating the AOD in the opposite diffraction mode, although I have not found any practical benefit of this interpretation.

The interpretation of Eq. (2.4) is as follows: the last term produces a (cylindrical) focus, the first two terms $a + bt$ offset the lateral position of the focus. To determine the focal length consider two rays separated by a distance δx. According to Eq. (2.4), the angles of the rays will differ by $\mp\lambda b\delta x/V^2$ (positive b causes convergence in $+1$ mode and divergence in -1 mode) and assuming small angles these two rays meet at a distance of

$$f = \pm V^2/\lambda b \tag{2.5}$$

Because f is independent of δx, every ray will meet at distance f; the AOD is behaving as a cylindrical lens of focal length f. In Fig. 2.6(a), three different drive frequency ramps are shown. The blue drive ramp has a greater slope (greater b) than the red and so the focal length is shorter as illustrated by Figs. 2.6(b) and (c).

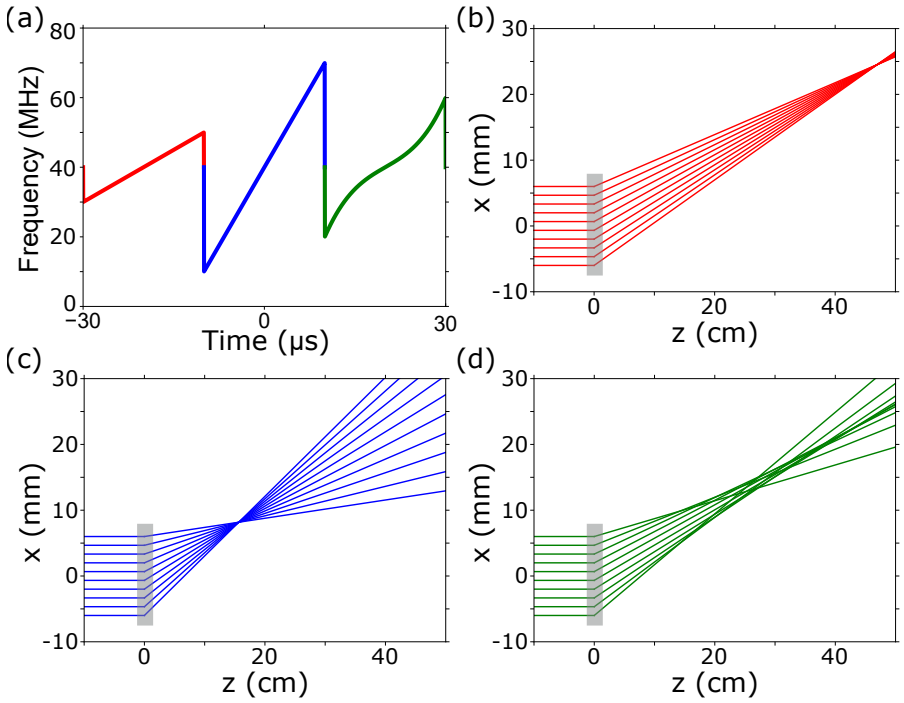

Figure 2.6: (a) Time-dependence of three consecutive frequency ramps for an AOD. The frequency is periodically reset in order to maintain high diffraction efficiency producing a sequence of frequency ramps (red, blue, green). Each ramp is chosen to diffract the incident optical beam in a particular pattern. The three different frequency ramps were calculated using a, b, c, d as given in Eq. (2.10). Red has $a = 40$ MHz, $b = 1$ MHz μs^{-1} and $c = d = 0$; blue has $a = 40$ MHz, $b = 3$ MHz μs^{-1} and $c = d = 0$; green has $a = 40$ MHz, $b = 1$ MHz μs^{-1}, $c = 0$ and $d = 0.01$ MHz μs^{-3}. The effect of each ramp on an incident plane wave at $t = 0$ is shown in (b), (c) and (d) for an AOD operating in the $+1$ mode. (b) the red ramp focuses the rays at just under 50 cm. (c) the blue ramp focuses the rays at around 16 cm. (d) The green rays do not form a stigmatic focus, having a 2D analog of spherical aberration, due to d being non-zero.

Now the focal length has been determined, the first two terms $a + bt$ can be interpreted more precisely. By Eq. (2.4), the first two terms cause an angular deflection of $\lambda (a + bt) / V$ and therefore a lateral displacement of the focus of $f\lambda (a + bt) / V = Va/b + Vt$. The first term Va/b is a time-independent displacement of the focus whilst the second term Vt corresponds to the focus moving with the velocity of the acoustic wave. This can also be understood as follows: if the acoustic wave was stationary, the focus would be stationary; laterally translating our reference frame at velocity V would make both the acoustic wave and the focus move with velocity V together. With the behaviour of a single AOD understood, multiple AODs can be concatenated in series to gain additional control over the trajectory of the laser focus.

2.3.2 *For a cylindrical acousto-optic lens*

Section 2.3.1 showed how a single AOD driven with a linear-chirp could behave as a cylindrical lens with any focal length but produced a focus moving laterally with speed V. Here I discuss how two AODs aligned to have counter-propagating acoustic waves (a cylindrical AOL) can behave as a cylindrical lens with any focal length z_{AOL} and any lateral scan velocity v parallel to the direction of the acoustic waves. The original derivation of the linear chirps required for a cylindrical AOL followed a geometrical ray argument and used non-Cartesian coordinates [61]. I have reproduced the argument in Appendix A using Cartesian coordinates which are consistently used through this thesis. In the case that the two AODs are separated by distance s and operate in the $+1$ diffraction mode, the drive equations for a cylindrical AOL are

$$\begin{aligned} b_+ &= \frac{V^2}{\lambda}\frac{(1+v/V)}{2z_{\mathrm{AOL}}+s\,(1+v/V)} \\ b_- &= \frac{V^2}{\lambda}\frac{(1-v/V)}{2z_{\mathrm{AOL}}} \end{aligned} \tag{2.6}$$

where b_+ is the linear chirp (frequency gradient) on the first AOD with acoustic wave propagating in the positive lateral direction and b_- is the linear chirp on the second AOD with acoustic wave propagating in the negative lateral direction.

To help understand these expressions, notice that the values of $v = \pm V$ correspond to the chirp being on only one of the AODs. This is consistent with a single AOD producing focal spots scanning with velocity V and the AODs in a cylindrical AOL having opposite acoustic propagation directions. If the AODs are instead operating in the -1 mode, the sign must be changed for $b_+$and b_-.

An intuitive picture which holds for $s \ll z_{\mathrm{AOL}}$ is based on decomposing the pair of linear chirps into a symmetric and anti-symmetric pair (b_S, b_A) such that $b_\pm = b_S \pm b_A$. The cylindrical AOL's focusing power is determined by b_S and the lateral scanning velocity by b_A [3]. This is key in understanding why high-speed line-scans can be full-frame when $|z_{\mathrm{AOL}}| < \infty$: for slow scans $b_\pm$ are dominated by b_S so efficiency falls off over a short scan distance, whereas $b_\pm$ are dominated by b_A for fast scans so the line-scanning field of view is very comparable to the pointing mode field of view.

2.3.3 *For a spherical acousto-optic lens*

Drive equations for a spherical AOL determine the linearly-chirped frequencies for each of the four AODs required to focus an optical beam. The focus can move at any constant lateral velocity (v_x, v_y),

including being stationary. The AOD acoustic directions are in the order $+x, +y, -x, -y$, and z_{AOL} is the focal length: the distance from the last AOD to the focus. The linear chirps follow directly from Eq. (2.6) and are given explicitly below:

$$\begin{aligned} b_{\mathrm{X}+} &= \frac{V^2}{\lambda}\frac{(1+v_x/V)}{2(s+z_{\mathrm{AOL}})+2s(1+v_x/V)} \\ b_{\mathrm{Y}+} &= \frac{V^2}{\lambda}\frac{(1+v_y/V)}{2z_{\mathrm{AOL}}+2s(1+v_y/V)} \\ b_{\mathrm{X}-} &= \frac{V^2}{\lambda}\frac{(1-v_x/V)}{2s+2z_{\mathrm{AOL}}} \\ b_{\mathrm{Y}-} &= \frac{V^2}{\lambda}\frac{(1-v_y/V)}{2z_{\mathrm{AOL}}} \end{aligned} \tag{2.7}$$

These drive equations are equivalent to equations (18) and (19) in [61] but the focal motion is given in terms of linear velocities instead of angular velocities. By using Eq. (2.6), the AODs have been assumed to operate in the $+1$ mode. If the AODs are all operating in the -1 mode, the sign must be changed for each of the four bs. Relating these equations back to the AOL operating modes, for pointing (full-frame or random-access) $v_x = v_y = 0$, for full-frame line-scanning $v_x \neq v_y = 0$ and for random-access line-scanning it is usually true that $v_x \neq v_y \neq 0$.

In light of these drive equations, a comment should be made about the AOL design described in [62]. It is claimed that focusing and lateral line-scanning are performed respectively by the linear-chirp gradients (b) on the front and back pair of AODs. However, it is clear from the discussion found under *Continuous 3D trajectory scanning with AO deflectors* that the values of b on the back pair of AODs also contribute to the focusing. Furthermore, Eq. (2.7) shows focusing and line-scanning cannot be decoupled. Given the term 'lateral drift compensation' is used to describe the back pair of AODs, a reader could easily overlook the fact that such 'compensation' also affects the focal length. The important design improvement made in [62] was moving bulk lateral deflections onto the back pair of AODs (X-,Y-) by better assigning the time-independent frequency coefficients (a) across the four AODs.

2.4 NONLINEAR DRIVE THEORY

An infinity-corrected microscope objective focusses a plane wave to a diffraction-limited point spread function (PSF) in its front focal plane. Remote focusing microscopes, those which shift the focus out of the objective's front focal plane, progressively introduce spherical aberration as the distance increases [86]. This is a significant limitation of AOL microscopes. An aberration-free remote-focusing microscope

has been designed [87] but is incompatible with an AOL. To address this limitation, it was realised that nonlinear frequency chirps could be used [72]. Subsequently, it was demonstrated experimentally that a cylindrical AOL can correct 2D spherical-like aberrations and shown theoretically that a spherical AOL comprising six AODs (instead of the conventional four) could correct full 3D spherical aberration [3]. Continuous axial scanning was also demonstrated, which will enable a range of new nonlinear AOL microscope imaging modes [3]. While the majority of the ideas in the paper were developed before I joined the lab, I am a co-author for my contribution of quantifying the spherical aberration arising in an AOL microscope through FFT-based modelling. Specifically, see Fig. 6 in [3] (Fig. 8.1 in this thesis) and the particular algebraic expressions in [3] Table 1 (Table 6.1 in this thesis).

The key idea behind the theory put forward in [3] is that the phase of the diffracted optic wave, ϕ_d, is equal to the sum [difference] of the phases of the incident optic wave, ϕ_i, and the acoustic wave, Φ, for an AOD operating in ± 1 diffraction mode enabling us to make sense of nonlinear AOD drives:

$$\phi_d = \phi_i \pm \Phi \tag{2.8}$$

By taking the AODs to have zero optical separation between them ($s = 0$), modelling an AOL becomes as simple as adding the phases of the acoustic waves (in Chapter 6 I solve the more general case $s \neq 0$). The drive frequency is proportional to the time derivative of the acoustic phase:

$$\mathscr{F}\left(t - \frac{x}{V}\right) = \frac{1}{2\pi} \times \frac{\partial \Phi(t,x)}{\partial t} \tag{2.9}$$

On the basis of Eqs. (2.8) and (2.9), each coefficient in the drive frequency power series shown in Eq. (2.10) could be identified with a distinct use.

$$\mathscr{F}(t) = a + bt + ct^2 + dt^3 + \ldots \tag{2.10}$$

The components a and b already discussed for linear chirps following Eq. (2.2) retain the same significance. The new coefficients, c and d enable continuous axial scanning and 2D-spherical-like aberration correction respectively. Higher powers of t can be included ($e, f, \ldots$) but the hardware used for frequency synthesis presently only allows up to d. According to Eq. (2.9) frequencies correspond to particular phase patterns. In terms of wavefronts, a corresponds to tilt, b to focus, c to 2D-coma-like aberration, and d to 2D-spherical-like aberration. The green ramp in Fig. 2.6(a) has a non-zero cubic chirp coefficient d which causes the 2D-spherical-like aberration exhibited by the green rays in Fig. 2.6(d).

To show how quadratic (c) and cubic chirps (d) can be used to introduce axial scanning and 2D-spherical-like aberration in a cylindrical

AOL, consider the sum of acoustic phases across the first and second transducers Φ_+ and Φ_-. For quadratic chirps the phase is cubic and for cubic chirps the phase is quartic:

$$\begin{aligned}\Phi_+ + \Phi_- &= \frac{2\pi c}{3}\left[\left(t - \frac{x}{V}\right)^3 + \left(t + \frac{x}{V}\right)^3\right] \\ &= \frac{4\pi c}{3}\left(t^3 + \frac{3tx^2}{V^2}\right)\end{aligned} \tag{2.11}$$

$$\begin{aligned}\Phi_+ + \Phi_- &= 2\pi\frac{d}{4}\left[\left(t - \frac{x}{V}\right)^4 + \left(t + \frac{x}{V}\right)^4\right] \\ &= \pi d\left(t^4 + 6\frac{t^2x^2}{V^2} + \frac{x^4}{V^4}\right)\end{aligned} \tag{2.12}$$

For the bottom-right-hand side of Eqs. (2.11) and (2.12), the first term is independent of x and only involves t, a global phase shift that can be ignored. In Eq. (2.11) the significant phase shift is therefore the latter term corresponding to curvature growing linearly with time, or constant velocity axial scanning. In Eq. (2.12), the last term corresponds to 2D-spherical-like aberration. The middle term involving t^2x^2 also corresponds to axial scanning but with constant acceleration instead of constant velocity. On the face of it, axial acceleration is an impediment to spherical aberration correction when imaging a stationary point. A work-around is to make scan durations sufficiently brief that the term is negligible and Eq. (2.12) shows that the duration will vary with the inverse-square-root of d. More strategically, the ability to have nonlinear axial scanning may be useful [3]: curved lines and surfaces could be fitted to regions of interest.

To correct full 3D spherical aberration, an AOL would need to generate $\left(x^2 + y^2\right)^2$ phase terms. The conventional spherical AOL comprising four AODs cannot generate such phase terms because of the cross terms x^2y^2 in $\left(x^2 + y^2\right)^2 = x^4 + 2x^2y^2 + y^4$ [3]. Partial correction is possible by compensating x^4 and y^4 [65]. It has been shown that six AODs could theoretically correct for spherical aberration. However, drive equations for a 6-AOD AOL are required, and I derive them in Section 8.2.

The phase modulation ability of AODs opens up the possibility of more general aberration correction to improve image signal and resolution [88]. Aberrations arise in biological tissue primarily because of scattering across different spatial scales, resulting in a degraded point-spread function [89]. Adaptive optics in two-photon microscopy often involves the addition of an LC-SLM or a DMD to the system [90]. It is therefore highly appealing that an AOL may be able to intrinsically correct aberrations. Using an LC-SLM it has been shown that near-diffraction-limited resolution can be achieved at depths down to 400 μm in biological samples [91] and fast-updating correction can be

enabled by combining guide star and direct wavefront sensing [92]. However, it is unlikely that an AOL would be able to perform such impressive aberration correction since even a 6-AOD AOL would be limited to the first eight Zernike modes [3], far fewer than used in LC-SLM or DMD-based aberration correction systems.

2.5 ACOUSTO-OPTIC DEFLECTORS

2.5.1 *Design*

The transmission efficiency and field of view of an AOL depends sensitively on the design of the constituent AODs. An AOD is essentially a crystal aperture with a transducer bonded to one side; the primary design choices are the crystal material and transducer. There are finer details to ensure high performance, such as the anti-reflection coatings on both sides of the very-flat optical aperture, a heat-sink on the opposite side to the transducer and an impedance matching network connecting the electronic radio frequency (RF) drive signal to the transducer. A front-view of an AOD from a compact AOL I have used is shown in Fig. 2.7(a). The crystal used for the AOD aperture is TeO_2 (specifically $\alpha-TeO_2$). It is a tetragonal crystal with outstanding acousto-optic properties [93] and has been studied extensively. TeO_2 is acoustically anisotropic to a great degree: there is a slow shear mode along the crystal direction $\langle 110 \rangle$ with a phase velocity of only 613 m/s (favourable for acousto-optic diffraction) and other acoustic modes with velocities exceeding 2000 m/s [85]. Optically, it is uniaxial and optically active with high refractive indices greater than 2 over optical and infrared wavelengths [94].

The transducers on TeO_2 AODs have two key variables, which are their geometry and their orientation relative to $\langle 110 \rangle$. The compact AOLs use AODs with different transducer widths for the front and back pair: the front have wide transducers of width of 3.3 mm and the back have narrow transducer widths of 1.2 mm, which are shown for comparison in Fig. 2.7(b). The AOD apertures are normal to the crystal $\langle 001 \rangle$ direction and the transducers normal to the $\langle 110 \rangle$ direction, reducing their frequency bandwidth but allowing them to be thinner than acoustically or optically rotated designs (for example those used in [62]). The reason two different transducer widths are used is that wide transducers have a high diffraction efficiency over a small range of incidence angles whereas a narrow transducer has a lower peak diffraction efficiency but is good over larger range of incidence angles [61]. The wide transducers are therefore used for the first two AODs in a spherical AOL because the incidence angles are fixed. The narrow transducers are used for the second two AODs in an AOL because the incidence angles depend on where the AOL is focusing.

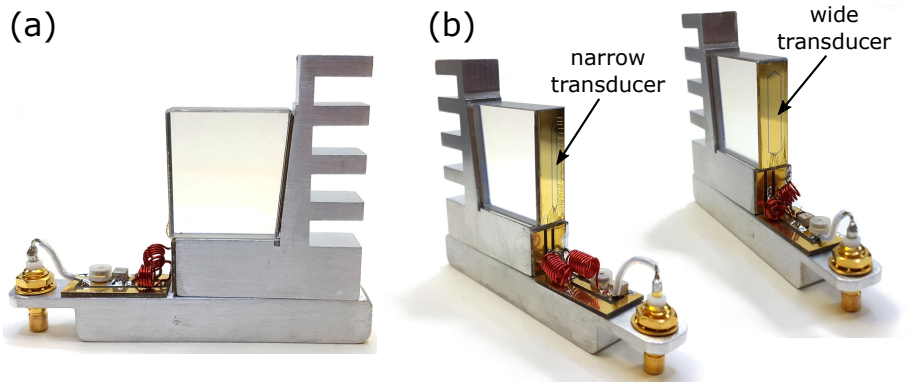

Figure 2.7: (a) A front-view of one of the AODs currently used in a compact AOL, see Fig. 2.5(c). The optical aperture is a TeO_2 crystal, 15 mm wide. The transducer is located on the left-hand side of the aperture (not visible). The metallic feature on the right-hand side is a heat sink to dissipate the energy of the acoustic wave once it has propagated across the crystal to avoid back-scattering. The impedance matching circuit between the transducer and the electronic RF input signal is visible on the bottom right-hand side. (b) Two similar AODs with different transducer widths. The AOD on the left has a narrower transducer than the AOD on the right. The transducers are outlined by vertical narrow hexagons.

There are alternative AOD designs that could be considered [95] and promising new material developments [96]. However, as of 2016, AODs cost several thousand pounds (GBP) each and take months to be manufactured. It is therefore infeasible to iterate through a large range of different designs to determine the best. The numerical ray-based model I develop in Chapter 4 will be able to aid future decisions on which designs of AOD will be well-suited for use in an AOL.

2.5.2 *Theory*

The theory of AODs was largely developed in the 60s and 70s [84, 97] as they found uses following the invention of the laser [98]. AODs made from optically or acoustically anisotropic crystals are harder to model than those made from isotropic crystals. Even so, there is an analytic solution for the efficiency of Bragg (single-order) diffraction in anisotropic crystals, which has been applied to TeO_2 AODs [85]. The analytic solution assumes a *sound column* which makes the model tractable but not physically realisable. The analytic result can therefore be regarded as an approximation or interpreted as showing the interaction is between particular angular spectrum components of the acoustic and optical waves.

To outline the key elements of acousto-optic diffraction theory, I consider the simple example of the interaction between an optical

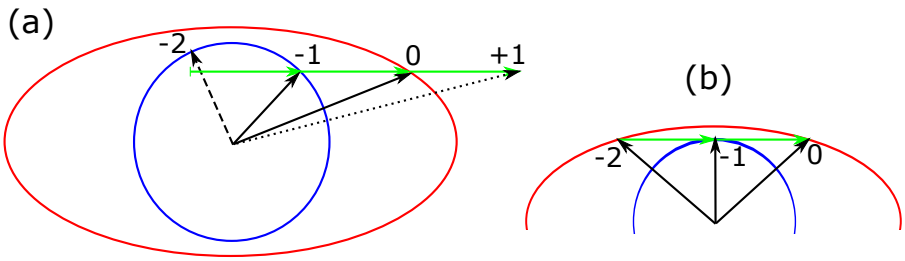

Figure 2.8: Acousto-optic diffraction schematic for TeO_2. The acoustic wavevector is repeatedly displayed in green. The optic wavevectors labelled with their diffraction mode are drawn from the centre in black. The red and blue lines represent the indicatrix for extraordinary and ordinary polarisations (TeO_2 is birefringent) and a particular optic frequency. Therefore only the optic wavevectors ending on these lines can propagate in the crystal. (a) There is strong diffraction into the -1 mode because the 0 mode wavevector minus the acoustic wavevector lies on the blue indicatrix line. There is no diffraction into the $+1$ mode (dotted) because the resultant optic wavevector is far from the red and blue lines. There is some diffraction into the -2 mode (dashed) because the distance from the blue line is small. (b) A single acoustic wavevector can lead to efficient diffraction from the 0 mode into the -2 mode. (Adapted from [1])

plane wave and an acoustic plane wave with frequencies and wavevectors $\omega, \mathbf{k}$ and $\Omega, \mathbf{K}$ respectively. The photo-acoustic effect is such that dipoles are induced whose magnitude per unit volume P is proportional to the product of the acoustic wave and the optic wave [85]: $P \propto \cos(\omega t - \mathbf{k}\cdot\mathbf{r})\cos(\Omega t - \mathbf{K}\cdot\mathbf{r})$. The cosine product can be split up into the sum of two cosines, each corresponding to a different dipole wave:

$$\begin{aligned} & 2\cos(\omega t - \mathbf{k}\cdot\mathbf{r})\cos(\Omega t - \mathbf{K}\cdot\mathbf{r}) \\ = \;& \cos([\omega+\Omega]\,t - [\mathbf{k}+\mathbf{K}]\cdot\mathbf{r}) \\ + \;& \cos([\omega-\Omega]\,t - [\mathbf{k}-\mathbf{K}]\cdot\mathbf{r}) \end{aligned} \tag{2.13}$$

In terms of phase, the two dipole waves are the sum and difference respectively of the incident optic and acoustic waves. Consequently, the induced dipole waves have the frequency/wavevector of the incident optic beam plus and minus the acoustic frequency/wavevector. The dipole waves are not the diffracted waves, but give rise to them by radiating [99]. When the frequency and wavevector of a dipole wave satisfies the dispersion relations of the material, constructive interference will form a diffracted optical wave. In Fig. 2.8(a), the difference between the acoustic wavevector (green) and the incident optical wavevector (0 mode) satisfies the crystal dispersion relation (lies on the blue indicatrix), and thus there is strong diffraction into the -1 mode. If the dispersion relations are nearly but not quite satisfied,

there can still be weak diffraction. For example, in Fig. 2.8(a) the -2 mode wavevector nearly satisfies the dispersion relations indicated by the closeness to the indicatrix (blue line), and therefore the radiation from the dipole waves interferes to produce a weak -2 optical mode. The strength of diffraction into the -1 mode has a *sinc* dependence on the dispersion relation mismatch [85]. In practice, the diffraction efficiency falls off sufficiently quickly for the dipole quantities to be taken as the diffracted quantities:

$$\omega_{\text{diffracted}} = \omega_{\text{incident}} \pm \Omega \tag{2.14}$$

$$\mathbf{k}_{\text{diffracted}} = \mathbf{k}_{\text{incident}} \pm \mathbf{K} \tag{2.15}$$

The $\pm$ in Eq. (2.15) indicates that there are two diffracted waves here. They are said to be the $+1$ and -1 modes respectively. It is not desirable to have both diffracted waves simultaneously but it is possible (Fig. 4 of [83]). Any part of the optical wave passing directly through the AOD undiffracted is called the 0 mode.

Dixon's equations relate the direction of the incident and diffracted optical waves to the acoustic frequency [100]. Their basis is that the frequency shift of Eq. (2.14) is negligible in comparison to the change in the wavevector from Eq. (2.15). The magnitude of the acoustic wavevector is much smaller than the optical wavevectors and is almost perpendicular to the incident optical wavevector. A small angle approximation can therefore be applied: the wavevector triangle Eq. (2.15) is related to the angular deflection of the optic wavevector (not Poynting vector) *inside* the crystal θ_c to the refractive index *inside* the crystal n and the optic wavevector *in vacuum* λ by $\theta_c = \pm\lambda F/Vn$. The small angle approximation of Snell's law can further be applied to find the angle between the incident and diffracted rays *outside* the crystal, recovering Eq. (2.1). Because the refractive index of TeO_2 is large, the angle of deflection as measured in air is much larger than inside the crystal.

The above discussion of an acoustic wave interacting with an optical wave to produce a second (diffracted) optical wave is implicitly making the first Born approximation, and the predicted strength of the diffracted beam is only valid for weak scattering. This is because the diffracted optical wave will itself interact with the acoustic wave, inducing further dipole waves that give rise to more diffracted optical waves. There are two important consequences of this: the $+1/-1$ mode can re-diffract back into the 0 mode or into the higher-order $+2/-2$ mode as shown in Fig. 2.8(b). Diffraction back into the 0 mode means there is a dynamic transfer of optical power between the 0 and $+1$ modes as the optical waves propagate through the AOD. This is accounted for the in the analytic theory presented in [85] and leads to a sinusoidal dependence of diffraction efficiency on transducer width and acoustic drive power.

The diffraction efficiency into higher-order modes is not accounted for in the analytic solution for efficiency given in [85] and leads in practice to an unwanted loss of optical power which increases with drive power. A well-known property of the AOD design used in this thesis is that strong diffraction efficiency into the ± 2 mode occurs at a particular acoustic frequency despite being aligned for the ± 1 mode (see Fig. 2.8(b) and Fig. 4 of [83]). This is undesirable and is minimised by having the transducers optimised for frequencies sufficiently far from this degeneracy. A model presented in [101] was based on the analytic model of [85] and additionally includes loss of power into higher-order modes by making further specific approximations. This model was able to predict the main frequency-dependence of diffraction into the ± 2 mode and the consequent reduction in the strength of the ± 1 mode for TeO_2 AODs.

Several detailed numerical single-AOD efficiency models exist at present: the historical progress can be found in [98] and a notable recent development is [102]. These are, however, more computationally demanding and therefore present challenges for modelling four AODs in series. It is therefore [101] that has most influenced the numerical ray-based model developed Chapter 4 of this thesis.

2.6 KEY AOL LIMITATIONS

The strength of an AOL when compared to competing technologies is that it can perform both fast 3D structural imaging and high-speed selective functional imaging with real-time movement correction. Nevertheless, other technologies outperform AOLs in particular areas. The key AOL limitations presently are as follows:

- AOL-based microscopes have a smaller field of view than a conventional galvo microscope.
  - Use only the X- and Y- AODs for lateral deflections and modulate the amplitude of RF drive signals [62].
- The centre of an AOL microscope's imaging volume is much brighter than the extremities.
  - Amplitude modulation of drive signals has improved this but only for pointing imaging modes [62].
- AOL-microscopes suffer from spherical aberration when focusing away from the front focal plane of the objective.
  - A new AOL design using six AODs has been proposed [3].
- The AOL duty cycle is very low when imaging in pointing mode or using short line-scans.
  - Smaller aperture AODs can be used to reduce fill time but this has the drawback of reducing resolution [3].

Part II

MODELLING AND DEVELOPMENT OF ACOUSTO-OPTIC LENS MICROSCOPY

3

RAY MODELLING OF AN AOL

This Chapter begins by formalising AOL drive theory for the first time: joining together what was already known to form a general theoretical foundation upon which I have developed different strands of AOL drive theory. Once the mathematical rules have been set out, I show there is some freedom when determining drive frequencies and find the size of the AOL microscope imaging volume depends sensitively on how they are chosen.

3.1 RAY TRACING

Prior to the theory I develop here, the derivation of AOL drive equations was performed in 2D and could be (trivially) extended to 3D because the x and y components of curvature are independent, as discussed in Section 2.3.3. The arguments were predominantly geometrical and whilst this gave a clear picture of how the AOL functioned it was difficult to extend generally to 3D.

In this Section, I begin by formalising the constraints required for drive equations by tracing rays through a simplified AOL. Following this, I formalise how the focal position is mapped to the imaging volume in a microscope. Once the rules are established, I show how a particular ray (the base ray) can be identified and used to simplify the calculation of the drive frequencies. This reveals a free parameter for each cylindrical AOL and I examine its effect on spherical AOL performance.

3.1.1 *Recursive ray equation*

Here I set up an equation by tracing rays through an AOL which can be used to determine drive frequencies. An AOL schematic is shown in Fig. 3.1. The acoustic wavevectors are labelled as $\mathbf{K}_n$, which have a fixed direction for each AOD. For a conventional spherical AOL, the acoustic unit vectors are $\hat{\mathbf{K}}_1 = (1,0,0)$, $\hat{\mathbf{K}}_2 = (0,1,0)$, $\hat{\mathbf{K}}_3 = (-1,0,0)$, $\hat{\mathbf{K}}_4 = (0,-1,0)$. However, the derivation here is more general, not only applying to arbitrary acoustic wave directions but also an arbitrary number of AODs. Importantly, the magnitudes of the acoustic wavevectors depend locally on the acoustic frequency and are generally not constant across the AODs. The local magnitude of the acoustic wavevector K can be expressed in terms of the local acoustic frequency F and acoustic velocity V as $K = 2\pi F/V$. Therefore I express the m^{th}AOD's acoustic wavevector $\mathbf{K}_m$, which can vary in magnitude

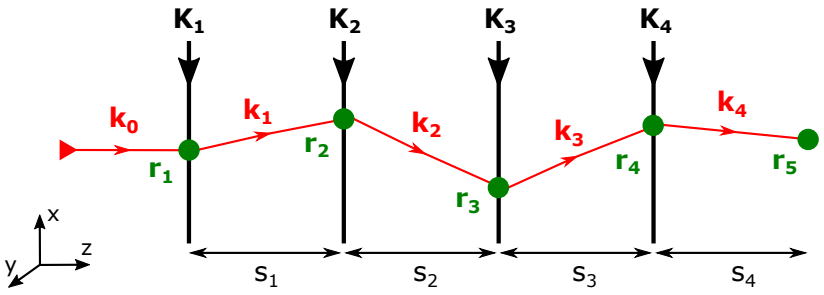

Figure 3.1: Schematic of a spherical AOL. $\mathbf{K}_m$ are the acoustic wavevectors (directions are arbitrary; arrows shown for illustration only), $\mathbf{k}_m$ are the optical ray direction unit vectors, $\mathbf{r}_m$ are positions and s_m are distances along the z-direction. The light passes from left to right so $\mathbf{k}_0$ is the incident beam's direction, usually aligned with the z-axis. All AOD apertures are shown as normal to the z-direction—in a real AOL the AODs are offset from the z-direction by small angles.

across the aperture, as the product of its magnitude and its unit vector:

$$\mathbf{K}_m = \frac{2\pi F_m}{V}\hat{\mathbf{K}}_m \tag{3.1}$$

I traced rays between AODs, denoting the input optical wavevector as $\mathbf{k}_0$ and the optical wavevector following the n^{th} AOD as $\mathbf{k}_n$. If the AODs are operating in the ± 1 mode and deflection angles are small (which they always are), Eqs. (2.1) and (3.1) imply the following relation between optical and acoustic wavevectors:

$$\mathbf{k}_n = \mathbf{k}_{n-1} \pm \mathbf{K}_n \tag{3.2}$$

I denote the intersection point of the ray with the n^{th} AOD by $\mathbf{r}_n = (x_n, y_n, z_n)$, and the spacing between AODs n and $n+1$ by s_n. For an N-AOD system, the $N+1^{\text{th}}$ plane is the focal plane: $\mathbf{r}_{N+1}$ is the intersection point of the ray with the focal plane and s_n is the AOL's focal length. I formulated a recursive equation expressing $\mathbf{r}_{n+1}$ in terms of $\mathbf{r}_n$ and time t:

$$\mathbf{r}_{n+1} = \mathbf{r}_n + \frac{\mathbf{k}_n s_n}{\mathbf{k}_n \cdot \hat{\mathbf{z}}} \tag{3.3}$$

AODs are taken to be thin and normal to the z-axis, the direction of which is given by the unit vector $\hat{\mathbf{z}}$. Acoustic wavevectors therefore have zero z-component $\mathbf{K}_m \cdot \hat{\mathbf{z}} = 0$ and so the z-component of the optical wavevector is constant as it passes through the AOL, $\mathbf{k}_n \cdot \hat{\mathbf{z}} = \mathbf{k}_0 \cdot \hat{\mathbf{z}}$. The acoustic wave is traveling and therefore the acoustic frequency depends on the distance from the transducer and the time:

$$F_m = \mathscr{F}_m\left(t - \frac{[\mathbf{r}_m - \mathbf{R}_m]\cdot\hat{\mathbf{K}}_m}{V}\right) \tag{3.4}$$

where $\mathbf{R}_m$ is a point on the m^{th} AOD's transducer. Taking Eq. (3.3), and recursively substituting in Eqs. (3.2), (3.1) and (3.4) leads to

$$\mathbf{r}_{n+1} = \mathbf{r}_n + \frac{s_n \mathbf{k}_0}{\mathbf{k}_0 \cdot \hat{\mathbf{z}}} \pm \frac{2\pi s_n}{V \mathbf{k}_0 \cdot \hat{\mathbf{z}}} \sum_{m=1}^{n} \mathscr{F}_m \left(t - \frac{[\mathbf{r}_m - \mathbf{R}_m] \cdot \hat{\mathbf{K}}_m}{V} \right) \hat{\mathbf{K}}_m \quad (3.5)$$

Equation (3.5) can be simplified by assuming that the incident wavevector is aligned with the optic axis: $\mathbf{k}_0 = (0, 0, 2\pi/\lambda)$. The result is

$$\mathbf{r}_{n+1} = \mathbf{r}_n + s_n \hat{\mathbf{z}} \pm \frac{\lambda s_n}{V} \sum_{m=1}^{n} \mathscr{F}_m \left(t - \frac{[\mathbf{r}_m - \mathbf{R}_m] \cdot \hat{\mathbf{K}}_m}{V} \right) \hat{\mathbf{K}}_m \quad (3.6)$$

Equation (3.6) above can be used recursively to express, for example, $\mathbf{r}_4$ in terms of $\mathbf{r}_1$ and t. For an N-AOD system, the $N+1^{\text{th}}$ plane is the focal plane: $\mathbf{r}_{N+1}$ is the focal position and s_n is the AOL's focal length. Using Eq. (3.6), $\mathbf{r}_{N+1}$ can be expressed in terms of $\mathbf{r}_1$ and t, and the drive equations for a stigmatic focus moving with velocity $(v_x, v_y, 0)$ can then be derived by applying constraints. For a focus, it is necessary that all rays have the same position in the end plane which implies the functions are unchanged by changing the position of the input ray:

$$\begin{aligned} \frac{\partial x_{N+1}}{\partial x_1} = 0 \quad , \quad \frac{\partial x_{N+1}}{\partial y_1} = 0 \\ \frac{\partial y_{N+1}}{\partial x_1} = 0 \quad , \quad \frac{\partial y_{N+1}}{\partial y_1} = 0 \end{aligned} \quad (3.7)$$

Notice this can be expressed compactly in terms of the Jacobian matrix and the 2×2 matrix of zeros:

$$\frac{\partial (x_{N+1}, y_{N+1})}{\partial (x_1, y_1)} = \begin{pmatrix} 0 & 0 \\ 0 & 0 \end{pmatrix} \quad (3.8)$$

For the focus to be moving with constant velocity (v_x, v_y) the end plane functions must change linearly with t:

$$\frac{\partial x_{N+1}}{\partial t} = v_x \quad \frac{\partial y_{N+1}}{\partial t} = v_y \quad (3.9)$$

The lateral focal velocity (v_x, v_y) is used for continuous line-scanning as shown in Figs. 2.1(a) and (c). By contrast, the velocity is set to zero for pointing, Figs. 2.1(b) and (d). The equations and constraints presented here provide an alternative means to derive the drive equations, Eq. (2.7). The easiest way to do this is to substitute $\mathscr{F}_m(t) = b_m t$, $s_{m<5} = s$, $s_5 = z_{\text{AOL}}$, $\mathbf{r}_1 = (x_1, y_1, -3s)$ and $\hat{\mathbf{K}}_1 = (1, 0, 0), \hat{\mathbf{K}}_1 = (0, 1, 0), \hat{\mathbf{K}}_3 = (-1, 0, 0), \hat{\mathbf{K}}_4 = (0, -1, 0)$ into Eq. (3.6). The vector equation decouples into scalar equations. The z-component satisfies

$z_5 = z_{\mathrm{AOL}}$ by construction. The x and y components are more interesting and simplify to the following set of equations, assuming the AODs operate in the $+1$ mode:

$$\begin{aligned} x_3 &= x_1 + \frac{2\lambda s}{V} b_1 \left(t - \frac{x_1}{V}\right) \\ x_5 &= x_3 + \frac{\lambda(s + z_{\mathrm{AOL}})}{V} \left[b_1 \left(t - \frac{x_1}{V}\right) - b_3 \left(t + \frac{x_3}{V}\right)\right] \\ y_2 &= y_1 \\ y_4 &= y_1 + \frac{2\lambda s}{V} b_2 \left(t - \frac{y_1}{V}\right) \\ y_5 &= y_4 + \frac{\lambda z_{\mathrm{AOL}}}{V} \left[b_2 \left(t - \frac{y_2}{V}\right) - b_4 \left(t + \frac{y_4}{V}\right)\right] \end{aligned} \tag{3.10}$$

Applying the constraints of Eqs. (3.8) (two components trivially satisfied) and (3.9) yields Eq. (2.7). Because the equations for the x and y components are nearly identical, I will only solve the y component here:

$$\begin{aligned} 0 &= \frac{\partial y_4}{\partial y_1} - \frac{\lambda z_{\mathrm{AOL}}}{V^2} \left(b_2 + b_4 \frac{\partial y_4}{\partial y_1}\right) \\ v_y &= \frac{\partial y_4}{\partial t} + \frac{\lambda z_{\mathrm{AOL}}}{V} \left(b_2 - b_4 \left[1 + \frac{1}{V} \frac{\partial y_4}{\partial t}\right]\right) \\ \frac{\partial y_4}{\partial y_1} &= 1 - \frac{2\lambda s}{V^2} b_2 \\ \frac{\partial y_4}{\partial t} &= \frac{2\lambda s}{V} b_2 \end{aligned} \tag{3.11}$$

It requires only a few further lines of algebra to reach expressions for b_2 and b_4. To be clear on the notation in use here $b_1 = b_{\mathrm{X}+}$, $b_2 = b_{\mathrm{Y}+}$, $b_3 = b_{\mathrm{X}-}$, $b_4 = b_{\mathrm{Y}-}$, $x_5 = x_{\mathrm{AOL}}$, $y_5 = y_{\mathrm{AOL}}$. I have neglected to consider a_1, a_2, a_3, a_4 here because these can be calculated independently of b_1, b_2, b_3, b_4, where each a and b are defined by Eq. (2.2). How the values of a_1, a_2, a_3, a_4 are constrained and optimally chosen is explored in Sections 3.1.3 and 3.1.4.

3.1.2 *Focal position mapping by post-AOL optics*

So far, I have discussed the focal trajectory produced by an AOL in isolation. In an AOL microscope, after leaving the last AOD of the AOL, the optical beam is relayed by a 4f relay of magnification M to the rear focal-plane of an infinity-corrected objective. These three stages are illustrated in Fig. 3.2. Here I set out the relations between these focal trajectories.

For clarity, I denote the focal position that would be produced by the AOL alone by $(x_{\mathrm{AOL}}, y_{\mathrm{AOL}}, z_{\mathrm{AOL}})$, where $x_{\mathrm{AOL}}, y_{\mathrm{AOL}}$ are measured from the centre of the last AOD and z_{AOL} is measured from

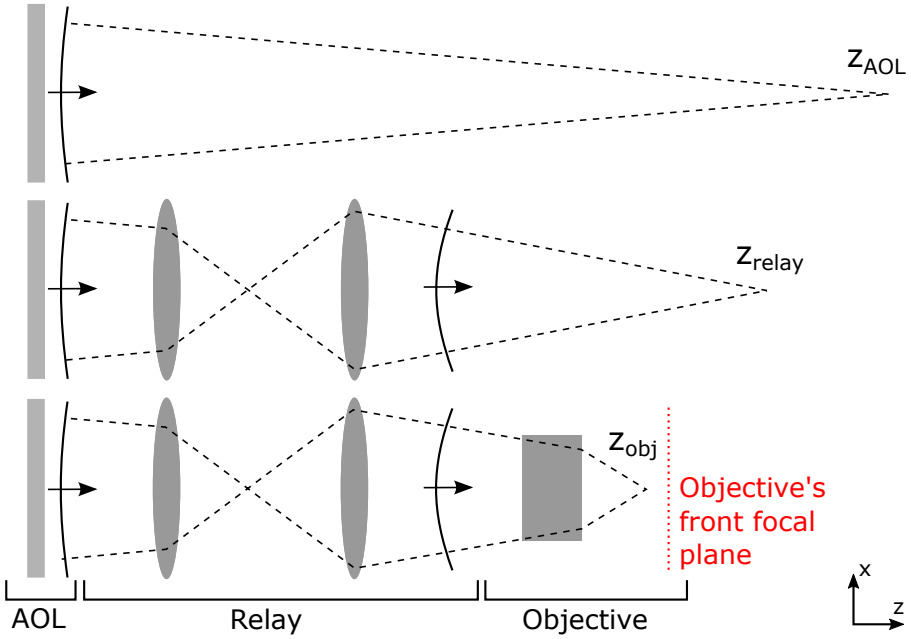

Figure 3.2: AOL microscope focal position mapping. Top: an AOL produces a focal point z_{AOL}. Middle: a relay is added after the AOL which maps the focal point z_{AOL} to a new position z_{relay}. Bottom: an infinity-corrected objective is added after the relay which maps the focal point z_{relay} to a new position z_{obj} relative to the objective's front focal plane .

the last AOD. These correspond to $\mathbf{r}_{N+1} = (x_{N+1}, y_{N+1}, z_{N+1})$ for an N-AOD AOL in Eq. (3.6). The focal position of the AOL is then mapped by a 4f relay of magnification M to a new position denoted $(x_{\text{relay}}, y_{\text{relay}}, z_{\text{relay}})$. The effect of the relay is to scale the lateral and axial focal positions:

$$x_{\text{relay}} = -Mx_{\text{AOL}} \qquad y_{\text{relay}} = -My_{\text{AOL}} \qquad z_{\text{relay}} = M^2 z_{\text{AOL}} \tag{3.12}$$

The objective then further, significantly alters the focal position to $(x_{\text{obj}}, y_{\text{obj}}, z_{\text{obj}})$, where $x_{\text{obj}}, y_{\text{obj}}$ are measured from the optic axis of the objective and z_{obj} is the displacement from the objective's front focal plane. The effective front focal length of the water-immersion objective is $f_{\text{obj}} = n \times$ tube lens focal length$/$magnification, where n is the refractive index of water and magnification refers to the magnification of the objective rather than the relay. The post-objective axial focal position z_{obj} (which is relative to the front focal plane of the objective) can be approximated by applying the thin lens equation:

$$\begin{aligned}\frac{1}{z_{\text{obj}}+f_{\text{obj}}} &= \frac{1}{f_{\text{obj}}}+\frac{1}{nz_{\text{relay}}-f_{\text{obj}}}\\ z_{\text{obj}} &= \frac{-f_{\text{obj}}^2}{n}\frac{1}{z_{\text{relay}}}\\ &= \frac{-f_{\text{obj}}^2}{M^2 n}\frac{1}{z_{\text{AOL}}}\end{aligned} \tag{3.13}$$

The thin lens equation is only applicable to the paraxial rays passing through the objective. For large displacements the focal point will be spherically aberrated and consequently the effective position is displaced slightly from z_{obj}. The lateral focal position depends on the AOL's axial focal position in addition to its lateral focal position:

$$\begin{aligned}x_{\text{obj}} &= \frac{z_{\text{obj}}+f_{\text{obj}}}{nz_{\text{relay}}-f_{\text{obj}}}x_{\text{relay}}\\ &= \frac{f_{\text{obj}}x_{\text{relay}}}{nz_{\text{relay}}}\\ &= \frac{-f_{\text{obj}}x_{\text{AOL}}}{Mnz_{\text{AOL}}}\end{aligned} \tag{3.14}$$

and an analogous equation also holds for y_{obj}.

Note that in the limit that the AOL focuses at $z_{\text{AOL}} \to \infty$ (rays leaving the AOL are parallel), the post-AOL optics still bring the beam to a focus. In this case it is the well-defined limits $\Theta_x = x_{\text{AOL}}/z_{\text{AOL}}$ and $\Theta_y = y_{\text{AOL}}/z_{\text{AOL}}$ that determine the lateral focal positions: Θ_x and Θ_y are proportional to x_{obj} and y_{obj} respectively. Because Θ_x and Θ_y are small, they can be interpreted as deflection angles (in radians) as measured from the centre of the last AOD to the focal point. A special point is $\left(\Theta_x = 0,\, \Theta_y = 0,\, z_{\text{AOL}} = \infty\right)$ which corresponds to the centre of the imaging volume $\left(x_{\text{obj}} = 0, y_{\text{obj}} = 0, z_{\text{obj}} = 0\right)$.

The above calculations require particular distances between the second AOD of the cylindrical AOL and the objective. In a compact AOL, which has four AODs arranged as two, orthogonal cylindrical AOLs, only one of the cylindrical AOLs can be the correct distance from the objective. In practice, this is not a problem because the AOL focal length is typically no less than 50 cm, whilst the separation between the AODs is only 5 cm. The relatively small distance between the AODs means that to a good approximation both of the cylindrical AOLs are mapped to the objective's (paraxial) rear focal-plane.

To summarise the mapping of AOL focal trajectories to microscope focal trajectories, the microscope lateral focal position is proportional to the ratio of AOL lateral and axial focal positions (the deflection angle, since angles are small). Furthermore, the microscope axial focal position is proportional to the curvature of the beam leaving the AOL.

For linear chirps, the AOL focal trajectory is necessarily constant-velocity lateral scanning which corresponds to constant-velocity lateral scanning of the microscope focus. For nonlinear chirps, axial scanning is also possible and more careful consideration of the relations is required.

3.1.3 *The base ray*

To drive an AOL, first the linear chirps (b) are calculated from the drive equations Eq. (2.7), and then the centre frequencies (a) are determined (the frequencies at $t = 0$ of the ramps). I introduce the base ray as an approach to ease the calculation of centre frequencies. I define the base ray as the ray at $t = 0$ that intersects each AOD at its acoustic frequency ramp centre (experiences frequency a). This definition practically amounts to assuming that the AOD transducers are located at the centre of the AODs. This assumption is not at all a problem since frequency ramp power series can be translated after their calculation to account for the real physical location of the AOD transducers. Subsequent algebra is made simpler if the base ray intersection points with the AODs are taken as lateral coordinate system origins, which is similar to the idea of an optical system base ray [103], hence the name. It is important to notice that the base ray depends on the centre frequency on each of the AODs so that the relationship between base rays and AOLs is many-to-one.

The acoustic frequency F encountered by the base ray at each AOD at $t = 0$ is by definition the centre frequency of that AOD's drive ramp a. This directly relates the AOL's lateral focal displacement to the drive ramp centre frequency. By applying Eq. (2.1) to the base ray, I determined the relationship between the centre frequencies of each AOD (a_+ and a_-) and the lateral deflection angle of a cylindrical AOL:

$$\Theta = \frac{x_{\mathrm{AOL}}}{z_{\mathrm{AOL}}} = \pm\frac{\lambda}{V}\left[(a_+ - F_0)\left(1 + \frac{s}{z_{\mathrm{AOL}}}\right) - (a_- - F_0)\right] \tag{3.15}$$

where s is the separation between the AODs, z_{AOL} is the distance from the last AOD to the focal point and F_0 is the optimal frequency of the AODs discussed in Section 2.3.1. The $\pm$ signs are decided by whether the AODs are diffracting into the $+1$ or -1 mode. For experiments and simulations reported in this thesis the AODs use the -1 diffraction mode.

Equation (3.15) can be applied to a spherical AOL by considering it as two orthogonal cylindrical AOLs with AOD spacing $2s$ offset axially by distance s, the first aligned in the x-direction and the second in the y-direction. When the AODs in an AOL are all driven at F_0, there is no focusing ($z_{\mathrm{AOL}} = \infty$) and the lateral angle is zero ($\Theta_x = 0, \Theta_y = 0$), in agreement with Eq. (3.15). Equation (3.15) has

two free parameters a_+, a_- so there is a degree of freedom when choosing the centre frequencies for a cylindrical AOL. This can be understood as follows: if the drive frequency of the first AOD in a cylindrical AOL increases then increasing the drive frequency of the second will counteract this change by deflecting the base ray in the opposite direction. Therefore there are two degrees of freedom when choosing the centre frequencies for a spherical AOL, which is effectively two cylindrical AOLs.

3.1.4 *Pair deflection ratio* $\mathcal{R}$

The focal position of an AOL microscope has both lateral and axial displacements. The mean lateral focal displacement induced by a set of frequency ramps can be varied independently of focal length by adjusting the ramp centre frequencies (a). Such lateral displacements can be seen by comparing the frequency ramps of Fig. 3.3(a)–(c) with their corresponding ray diagrams in Fig. 3.3(d). The paths taken by the purple, cyan and orange rays in Fig. 3.3(d) (artificially coloured; all of 800 nm wavelength) correspond to a compact AOL being driven with the ramps shown in Figs. 3.3(a), (b) and (c), respectively. Importantly the cyan and orange rays focus at the same point despite taking different paths through the AOL. This illustrates that there is some freedom when choosing the centre frequencies. Here I quantify the degree of freedom by defining the pair deflection ratio, denoted $\mathcal{R}$.

In a cylindrical AOL, the base ray is deflected by angles θ_+ at the first AOD and θ_- at the second AOD, which are determined by the centre frequencies of the AODs. As discussed in Section 2.3.1, AODs are manufactured to operate optimally at a particular frequency F_0. The AODs considered in this thesis (mostly) have $F_0 = 39$ MHz. By Eq. (2.1) this frequency corresponds to an *optimal deflection angle* $\theta_0 = \lambda F_0 / V$. Thus, it can be more effective to consider angular deflections *relative* to this optimal deflection angle rather than the absolute deflection angles θ_+, θ_-. For a cylindrical AOL with AODs operating in the -1 mode, the top of Fig. 3.3(e) shows the base ray first deflected down by θ_0 at X+ and then back up by θ_0 at X- such that it is parallel with its initial direction. The bottom of Fig. 3.3(e) shows how changing the frequencies from $(a_+ = F_0, a_- = F_0)$ to $(a_+ = F_+, a_- = F_-)$ incrementally changes the deflection angles. The relative angular deflections of the base ray at the first ($\delta\theta_+$) and second ($\delta\theta_-$) AODs are given by

$$\delta\theta_\pm = \theta_0 - \theta_\pm = \frac{\pm\lambda\,(F_0 - a_\pm)}{V} \tag{3.16}$$

where the sign difference is due to the acoustic wave on the first AOD propagating in the opposite direction to the acoustic wave on the second AOD (nothing to do with diffraction modes; -1 has been assumed).

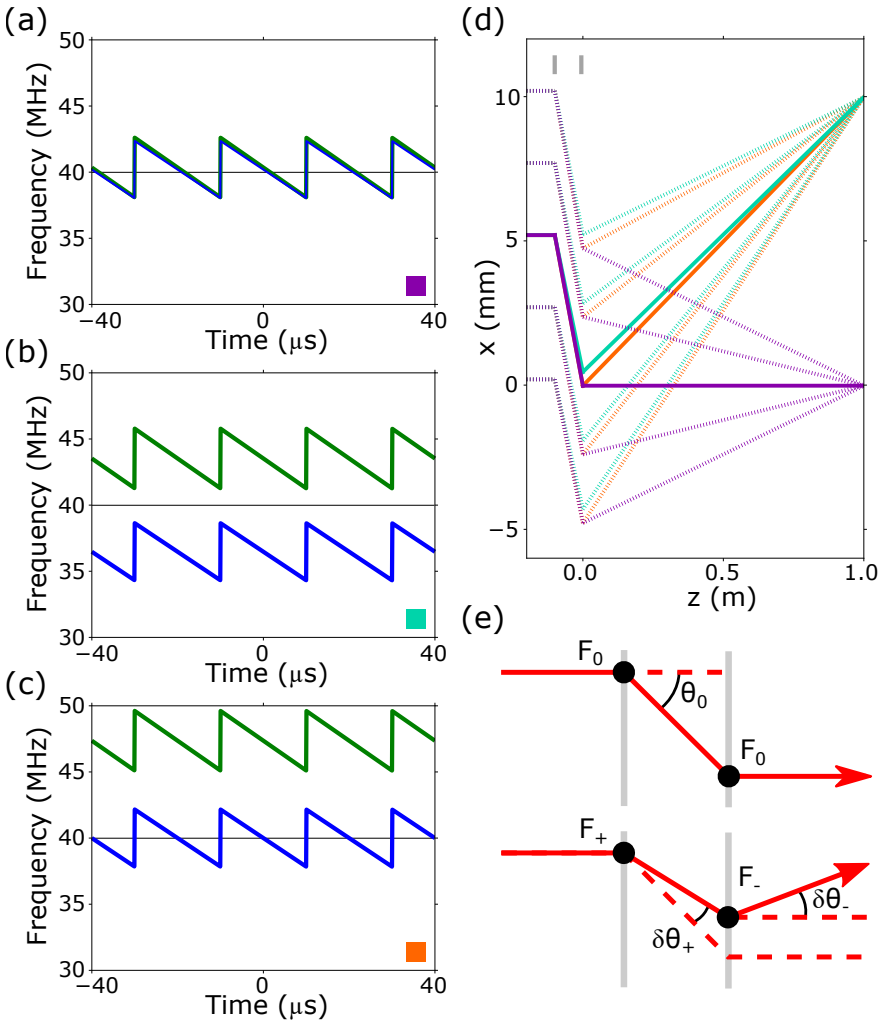

Figure 3.3: (a)–(c) Sequences of acoustic frequency ramps used to drive the two AODs that make up a cylindrical AOL. The colour indicates which AOD the ramp is for: X+ blue; X- green. For AODs operating in the -1 diffraction mode, the ramps cause the AOL to focus at (a) (0,1); (b) (0.01,1); (c) (0.01,1) m. Note the focal lengths are all the same ($z_{\mathrm{AOL}} = 1$ m) for (a)–(c) because the ramp gradients are unchanged. (d) Comparison of light ray paths through the AOL (purple, cyan and orange) when driven with the ramps shown in (a), (b) and (c), respectively. Note the cyan and orange rays take different paths but focus at the same point. The short grey lines indicate AOD z-positions. (e) Base ray passing through a pair of anti-parallel AODs to illustrate Eqs. (3.16) and (3.17). (Adapted from [1])

To express the degree of freedom in terms of the frequencies $a_\pm$ experienced by the base ray, I define the pair deflection ratio $\mathcal{R}$ as the ratio of the base ray's deflection at the first AOD to the deflection at the second AOD:

$$\mathcal{R} = \frac{\delta\theta_+}{\delta\theta_-} = \frac{F_0 - a_+}{a_- - F_0} \tag{3.17}$$

I had assumed AODs diffracted into the -1 mode. However, because relative deflection angles were used, Eq. (3.17) is also valid for cylindrical AOLs using $+1$ mode diffraction too. To calculate the drive frequencies for a chosen value of $\mathcal{R}$ when the AODs in a cylindrical AOL diffract into the ± 1 mode, I solve Eqs. (3.15) and (3.17) simultaneously to find

$$\begin{aligned} a_+ &= F_0 \pm \frac{V}{\lambda} \frac{\mathcal{R} x_{\mathrm{AOL}}}{\mathcal{R}\,(s + z_{\mathrm{AOL}}) + z_{\mathrm{AOL}}} \\ a_- &= F_0 \mp \frac{V}{\lambda} \frac{x_{\mathrm{AOL}}}{\mathcal{R}\,(s + z_{\mathrm{AOL}}) + z_{\mathrm{AOL}}} \end{aligned} \tag{3.18}$$

This derivation assumed the AOD transducers were located at the point that the intersect the base ray. In practice, the frequency power series must be shifted from the base ray positions to the actual transducer positions, using the relation between time and space for the acoustic waves: if $\mathcal{F}(t)$ has been calculated at the base ray displaced from the physical location of the transducer by Δ, the chirp coefficients at the transducer can be calculated by expanding $\mathcal{F}(t \pm \Delta/V)$ and equating coefficients ($\pm$indicates the direction of the acoustic wave).

A special case is pointing with $\mathcal{R} = 1$ focused at $z_{\mathrm{obj}} = 0$ (the limit $z_{\mathrm{AOL}} \to \infty$); to image a line, the drive frequency is incremented discretely to image point-by-point. In the limit that time between discrete frequency steps goes to zero and distance (angular separation) between discrete spatial points goes to zero, a single linearly-chirped ramp is recovered which corresponds to line-scanning at $z_{\mathrm{obj}} = 0$. For drives using $\mathcal{R} \neq 1$ at $z_{\mathrm{obj}} = 0$, the limiting linearly-chirped ramps would add different amounts of curvature such that the line-scanning was at $z_{\mathrm{obj}} \neq 0$. Thus, we would expect the AOL microscope's field of view to be very comparable when using pointing and line-scanning at $z_{\mathrm{obj}} = 0$, as has been noted previously [61].

Finally, I remark that a spherical AOL has a ratio for each of its two orthogonal cylindrical AOLs, which can be set independently:

$$\mathcal{R}_x = \frac{F_0 - a_{\mathrm{X}+}}{a_{\mathrm{X}-} - F_0}, \qquad \mathcal{R}_y = \frac{F_0 - a_{\mathrm{Y}+}}{a_{\mathrm{Y}-} - F_0} \tag{3.19}$$

In practice however, what is good for $\mathcal{R}_x$ is good for $\mathcal{R}_y$ so invariably they are taken to be equal: $\mathcal{R} = \mathcal{R}_x = \mathcal{R}_y$. The rest of this Chapter describes how the performance of a compact AOL depends on the

ratios, which I have explored using both a ray-based computer model (the development of which is described in detail in Chapter 4) and experimental measurements from an AOL microscope.

3.2 EFFECT OF PAIR DEFLECTION RATIO ON AOL PERFORMANCE

Using both a computer model and experimental measurements, I examine how the pair deflection ratio affects the field of view of an AOL microscope when operating in full-frame pointing mode to image in the objective's front focal plane. I then make further experimental measurements to determine its effect on the microscopes entire imaging volume in pointing mode.

3.2.1 *Spherical AOL field of view dependence on $\mathcal{R}$*

To understand how AOL field of view varies with $\mathcal{R}$ in pointing mode, I compared the predictions from my computer model of an AOL (see Chapter 4 for details of the model) with experimental measurements of AOL efficiency using a 3D two-photon AOL microscope. To do this I predicted the intensity of two-photon fluorescence at $z_{\mathrm{AOL}} = \infty$. An AOL focal position at $z_{\mathrm{AOL}} = \infty$ corresponds to the AOL microscope focusing at $z_{\mathrm{obj}} = 0$, where z_{obj} is the axial position after passing through an infinity-corrected microscope objective relative to its front focal plane. To approximate the relationship between z_{AOL} and z_{obj} for the post-AOL optical arrangement I used $z_{\mathrm{obj}} = 140 \times 10^{-6}/z_{\mathrm{AOL}}$ where z_{obj} and z_{AOL} are both in metres.

Figure 3.4 compares the simulated fluorescence intensity (calculated as the fourth power of the optical field to account for two-photon excitation, normalised) and experimentally measured intensity of a uniform fluorescent sample [104] over the field of view (expressed as the x-axis and y-axis deflection angles, Θ_x and Θ_y) for a wide range of ratios at an excitation wavelength of $\lambda = 920$ nm. The region of high transmission efficiency (white areas in Fig. 3.4) predicted by my AOL model agreed closely across the full range of ratios spanning $+5$ to -5. The peak fluorescence intensities are all at the centre because that point corresponds to the AODs all being driven at the optimal frequency F_0 and is independent of $\mathcal{R}$.

Comparison of the top two rows shows that the region of high transmission efficiency is bell-shaped and its area progressively increases as the ratio is reduced from +5 to 0.5. However, for $\mathcal{R} = 0$ the shape of the region of efficiency became more complex both in the model and in the experimental measurements (Fig. 3.4). The horizontal and vertical troughs at around -1 degree correspond to a drop in acoustic power for the narrow transducer at around 28 MHz (discussed in Chapter 4 and visible in Fig. 4.2). The central region is extended in the x-axis more than in the y-axis so the image does not

have a diagonal line of symmetry. This was due to X- and Y- being aligned at slightly different angles and I confirmed this by observing X- or Y- could be rotated to restore the diagonal line of symmetry to the region of high transmission efficiency (data not shown).

I extended my investigation to values below $\mathcal{R} = 0$ to test the validity of my model. These results show close agreement between the results from the AOL model and the experimental measurements in this region. The value of -1 is missing because it is not physically achievable due to perfect cancellation of the X+ and X- deflection. From Fig. 3.4 I anticipated that a ratio between 0 and 0.5 would be best and found $\mathcal{R} = 0.3$ gave the widest central high efficiency region.

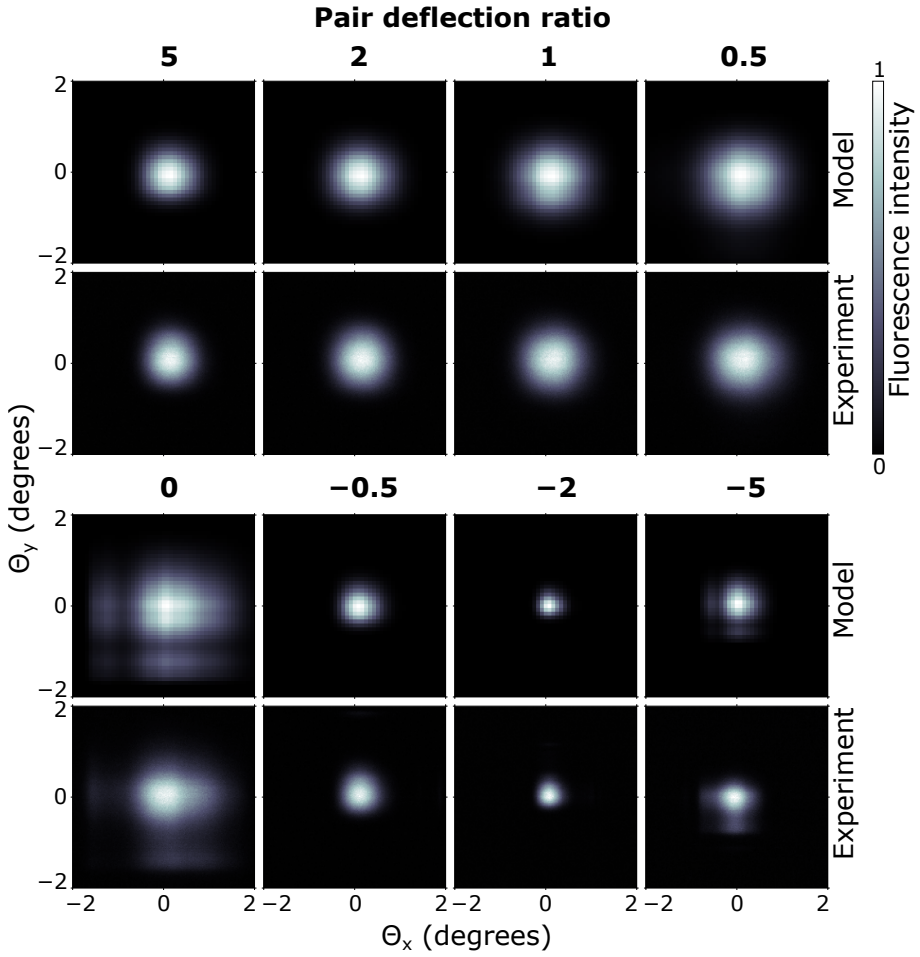

Figure 3.4: Comparison of simulated fluorescence intensity over the field of view (model; first and third rows) with experimentally measured fluorescence intensities (experiment; second and fourth rows) for the pair deflection ratios 5, 2, 1, 0.5, 0, -0.5, -2, -5 (shown in bold). Fluorescence intensity values were normalised to the peak value. Excitation wavelength 920 nm. Each plane is described by the AOL's lateral deflection of the optical beam, Θ_x and Θ_y—see Eq. (3.15). (Published in [1])

3.2.2 *Dependence of imaging volume on $\mathcal{R}$*

In order to evaluate how AOL microscope imaging volume depends on $\mathcal{R}$ in pointing mode, I imaged a uniform fluorescence preparation at a range of different focal depths using the AOL microscope. The volumes are shown as z-stacks in Figs. 3.5(a)–(c). In Fig. 3.5(a) I use a large ratio of 5, corresponding to X+ and Y+ contributing most of the lateral deflection. The central plane ($z_{\text{obj}} = 0$) is brightest and the area of the bright regions narrows slightly at the bottom. Figure 3.5(b) is for $\mathcal{R} = 0.3$, corresponding to X- and Y- contributing most of the lateral deflection. The central plane is brightest again and the shape of the bright regions is nearly constant throughout the volume. Figure 3.5(c) is for $\mathcal{R} = -2$, corresponding to X- and Y- contributing a negative amount of the lateral deflection and X+ and Y+ having to contribute over 100% of lateral deflection to compensate. The area of the bright regions is small in comparison and increases with z_{obj}.

From a series of these z-stacks I calculated the dependence of the AOL microscope imaging volume on $\mathcal{R}$, where I defined the imaging volume boundary as 60% of peak fluorescence intensity. The dependence of imaging volume on $\mathcal{R}$ is shown in Fig. 3.5(d). I observed a peak in imaging volume at $\mathcal{R} = 0.3$ and a sharp fall in the vicinity of -1 (-1 is not physically possible as mentioned in Section 3.2.1). These results demonstrate the sensitivity of AOL performance on $\mathcal{R}$ and confirm my model's prediction that using X- and Y- to contribute the majority of the lateral deflection is advantageous for the compact AOL design.

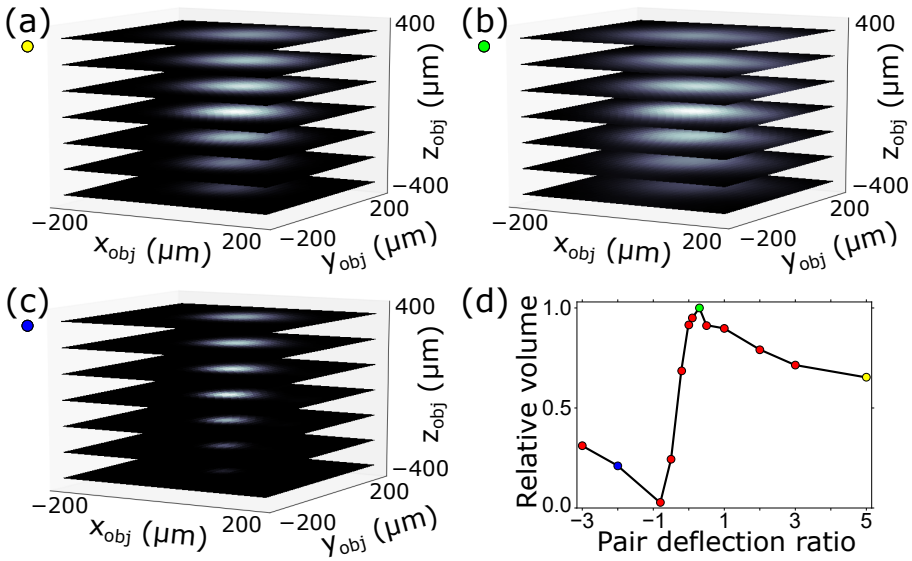

Figure 3.5: AOL microscope z-stacks for (a) $\mathcal{R} = 5$, (a) $\mathcal{R} = 0.3$ and (b) $\mathcal{R} = -2$. Fluorescence intensity in arbitrary units. (d) Relationship between AOL microscope imaging volume and $\mathcal{R}$. AOL microscope imaging volume boundary defined as 60% of peak fluorescence. The peak is at $\mathcal{R} = 0.3$. The yellow, green and blue dots identify the volume shown in three z-stacks (a)–(c) on the plot (d). Optical wavelength 920 nm. (Published in [1])

3.3 DISCUSSION

The recursive ray equation Eq. (3.6) that I derived in this Chapter can be applied to find the drive equations of [61], Eq. (2.7). The recursive ray equation is intrinsically 3D making it applicable when AODs are not orthogonal. Additionally, it can handle nonlinear drive frequency chirps. This is in contrast with the geometric approach, which assumed orthogonal AODs and linear chirps. However, a practical limitation of the recursive ray equation is that it is too long to manipulate by hand for all but the simplest AOD arrangements. One recourse is to realise the constraints I have used are stronger than necessary. Because brief frequency ramps are used, the derivatives need only be locally zero. That is to say, it should be sufficient to have the first-derivatives (and optionally the second-derivatives and third-derivatives and so on) evaluated at $t = 0$ equal to zero, rather than the derivative be zero for all t. Weaker constraints are used in Chapter 6, which explores nonlinear frequency chirps for a cylindrical AOL. Another approach is to restrict the equation to linear chirps as I have done in Chapter 8.

I have derived simple expressions relating the AOL focal position to the microscope focal position. This is important because it is microscope focal trajectories that are useful for experiments, but AOL focal trajectories which are directly determined by drive frequencies.

A special case worth remembering due to its repeated appearance is that constant velocity lateral scanning of the AOL focus corresponds to constant velocity lateral scanning of the microscope focus. However, constant velocity axial scanning of the microscope focus does not correspond to constant velocity axial scanning of the AOL focus, instead it corresponds to AOL curvature varying linearly in time. For any microscope focal trajectory (such as those considered in Chapter 6) the relations I have derived will determine the required AOL focal trajectory.

When calculating the centre frequencies of the AOD drive ramps, I have found considering a particular ray (the base ray) greatly simplifies calculations. An implicit assumption in the frequency chirp power series calculated using the base ray is that the AOD transducers are located at their respective points of intersection with the base ray, which is never true in reality. This is easily remedied after calculating the frequency power series by translating it in time to compensate for the actual transducer positions.

Application of the base ray to an AOL has revealed that there is a degree of freedom in centre frequencies. I have called this degree of freedom the pair deflection ratio and given it the symbol $\mathcal{R}$. The pair deflection ratio is a measure of the amount of deflection contributed by the first and second AOD of each X or Y anti-parallel pair. I have explored how AOL optical transmission depends on $\mathcal{R}$ and found experimentally that a value of 0.3 maximised the volume for the compact AOL design. I simulated the field of view dependence on $\mathcal{R}$ using a numerical AOL model (developed in Chapter 4) and measurements with a two-photon compact AOL microscope confirmed the model's predictions.

My results show the way in which the AODs are driven strongly affects the size of the volume that can be imaged with an AOL microscope. The optimal value of $\mathcal{R} = 0.3$ implies that deflecting predominantly with the last two AODs provides the best transmission efficiency characteristics for the compact AOL design. Fixing the value of $\mathcal{R}$ is a new simple rule that I have used to achieve a near-optimal field of view. Alternatively, optimal AOD drive frequency can be determined on a voxel by voxel basis. However, this 'optimised frequency limits' approach [105] is far more complicated to implement than simply fixing $\mathcal{R}$. Another lab has reported using only the last two AODs (X-,Y-) for lateral deflections to maximise the field of view [62] which is $\mathcal{R} = 0$ in the nomenclature of this thesis. This is consistent with my results, taking into account differences between the AOL designs and the AODs used.

I have explored the effect of the pair deflection ratio on pointing mode (see Fig. 2.1). However, $\mathcal{R}$ is also applicable to line-scanning mode. When the focus moves continuously in y and is stationary in x as typical for full-frame imaging, $\mathcal{R} = 0.3$ for the X+, X- AOD

pair would provide the largest imaging volume. The y-scan would be centred at $\Theta_y = 0$ and so the Y+, Y- pair would be driven at the optimal frequency, F_0, irrespective of $\mathcal{R}$.

4

MODELLING AOL TRANSMISSION EFFICIENCY

This Chapter examines the transmission efficiency of an AOL microscope in the 3D imaging region (the diffracted optical power as a fraction of incident optical power). Previous AOL models have exclusively focused on phase: how to choose the drive frequencies to produce a stigmatic focus at a known location. When illuminating a fluorescent sample with a two-photon AOL microscope, it is not enough to have the focus in the correct position: the illumination must be intense enough to excite the fluorophores and produce a signal greater than the background noise. To address this, I have designed the first AOL model that numerically calculates the optical transmission efficiency. The two-photon fluorescence excitation can subsequently be calculated as the square of the optical intensity. The model is based on a well-documented model of a single AOD. I tuned the model using experimental data, which I collected specifically for the model. Several model predictions are then confirmed experimentally with further data collected using an AOL microscope, which suggests the main factors determining AOL performance are known.

4.1 NUMERICAL MODEL

I have developed a ray-based numerical model of light transmission efficiency through a compact AOL. There were four reasons for doing this. First, to gain a better understanding of AOLs. Second, it is difficult to experimentally optimise multiple AOL parameters when they can take a large range of values. Third, it takes a long time and lot of work to set up a new AOL. Fourth, it is not possible to try variations of AOD design without great expense and delay getting them manufactured. The model has suggested three improvements and will be useful for deciding future AOD designs.

The size of an AOL microscope's imaging volume is of practical importance and depends on many factors. For example, a continuum of AOL drive configurations are possible for focusing at the same point. However, it is not feasible to experimentally explore all these factors in a brute force fashion and quantitative predictions have been difficult due to the lack of a theoretical model. To date, predicting AOL performance has relied on models of single AODs, the thin lens equation and geometrical considerations [58, 59, 61, 62]. The most detailed model of a single AOD was developed in [102] and relies on intensive numerical computations. Approximate closed form expressions for AOD diffraction efficiency and angular deflection are provided in

[85]. The model developed in [101] extends [85] and considers two orthogonally arranged AODs. All three of these models assume the AODs are driven with constant frequency and this means they cannot be used to simulate a spherical AOL with finite focal length because focusing requires four AODs to be driven with linear frequency chirps.

To develop a quantitative description of optical transmission efficiency through a compact AOL I have developed an experimentally constrained model using a novel ray-based approach. This has allowed me to systematically explore how the different drive configurations affect optical transmission efficiency over 3D space and thus determine the imaging volume. My model-based simulations indicate that imaging volume depends sensitively on how lateral deflection is divided between the first two AODs (X+ and Y+) and the last two AODs (X- and Y-), which I have confirmed experimentally with a 3D two-photon AOL microscope.

I developed a computer model of a spherical AOL [4], where each of the four AODs is treated similarly to the approach developed in [101]. My AOL model has extended the work of [101] in three important respects as detailed in Table 4.1. Time-varying drive frequencies were handled by dividing the optical beam into rays. At every AOD, each ray was approximated as a plane wave interacting with a constant frequency acoustic wave. The frequency of the acoustic wave was taken as the local, instantaneous frequency at the ray's point of incidence with the AOD. The justification for this is that the optical field behaves locally as a plane wave [99], and the diffraction angle for each ray depends only on the local, instantaneous acoustic frequency [58]. Each ray can then be treated at each AOD with the model detailed in [85]. Thus, by dividing up the beam into N rays, I effectively replaced each non-constant drive frequency AOD with N (smaller) AODs with constant drive frequencies. For the purposes of this work I have found $N = 25$ to be a good trade-off between precision and computation speed.

The reason that I have broken up arbitrary wavefronts into multiple plane waves via rays instead of attempting to deal with them using Fourier methods is because of the nonlinearity of the acousto-optic interaction. From the Fourier perspective, optical plane waves interact with acoustic plane waves via Eq. (2.15). For constant acoustic frequencies, crystal dispersion relations ensure that each incident optical wavevector diffracts into only one diffracted optical wavevector (for a given mode). When a linearly-chirped acoustic wave is used, the relation becomes one to many and the process is no longer linear due to interactions between the multiple coupled diffracted wavevectors for each incident wavevector. Rays linearise the problem by using the local acoustic frequency and thus reduce an arbitrary chirp problem to a constant frequency problem. The benefit of rays is that they pro-

vide a localised representation of the optical wave. My hope is that a partially-localised wave representation such as the Wigner function which has a close correspondence with rays [106] may lead to a linear solution but I have not succeeded in discovering such a solution.

Table 4.1: Comparison of ray-based model with the model detailed in [101]. (Published in [1])

[101] **Model**	**Ray-based Model**
2 AODs	any number of AODs
constant frequency	time-varying frequency
efficiency only	efficiency and ray tracing

For a given focal position, my model calculates the drive frequencies across each AOD for a sequence of times. To model light propagating through an AOL, a bundle of rays is generated and passed through each AOD. The energy of each ray is calculated after each AOD. I used my model to predict the two-photon fluorescence over a region of space by summing the energy of the rays after the last AOD and squaring the total to account for the quadratic dependence of two-photon excitation on optical power. This left an unknown constant of proportionality, which I removed by normalising all model predictions of fluorescence so that the peak has a value of 1.

My computer model of an AOL is conceptually simple: rays propagate through each of the AODs and the intervening spaces of the AOL. For each AOD I modelled the following three processes

- Refraction into the AOD, accounting for the anisotropy of the AOD.
- Acousto-optic diffraction inside the AODs: calculation of the diffracted optic wavevector, diffraction efficiency and secondary diffraction effects (the diffracted wave re-diffracting).
- Refraction out of the AOD, again, accounting for the anisotropy of the AOD.

To calculate the refraction in and out of each AOD, I used the values for refractive indices and optical activity for TeO_2 given in [94]. For acousto-optic diffraction, the wavevector of the diffracted optic wave is calculated from the sum of the incident optic wavevector and acoustic wavevector. I calculated diffraction efficiency, η, between neighbouring modes using the following equation given in [85]:

$$\eta = u^2 \left(\sin\sigma/\sigma\right)^2 \tag{4.1}$$

$$\sigma = \left(\zeta^2 + u^2\right)^{1/2}, \qquad \zeta = -\tfrac{1}{2}\Delta k\, L, \qquad u = \frac{\pi}{2\lambda} L n_o^{3/2} n_e^{3/2} pS$$

where λ is the optical wavelength in vacuum; n_o is the ordinary refractive index; n_e is the extraordinary refractive index; p is the elasto-optic coefficient; S is the sound amplitude; Δk is the wavevector mismatch (the diffracted optic wavevector plus the acoustic wavevector minus the incident optic wavevector); and L is the effective width of the transducer. The value of the elasto-optic coefficient, p, was taken from Appendix E of [85].

Following Section 2.5 in [101], I made approximations to account for secondary diffraction into the -2 mode as shown in Fig. 2.8(b) by using the following equation:

$$\widetilde{\eta}_1 = \eta_1 \left(1 - \alpha \eta_2\right) \tag{4.2}$$

where $\widetilde{\eta}_1$ is the diffraction efficiency into the -1 mode, corrected for secondary diffraction; η_1 is the diffraction efficiency from the 0 mode into the -1 mode calculated using Eq. (4.1); η_2 is the simplified diffraction efficiency from the -1 mode into the -2 mode calculated using Eq. (4.1); α is a parameter that determines the strength of the secondary diffraction, estimated from experimental data and discussed in the next section.

My model does not include polarisation effects. I neglect these because the optical polarisation inside the AODs depends only on the ray directions relative to the optic axis and these will not vary much. My calculations indicate that ray angles to the optic axis (inside the AOD crystal) will vary between 2° and 0° with the input polarisation optimised for 1° and output polarisation optimised for 0.6°. Using Fig. 1 of [93] I find the actual polarisation of rays varies between perfectly circular and 90% ellipticity. The input polarisation for each AOD is configured to be nearly circular (95% ellipticity) and the polarisation mismatch will therefore be insignificant.

4.1.1 *Tuning AOD properties in the computer model*

Because AOD optical transmission has a complex dependence on the transducer properties, I constrained my model with experimental measurements. To do this I recorded the optical power transmitted through an individual AOD over a range of incidence angles and drive frequencies.

To constrain the effective transducer width, L, I measured the dependence of diffraction efficiency on relative incidence angle for both narrow and wide transducer AODs, as shown in Fig. 4.1 (see Section 4.1.2 for description). I then inferred L from the separation between the efficiency minima. The values of L that gave the best match to the measured separation in the minima were $L = 1.15$ mm for the narrow transducer and $L = 3.25$ mm for the wide transducer.

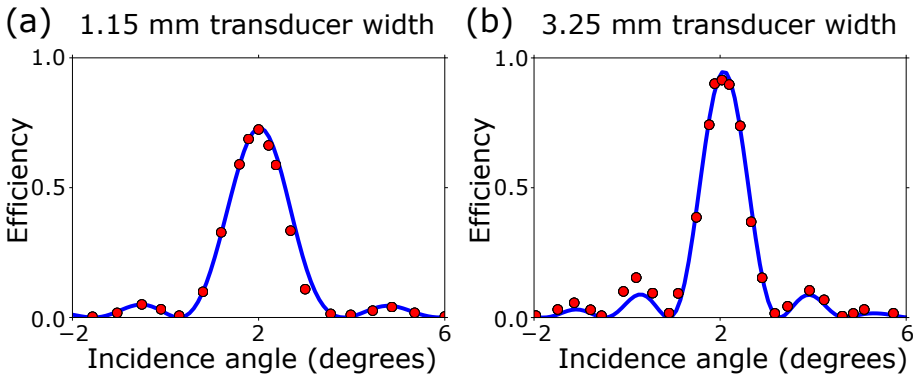

Figure 4.1: Tuning the AOD transducer width parameter in my model by fitting experimentally measured separations between efficiency minima. Model simulations following tuning (solid lines) and experimental measurements (dots) for AOD diffraction efficiency into the -1 mode against incidence angle. Plots are for two different AODs with transducer widths of (a) 1.15 mm and (b) 3.25 mm. Optical wavelength was 785 nm; acoustic frequency 39 MHz; RF drive power 1.5 W. (Published in [1])

I calculated the efficiency with which RF electronic drive signals were converted into acoustic power (RF-acoustic coupling) by the AOD transducers over a range of drive frequencies, by fitting single AOD model predictions to experimentally measured efficiencies at the (frequency dependent) Bragg angle (see Section 4.1.2). Two wavelengths were used (800 nm and 909 nm) in order to check my calculated acoustic power was independent of optical wavelength. Holding the RF power at 1.5 W, I measured the -1 diffraction mode efficiency over a range of drive frequencies (Fig. 4.2 green and blue dots) and determined the acoustic powers that gave the best fit to model predictions (magenta triangles). I divided my inferred acoustic drive powers by the the RF power (1.5 W) to find the RF-acoustic coupling. The RF-acoustic coupling (magenta line) was interpolated between each experimentally measured frequency using a cubic spline and the interpolated coupling was then used in the model to calculate the -1 (blue and green lines) and -2 (red and cyan lines) diffraction efficiencies. This tuning procedure is weakly dependent on the value chosen for α, which determines the diffraction efficiency into the -2 mode (red and cyan lines). I experimentally measured the -2 mode diffraction efficiency (red and cyan dots) and chose the value of α that gave the best fit. Examining simulations over a range of α values, I found $\alpha = 0.5$ gave the closest agreement when weighting the fit to the data from both wavelengths equally. However, if unequal weightings were given to the fitting to the 800 nm or 909 nm data, α could feasibly take a value in the range between 0.4 and 0.6.

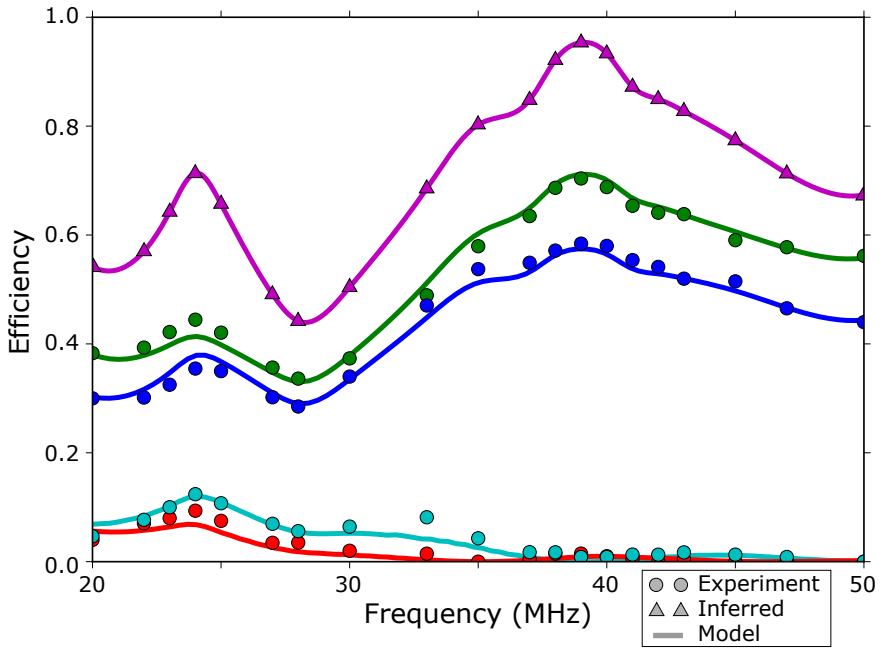

Figure 4.2: Tuning the RF-acoustic coupling and second-order diffraction coefficient, α, in my model for the narrow transducer AODs. The diffraction efficiencies of -1 and -2 modes measured at the -1 mode Bragg angle (adjusted for each frequency) are plotted against drive frequency, for two different wavelengths. The green and blue dots are experimentally measured efficiencies into the -1 mode at 800 nm and 909 nm optical wavelengths respectively. The cyan and red dots are experimentally measured efficiencies into the -2 mode at 800 nm and 909 nm optical wavelengths respectively. The magenta triangles are the conversion efficiency of RF drive signal into acoustic power (RF-acoustic coupling) inferred from the experimental measurements by my model. The magenta line is used by the model to interpolate the RF-acoustic coupling between the magenta triangles. The green, blue, cyan and red lines are the model predictions, using the inferred RF-acoustic coupling, corresponding to the experimentally measured quantities. (Published in [1])

Fig. 4.2 shows the RF-acoustic coupling efficiency data for the narrow transducer AODs. I also measured the properties of the wide transducer AODs and used the same process to infer the RF-acoustic coupling profile. Having found values for L, α and the RF-acoustic coupling for both AOD designs, I had constrained my spherical AOL model. The source code of my model (written in Python 2.7) is available online [4].

4.1.2 *Set-ups for measuring AOD efficiency*

I used two distinct experimental set-ups for measuring AOD diffraction efficiency. The first was for measuring AOD diffraction efficiency

into the -1 mode against optical incidence angle. This setup was used to produce Fig. 4.1. The second was to measure diffraction efficiencies into multiple modes at two different wavelengths (but not incidence angle) and was used to produce Fig. 4.2.

The optical set up used to measure diffraction efficiency and incidence angle (Fig. 4.1) consisted of a near-infrared laser (785 nm) and a green laser (532 nm), which allowed me to simultaneously measure the orientation of an AOD and the power of the diffracted (or non-diffracted) beams—Fig. 4.3(a). A gimbal (Thorlabs GMB1) was used to control and measure angles. Rotating the gimbal by an angle, Θ, deflected the green reflected beam (dashed) by 4Θ and the red beam by 2Θ. When the AOD was rotated by an angle Θ, the green focus on the screen shifted corresponding to the angle 2Θ. The gimbal could then be counter-rotated by $\Theta/2$ to cancel out the 2Θ shift and the angle $\Theta/2$ could be read off the gimbal.

To measure the RF drive power, a power meter (Diamond Antenna SX-200) was used to measure the power transmitted to the AOD's transducer. In all experiments, the RF power was fixed at 1.5 W at all drive frequencies. The angles in Fig. 4.1 were measured relative to one another and the peak was aligned to the Bragg angle from the model. The polariser ensured the input beam to the AOD was circularly polarised (the optimal polarisation for the AODs is near-circular).

Whilst using the experimental set up, I identified AODs of the opposite chirality, which had previously gone unnoticed. The difference was manifested through the Bragg angle of the AODs: for some it was 2^{o} and others it was 1^{o}. The Bragg angles should have uniformly been 2^{o} for the particular circular polarisation of light I was using. I found that by using a half wave plate to reverse the handedness of the polarisation the Bragg angles swapped as I expected. This finding is important for AOL assembly because the optical polarisation needed for efficient diffraction by an AOD depends on its crystal's chirality.

The second setup, used to measure the diffraction efficiency into several modes (Fig. 4.2) at two different wavelengths (800 nm, 909 nm), was a simplification of Fig. 4.3(a) where the beam splitter was removed and the beam passed into the power meter via a spatial filter used to switch between diffraction modes. An unusual feature of this experiment was that I adjusted the incidence angle for each frequency to obtain the maximum diffraction efficiency. This was done to avoid frequency-biasing the efficiency. I used a Chameleon Ultra II (Coherent Inc.) laser for this experiment.

4.2 RESULTS

4.2.1 *Simulations of single AOD efficiency*

I used the numerical ray-based model to calculate how the diffraction efficiency of wide and narrow transducer AODs varied as a function of incidence angle and drive frequency for 920 nm optical wavelength and 1.5 W RF drive power, see Figs. 4.3(b) and (c). The high efficiency region (white band) was less broad for the wide transducer AOD than for the narrow transducer, indicating that there was a smaller acceptance angle (range of incidence angles with high diffraction efficiency), as expected from previous work [61]. It is important to realise that the white region of high efficiency is tracing out the geometry of Fig. 2.8(a) with frequency proportional to length of the green arrows and incidence angle giving the bearing of the 0-order black line.

The simulations for the wide transducer AOD, shown in Fig. 4.3(b), had a high peak efficiency of over 85%. The Bragg angle (the angle corresponding to peak efficiency) increased with drive frequency and the angular range of high efficiency (acceptance angle) was under 1° and nearly constant between 20 and 50 MHz. For an incidence angle of around 2°, the drive frequency is limited to under 50 MHz. Below 28 MHz there is a 50% reduction in efficiency due to poor RF-acoustic coupling. For the narrow transducer AOD, the simulations shown in Fig. 4.3(c) predicted that the acceptance angle was 2° at 39 MHz. However, the peak efficiency (in agreement with Fig. 4.2) was lower than that for the wide transducer AOD, being under 60%. As drive frequency increased, the acceptance angle narrowed and the Bragg angle increased. The broad dip in efficiency at around 28 MHz corresponds to the measured drop in transducer efficiency found experimentally (see Fig. 4.2). This dip could have been mistaken as being due to optical power leaking into the second-order diffraction mode.

On the face of it, the narrower transducer provides high diffraction over a wider area of incidence angle-frequency space at the expense of reduced peak efficiency. This is broadly a good summary of the differences between wide and narrow transducer designs. However, as discussed in Chapter 5, the situation is not quite so simple: it is possible to achieve greater peak diffraction efficiency with the narrow transducer AOD and wider acceptance angles with the wide transducer AOD by using higher acoustic drive powers. Using higher drive power comes with its own practical challenges since AOD can need active cooling [62] and transducers can fail even with low drive power (more than one AOD in the lab has needed repairing).

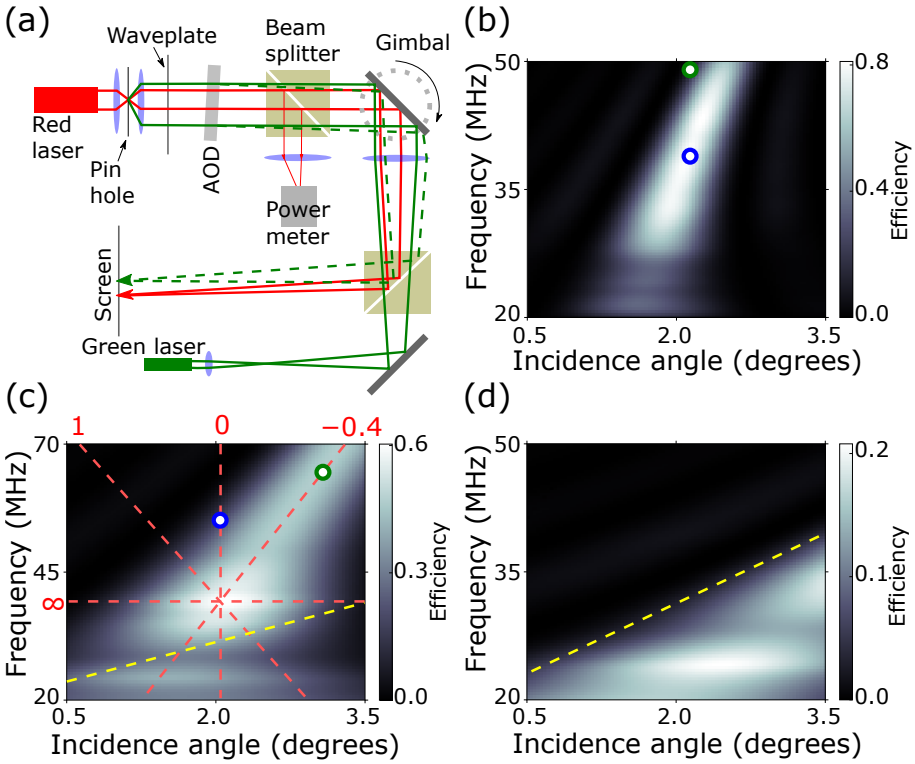

Figure 4.3: Experimental set-up and single AOD simulations. (a) Schematic diagram of the experimental set-up for measuring the incidence angle and efficiency of an AOD, used for data in Fig. 4.1. Optical paths of near-infrared and green laser light shown as solid lines. Reflected green beam shown as dashed line. Components are coloured as follows: beam splitter, yellow; lenses, blue; mirrors, dark grey. (b) Simulated diffraction efficiency of a wide transducer AOD into the -1 mode. (c) Simulated diffraction efficiency of a narrow transducer AOD into the -1 mode. Dashed red lines mark out different $\mathcal{R}$ values if the AOD was used as X- (or Y-) in an AOL. (d) Simulated diffraction efficiency of a narrow transducer AOD into the -2 mode as a fraction of the -1 mode efficiency. Optical wavelength was 920 nm in (b)–(d). The dotted yellow lines in (c) and (d) indicate the AOD's second-order boundary. Blue and green dots on (b) and (c) indicate frequency and incidence angle for X+ and X- in a cylindrical AOL focussed at $\Theta_x = 1^o, z = \infty$ with $\mathcal{R} = 0$ and $\mathcal{R} = -0.4$ respectively. (Published in [1])

4.2.2 *Predictions of cylindrical AOL performance*

Combining my diffraction efficiency simulations for wide and narrow transducer AODs together enabled me to understand why the transmission efficiency of a cylindrical AOL (a pair of anti-parallel AODs) operating in pointing mode depended sensitively on the pair deflection ratio defined in 3.1.4. All the results discussed in this section for

X+ and X- in a cylindrical AOL apply also to both Y+ and Y- in a spherical AOL.

In my simulated design of cylindrical AOL the first AOD (X+) is the wide transducer design and the second (X-) is the narrow, to match the compact AOL designs used for experiments. The red dashed lines labelled by $\mathcal{R}$ value on Fig. 4.3(c) show how incidence angle to and drive frequency of X- vary with lateral focal position Θ_x at $z_{\text{AOL}} = \infty$. $\mathcal{R} = 0$ and $\mathcal{R} = \infty$ correspond to fixed incidence angle and fixed drive frequency, respectively. For $\mathcal{R} = 1$, the line runs perpendicular to the ridge of high efficiency, while the value of -0.4 runs along the ridge, keeping largely within the high efficiency region. The drive frequency of X+ also depends on $\mathcal{R}$ but the angle of incidence to X+ is fixed (at 2.1^{o} for 920 nm optical wavelength).

A simplistic strategy to drive a cylindrical AOL would be to maintain optimal diffraction efficiency on X-. This requires $\mathcal{R} = -0.4$ for the simulated design of AODs. As an example, the green and blue dots in Figs. 4.3(b) and (c) show the points corresponding to the same focal position but with different $\mathcal{R}$ values (blue 0; green -0.4). As can be seen from the figure, $\mathcal{R} = 0$ in this example has greater diffraction efficiency than $\mathcal{R} = -0.4$ due to X+ losing efficiency sharply above 45 MHz (Fig. 4.3(b) green dot). Two points can be drawn from this example. Firstly, for this particular compact AOL I can achieve larger lateral deflections with $\mathcal{R} = 0$ than $\mathcal{R} = -0.4$ whilst maintaining high transmission efficiency. Secondly, it would be beneficial if the efficiency ridge in Fig. 4.3(b) was vertical, which could be achieved by using an acoustically-rotated AOD design.

My model also predicted that second order diffraction into the -2 mode occurs in X- at certain drive frequencies and incidence angles. This effect is unwanted because it produces observable second-order 'ghost' images. A second-order 'ghost' image that appears when the X- drive frequency is F will be identical to the 'proper' image found when the X- drive frequency is $2F$. Consequently, these faint 'ghost' images of objects appear displaced from their correct positions. Figure 4.3(d) shows the relationship between the ratio of the second order to the first order efficiency as a function of the incidence angle and drive frequency. The yellow line marks the AOD's second-order boundary, below which second order diffraction becomes significant. To block second-order 'ghost' images, a quarter-wave plate and linear polariser are needed after the last AOD, which reduces the AOL's optical transmission efficiency in the region of 20%. An alternative would have been to avoid the second-order region of Fig. 4.3(d) by carefully choosing drive frequencies, but this would have restricted the field of view.

4.2.3 *Dependence of spherical AOL efficiency on axial position*

I next examined whether my AOL model could also predict the transmission efficiency when the AOL was used in full-frame pointing mode to focus above or below the front focal plane of the objective. This was to verify the model is accurate for linearly-chirped drive frequencies. Note that the pair deflection ratio is defined for a frequency ramp at $t = 0$ and is unaffected by chirps. Constant frequency offsets were used across the four AODs to image each pixel, which were changed depending on the lateral offset corresponding to the pixel. Thus there is a one-to-one correspondence between frequency ramps and pixels.

Figure 4.4 compares the normalised predicted fluorescence intensity (top row) and experimentally measured fluorescence intensity (bottom row) over the field of view in three different focal planes. I use $\mathcal{R} = 0.3$ here for its high transmission efficiency over a large field of view. The shape of the regions of high transmission efficiency (white areas in Fig. 4.4) in the model and experimental measurements changed only subtly with axial position and were in good agreement. The region of high transmission efficiency expanded in the positive x-direction as z increased in both the model and experiment.

The ratio of fluorescence peaks from left to right in Fig. 4.4 for the model was $0.78 : 1 : 0.86$, and for experiment was $0.55 : 1 : 0.70$. The decrease in intensity as the focus moves away from the objective's front focal plane is likely to arise from two factors. The first is that spherical aberrations are introduced as the focal position shifts axially away from $z_{\text{obj}} = 0$ m so the PSF deteriorates, changing the fluorescence excitation. This effect is present in the experimental measurements but not in the model. The second effect, which is present in both model and experiment, is that AODs are driven with linearly chirped frequencies to shift the axial position. The gradient of the chirp is proportional to the distance from the objective's front focal plane. As the distance increases, the range of frequencies across each of the AODs increases and progressively blurs the region of high transmission efficiency, reducing the peak.

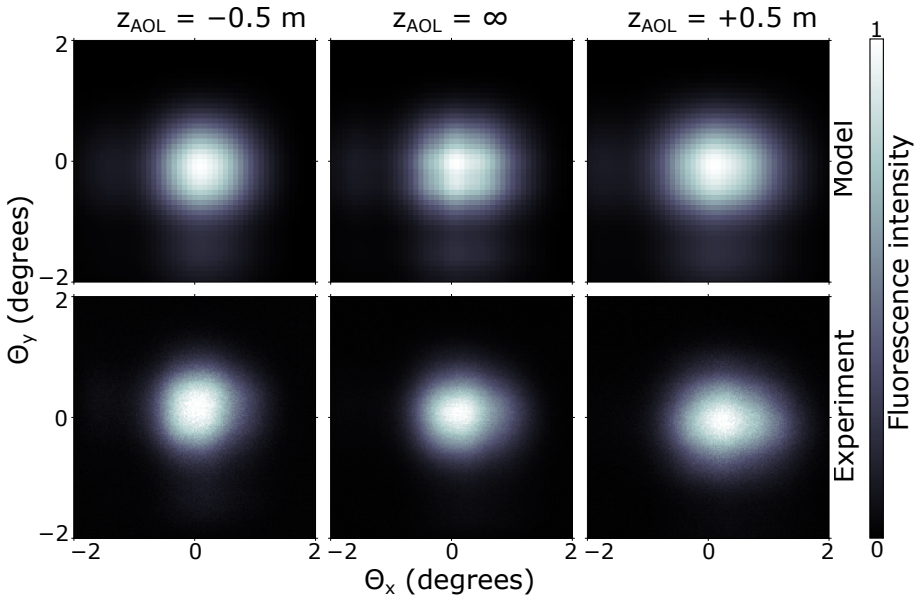

Figure 4.4: Comparison of normalised fluorescence intensity from experiment and simulations for $\mathcal{R} = 0.3$. Three focal planes are shown: $z_{AOL} = -0.5$ m, $z_{AOL} = \infty$, $z_{AOL} = 0.5$ m. The optical wavelength was 920 nm. (Published in [1])

4.2.4 *Dependence of cylindrical AOL efficiency on line-scanning velocity*

I used the numerical ray-based model to examine how the focal-scan-speed affects the field of view of the AOL microscope in full-frame line-scanning mode. Similarly to Section 4.2.3, linearly-chirped drive frequencies were simulated across the AODs, calculated using the drive equations. Each set of four drive ramps across the four AODs produced an entire line-scan, which could be divided up into an arbitrary number of pixels depending on the sampling rate (dwell time). Thus there would be a many-to-one relationship between pixels and frequency ramps, which is different to pointing mode considered in Section 4.2.3. Scan speed is inversely proportional to dwell time.

My simulation results are shown in Fig. 4.5. Setting $z_{AOL} = 1$ m, I found that the field of view decreased as scan-speeds decreased, providing the dwell time was more than about 200 ns. For dwell times under 100 ns, the field of view is stable, but the peak efficiency begins to decrease with dwell time. The explanation for this is the chirps on X+ and X- are very steep and therefore the acoustic frequencies at the edges of those AODs have large deviations from the optimal frequency F_0, leading to weaker diffraction efficiency.

The choice of the focal length as +1 m is arbitrary. However, Fig. 4.5 characterises the microscope over all focal lengths due to the approximate scaling relations when the AOD spacing is small ($s \ll z_{AOL}$). Doubling the ramp gradients b corresponds very nearly to halving the focal length z_{AOL} and halving the dwell time. As an example, the

cyan line of Fig. 4.5 presented as a dwell time of 500 ns at a focal length of +1 m also corresponds (nearly) to a focal length of +0.5 m for a dwell time of 250 ns. The model suggests an optimal range for the *focal length-dwell time* ratio for the compact AOL in the region of 10^7 m/s.

These simulations are in agreement with the experimental finding that only short line-scans are possible away from the front focal plane of the objective ($z_{AOL} = \infty$) when scan speeds are slow. The dwell times used in [61] corresponded to the blue line of Fig. 4.5, and are predicted to be short. In the limit $z_{AOL} = \infty$, by the reasoning of the previous paragraph, this corresponds to a dwell time of zero in Fig. 4.5. As noted for very short dwell times, the efficiency falls off due to the steepness of the frequency ramps used. However, in the limit $z_{AOL} = \infty$ the ramps can have arbitrary dwell time and still correspond to zero dwell time at $z_{AOL} = 1$ m. I would therefore expect the field of view at $z_{AOL} = \infty$ to be very comparable to the yellow line of Fig. 4.5 for all dwell times longer than 100 ns. Thus, full-frame line-scans with large dwell time are possible, as found in [61].

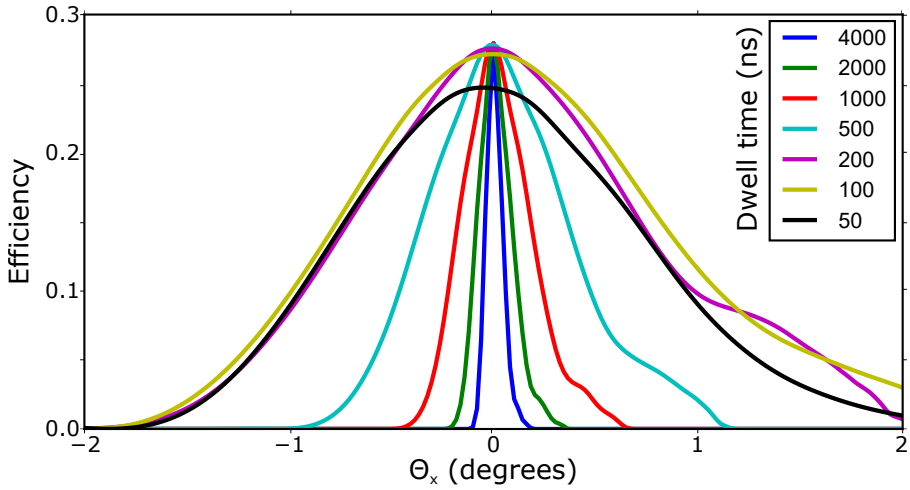

Figure 4.5: Modelling AOL field of view dependence on scan speed. Diffraction efficiency is shown over the field of view for a range of pixel dwell times. Focal length taken to be +1 m, field of view 4° (70 mrad), and 512 pixels in a line. (Under consideration in [2])

4.3 DISCUSSION

I have developed an experimentally-constrained numerical ray-based model of light propagation through a spherical AOL that incorporates refraction and acousto-optic diffraction. Chirped acoustic frequency drives (linear or nonlinear) can be chosen independently for each of the four (or however many) AODs. The close match between AOL model predictions and experimental results from a 3D two-photon AOL microscope confirm that the model reproduces the main

properties of light propagation through the AOL over a wide range of acoustic centre frequencies and linear frequency chirps. By providing a theoretical framework for understanding light propagation through a spherical AOL, my open source modelling provides a tool for improving the design and control of AOL microscope technology.

My ray-based approach builds on classical models of AODs, by generalising the drive frequency to include chirped drives and by combining AODs of different spatial orientations in series to form a spherical AOL. My model was tuned to simulate a compact AOL [61], using AODs which had the optic axis normal to the aperture and the transducer aligned with the slow shear acoustic mode. In my model, the RF-acoustic coupling properties of the wide and narrow transducer AODs were experimentally inferred and I demonstrated that my model was able to correctly account for the wavelength-dependence of diffraction efficiency between 800 nm and 920 nm (Fig. 4.2). The RF-acoustic coupling inferred for the narrow transducer AOD has a similar form (frequency scale reduced) to the theoretical calculation shown in [101] Fig. 7 and is consistent with the transducer having a resonance around 40 MHz, which was specified in the design. Examining the field of view for different $\mathcal{R}$ values was a rigorous test of my model, because each ratio corresponds to a different cross-section through the *frequency-incidence angle* plane for the narrow transducer AOD—red lines in Fig. 4.3(c).

The model confirms the benefits of several of the design features of the current compact AOL design when operating in pointing mode. For example, the diffraction efficiencies of the AODs X- and Y- depend on optical incidence angle (Fig. 4.1). Because the incidence angle of rays into X- and Y- vary with lateral focus deflection and focal length, a large acceptance angle is needed for a large imaging volume and so a narrow transducer AOD design is favourable [61]. In contrast, the incidence angles for X+ and Y+ are both fixed and the main requirement for X+ and Y+ are high peak efficiencies. A wide transducer AOD design requires less RF drive power to achieve high diffraction efficiency, which makes wide transducer designs suitable for the first two AODs in the AOL.

The transmission efficiency of an AOL is not predicted to be significantly affected by whether the design uses 4f relays between the AODs (simulations not shown). In practice, not having polarisers between AODs would boost efficiency though this is predicted to be a uniform effect and I would estimate the peak compact AOL transmission efficiency would increase from 25% to 35%. It would be possible to extend my model to the acoustically-rotated AOD designs used in [62] by accounting for the following differences: large acoustic walk-off angle, thicker crystals (30 mm [62] versus 8 mm for the compact AOL AODs), and higher drive power (20 W [62] versus 1.5 W for the compact AOL AODs). Further to these extensions, experimental mea-

surements for the AODs would be needed to constrain the model. Such AODs may provide greater frequency bandwidth and acceptance angle and therefore improve AOL imaging volume. Also they use linearly polarised light, which is marginally easier to work with. The reason that on-axis AODs (no acoustic or optic rotation) have been used in this thesis is that they are narrower. This makes them well-suited for the compact AOL design, more affordable, and possibly introduce fewer aberrations (though more investigation is needed to confirm this).

Modelling indicates that the *focal length-dwell time* ratio should be considered when performing line-scans with a compact AOL. For ratios below 5×10^6 m/s the field of view is predicted to increase as the ratio increases. The model is consistent with the experimental finding that only short scans are possible for $z_{\text{obj}} \neq 0$ when scan speeds are slow [61] but slow full-frame scans are possible providing $z_{\text{obj}} = 0$. However, for ratios above 10^7 m/s the diffraction efficiency is predicted to decrease across the field of view as the ratio increases, with the size of the field of view remaining steady. Intuitively, scans need to be fast if $z_{\text{obj}} \neq 0$ in order for the linear chirps to be dominated by scanning rather than focusing. In Eq. (2.7), the numerators for the bs are of the form $1 \pm v/V$. The 1 corresponds principally to focusing and the v/V contributes to scanning. Loosely, fast scanning therefore requires $v > V$. Indeed, the 200 ns dwell time in Fig. 4.5 corresponds to $v = 684$ m/s, exceeding the acoustic velocity $V = 613$ m/s. If scans are 'too fast', the ramps become so extreme that only the centre of the ramp efficiently diffracts an incident beam and the aperture is effectively reduced, leading to a reduction in overall diffraction efficiency. A likely further consequence of this is that spatial resolution is degraded, though this needs further investigation.

The important practical implication of the *focal length-dwell time* ratio is that the dwell time should be varied according to focal length if the goal is to maximise diffraction efficiency and have a field of view which does not depend on z_{AOL}. However, if the goal is to have the flattest field of view possible then the briefest dwell time possible should be used. This ratio principally determines whether full-frame line-scanning is possible away from the front focal plane of the microscope objective. Crucially, in order to perform full-frame lateral line-scans centred at arbitrary positions in 3D space, dwell times need to be kept short. Ideally this means 100 ns or less as demonstrated in [2], which requires the development of sophisticated microscope control and acquisition electronics.

Although my ray-based model is able to reproduce the experimental data from a particular AOL, one limitation is that it is unable to calculate the microscope illumination PSFs. The design of AODs I used had the benefit of introducing very little optical aberration into the system. Consequently, the ray-based model was well-suited to the

compact AOL. For modelling an AOL which produces significant optical aberration, it would be necessary to calculate the PSFs in order to accurately predict two-photon excitation fluorescence. To do this, my model could be extended to calculate aberrations geometrically by using its ray-tracing capability. Alternatively the wave optics AOD model of [102] could be extended to a spherical AOL, which would naturally calculate PSFs, but it would be far more complex and would be computationally intensive. A far-simpler model is developed in Chapter 8 which is able to predict the shape of PSFs but not the efficiency; it may be possible to combine this with the ray-based model.

5

AMPLITUDE MODULATION

A key measure of a microscope's performance is how large a sample can be imaged at high spatial resolution. The previously chapter details how drive frequencies were fine-tuned to optimise an AOL microscope's field of view. A second consideration of AOL microscope performance is that optical transmission at the centre of the imaging volume is much higher than at the extremities. In this Chapter, I examine how amplitude modulation of the acoustic drives can extend the microscope's field of view and improve the uniformity of transmission efficiency.

For a clear illustration of how variations in brightness across the field of view can lead to problems, consider Fig. 5.1 which shows complete mice brain slice images constructed by stitching a series of smaller images together. A problem with doing this is that the signal is brightest at the centre of the AOL's field of view and fades out around the edges. Therefore, images that are stitched together show a periodic variation in brightness as shown in Fig. 5.1(a). To reduce the variation in brightness, it was necessary to stitch together very small image tiles as in Fig. 5.1(b) but this is slow. If the brightness was more uniform and the field of view was extended, such large-scale mosaic images could be constructed much more efficiently.

This relatively brief chapter follows naturally on from the previous since it is based on the same AOD model [85] as the ray-based AOL model. In [62] (see supplementary material), amplitude modulation has been reported to very successfully extend the field of view of an AOL microscope operating in pointing mode (Fig. 2.1) as well as making the optical transmission more uniform. However, no exposition has been given in the literature of how amplitude modulation should be applied to enhance AOL performance. I apply standard AOD theory to provide such a description and show high drive powers are required in order to maximally benefit from amplitude modulation. This theoretical finding is apparently consistent with 20 W of drive power per AOD reported in [62]. Furthermore, I have extended AOL microscope amplitude modulation functionality to work for line-scanning as well as pointing, see Figs. 2.1(a) and (c) for line-scanning and Figs. 2.1(b) and (d) for pointing. One advantage of this is that a 400×400 pixel image can be acquired at 80 Hz instead of 0.25 Hz (a factor of 320 faster).

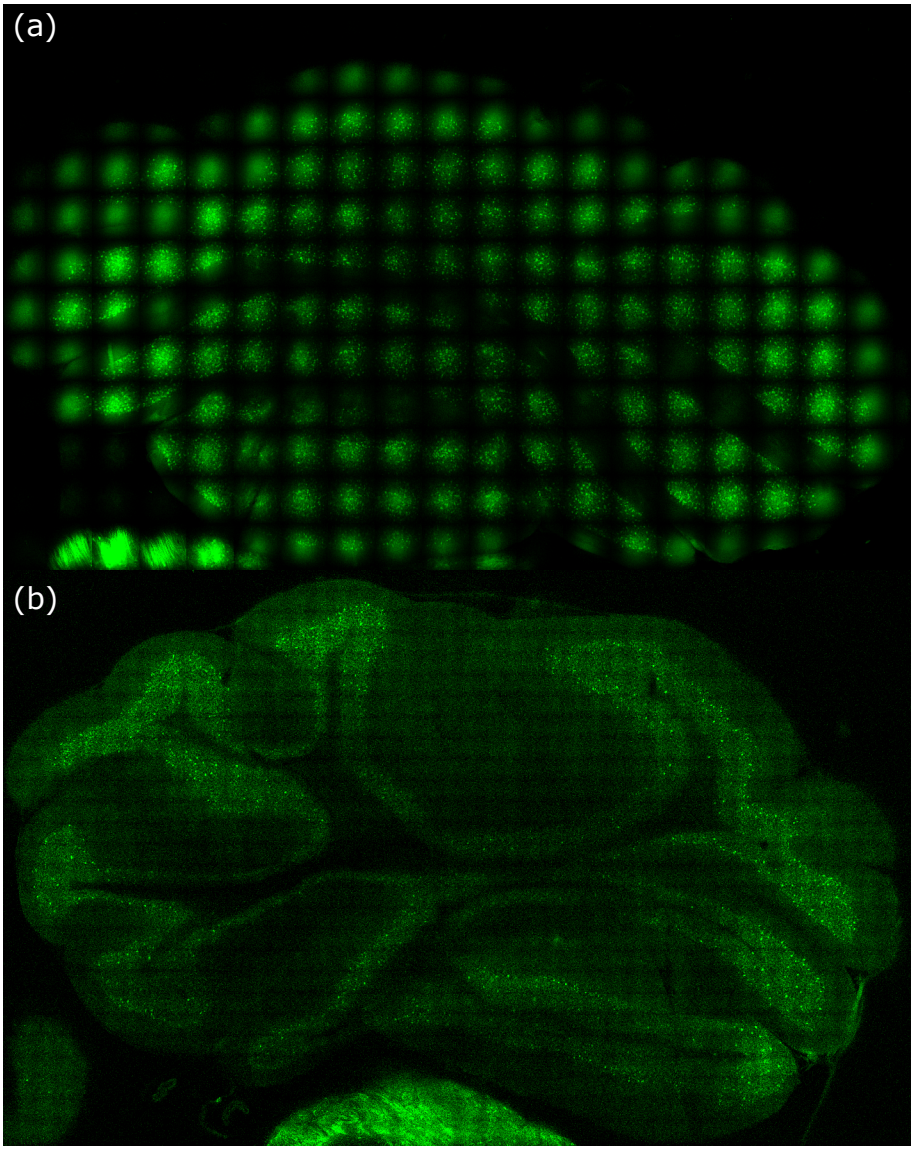

Figure 5.1: Mosaic images of complete mouse brain slices (height 4.5 mm, width 7 mm) constructed by tiling together smaller images (both without amplitude modulation). (a) 350×350 μm tiles. (b) Smaller, 150×150 μm tiles.

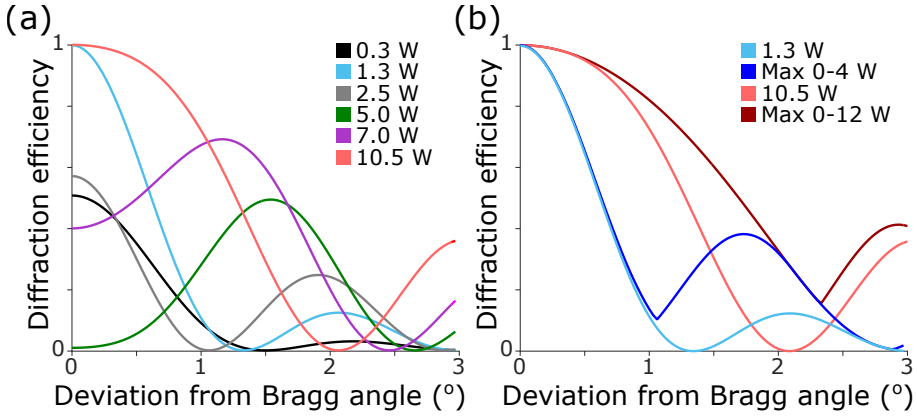

Figure 5.2: Amplitude modulation: model prediction of diffraction efficiency plotted against deviation of optical incidence angle from the Bragg angle for a 3.2 mm on-axis transducer AOD. (a) A range of drive powers (which map to acoustic amplitudes) are shown. (b) Efficiencies for fixed drive powers of 1.3 W and 10.5 W are plotted along with the maximum efficiencies possible using modulated drive powers under 4 W and under 12 W. The greater angular deviation for dark red (blue) compared to light red (blue) show the benefit of dynamically changing the amplitude as opposed to using a fixed amplitude when large (small) drive powers are available.

5.1 THEORY AND IMPLEMENTATION

The diffraction efficiency of an AOD, for a given optical wavelength, depends on incidence angle, drive frequency and drive power. The drive frequency and incidence angle determine the dispersion relation mismatch, which sensitively affects diffraction efficiency. The second difficulty is that the conversion of drive power into acoustic power has a dependence on the drive frequency. Compensating the direct diffraction efficiency dependence on frequency is straightforward because the drive power can simply be increased to counter any drop in conversion efficiency. That amplitude modulation can compensate the efficiency dependence on incidence angle which is indirectly related to frequency in an AOL is much less obvious and I detail the relevant theory below.

On inspection, Eq. (4.1) reveals that amplitude modulation is more effective the larger the amplitude is. In the approximation of large amplitudes relative to wavevector mismatch ($\zeta \ll u$), the equation can be binomially expanded to yield

$$\eta = \left(1 - \frac{\zeta^2}{u^2}\right) \sin^2 \left[u \left(1 + \frac{\zeta^2}{2u^2}\right)\right] \tag{5.1}$$

The terms in round brackets are both approximately equal to 1. Therefore the main contribution is $\sin^2 u$, where u is proportional to the square root of acoustic power and ζ is independent of acoustic power.

In so far as the theory is valid, diffraction efficiency can be maintained at close to 100% whatever the wavevector mismatch providing the acoustic wave amplitude is large enough to make $u \gg \zeta$. I say in so far as the theory is valid because Eq. (4.1) assumed there was no diffraction into higher-order modes. In practice, as drive powers increase the amount of power leaking into higher-order diffraction modes increases so the achievable diffraction efficiency into the -1 mode at the Bragg angle would decrease with drive power. Whilst this is worth bearing in mind, it is a secondary concern.

An examination of Eq. (4.1) shows that the diffraction efficiency has an oscillatory dependence on drive power for a given value of ζ (fixed incidence angle). In Fig. 5.2(a) I have plotted Eq. (4.1) for a range of incidence angles and drive powers. It reveals that a peak in diffraction efficiency at the Bragg angle occurs first at 1.3 W and second at 10.5 W, with the diffraction efficiency at the Bragg angle going to zero around 5 W. There would be further peaks and zeros at the Bragg angle if higher drive powers were included. Note that the maximum in diffraction efficiency for 5 W occurs far from the Bragg angle, about $\pm 1.8^{\circ}$ but is only about 50% efficient. An intuitive picture is that increasing drive power from 1.3 W progressively reduces the angular deviation of the secondary maximum (initially at $\pm 1.8^{\circ}$) and increases its efficiency until the secondary maximum becomes the primary maximum. By the time the drive power reaches 10.5 W, what was the secondary maximum at 1.3 W is now located at the Bragg angle (zero angular deviation) with 100% diffraction efficiency. The AOD transducer width was taken to be wide (3.2 mm). The required drive powers are inversely-proportionally related to transducer width so a transducer half the width would require approximately twice the drive power.

The improvement afforded by amplitude modulation is depicted in Fig. 5.2(b) by the dark blue line for drive powers limited to under 4 W and dark red line for powers up to 12 W. Given that AOL transmission efficiency is given by the product of diffraction efficiencies of four AODs, the secondary maximum of the dark blue line at 1.8° is too low to be of practical use. Thus, low-drive-power amplitude modulation offers no increase in acceptance angle (compare light and dark blue lines). On the other-hand, amplitude modulation at higher drive powers can produce a minor increase in acceptance angle (compare light and dark red lines). However, the acceptance angle was doubled simply by using a greater drive power (compare light red with light blue lines). This is consistent with [62] reporting acoustic drive powers of up to 20 W for their amplitude modulated AOL microscope, for which the AODs required active cooling.

The difference between low and high drive power amplitude modulation is summarised in Fig. 5.3. With high-power amplitude modulation, the dim edges of the field of view are boosted to give uniform

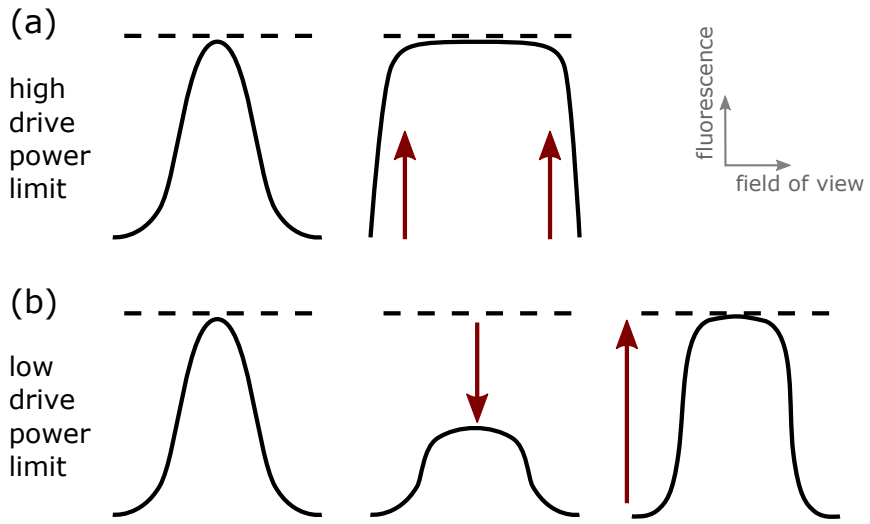

Figure 5.3: Using amplitude modulation to produce a more uniform fluorescence over the field of view. (a) When high drive powers are available, the fluorescence can be boosted in the weak extremities by using large amplitude acoustic waves. (b) If only low drive powers are available, the uniformity can be improved by reducing acoustic amplitudes used in the centre of the field of view. The overall fluorescence can then be increased by boosting input laser power.

fluorescence. The higher the cutoff, the better the results achievable using amplitude modulation. With low-power amplitude modulation the bright centre is reduced, and the entire signal must be boosted by increasing laser power. If low acoustic drive powers are used, such as are used in the compact AOL (< 4 W), amplitude modulation is really only capable of reducing the brightness at the centre of the field of view as opposed to the more desirable function of increasing the brightness around the edges. The AOD I have used are limited to drive powers of 4 W maximum to avoid any risk of damaging the AODs. In light of this, amplitude modulation is primarily useful for flattening the fluorescent brightness over the field of view. In order to have uniform brightness over the entire field of view the centre was significantly dimmed.

I used the numerical ray-based model to calculate how the acoustic amplitude needed to vary to produce an image of uniform brightness. The modelling indicated that a parabolic dependence of amplitude on frequency was sufficient to achieve uniform field illumination. For this purpose, Dr. G. Konstantinou extended the existing FPGA-based RF drive synthesiser to modulate the amplitude parabolically with time. Each of the four AODs had three amplitude coefficients (a total of twelve), which were tuned experimentally.

5.2 RESULTS

I show fluorescence over a 350 μm by 350 μm area with improved uniformity can be achieved by applying parabolic amplitude modulation to the acoustic drive signals. Further, I find that the fluorescence of small-scale structures around the edges of the field of view is limited by aberrations.

I imaged a uniform fluorescence preparation both with and without amplitude modulation (top of Fig 5.4). For fair comparison of the field of view sizes, I set the laser power in each case such that 10% of pixels were 90% saturated. I superposed the two images (amplitude modulation in green, without amplitude modulation in magenta) for visual comparison and found that amplitude modulation produced 62% increase in fluorescence (pixel values normalised to the brightest in the image, total fluorescence taken as sum of pixel values). Note some unwanted second-order diffracted beam has leaked into the top of the images due to using a larger than normal field of view. This is not a limitation of the system and could be removed by realigning the one of the apertures.

I repeated the same procedure with a suspension of fluorescent 1 and 5 μm beads (bottom of Fig 5.4). The field of views were consistent with those for the uniform fluorescence preparation. However, aberrations were very clearly visible around the edges of the field of view. I expect these were chromatic aberrations (for example see blue line in Fig. 8.3 for the size of chromatic effects). Amplitude modulation was having to overcompensate the reduction in fluorescence due to the poor PSF around the edges and therefore it is likely that a more uniform and extensive field of view could be achieved if the chromatic aberration was corrected.

5.3 DISCUSSION

I have found that a uniform fluorescent sample can be imaged with near-uniform brightness over a 350 μm field of view (36 mrad with a 20$\times$ objective, 0.7 numerical aperture). This is within a factor of two of commercially available galvo-based microscopes [75, 76]. The use of amplitude modulation lead to a 62% increase in total fluorescence measured over the field of view. However, the PSF of the microscope deteriorates towards the edges of the field of view and therefore an image of micron-diameter fluorescent beads is far less uniform. This could be improved by correcting for chromatic aberration, a known issue with demonstrated and patented solutions [107, 108].

A benefit of having intrinsically uniform image brightness is that there is no need for post-processing to bring out information hidden around the edges. A concern with post-processing is that it can introduce artifacts and therefore it is preferable to minimise its use.

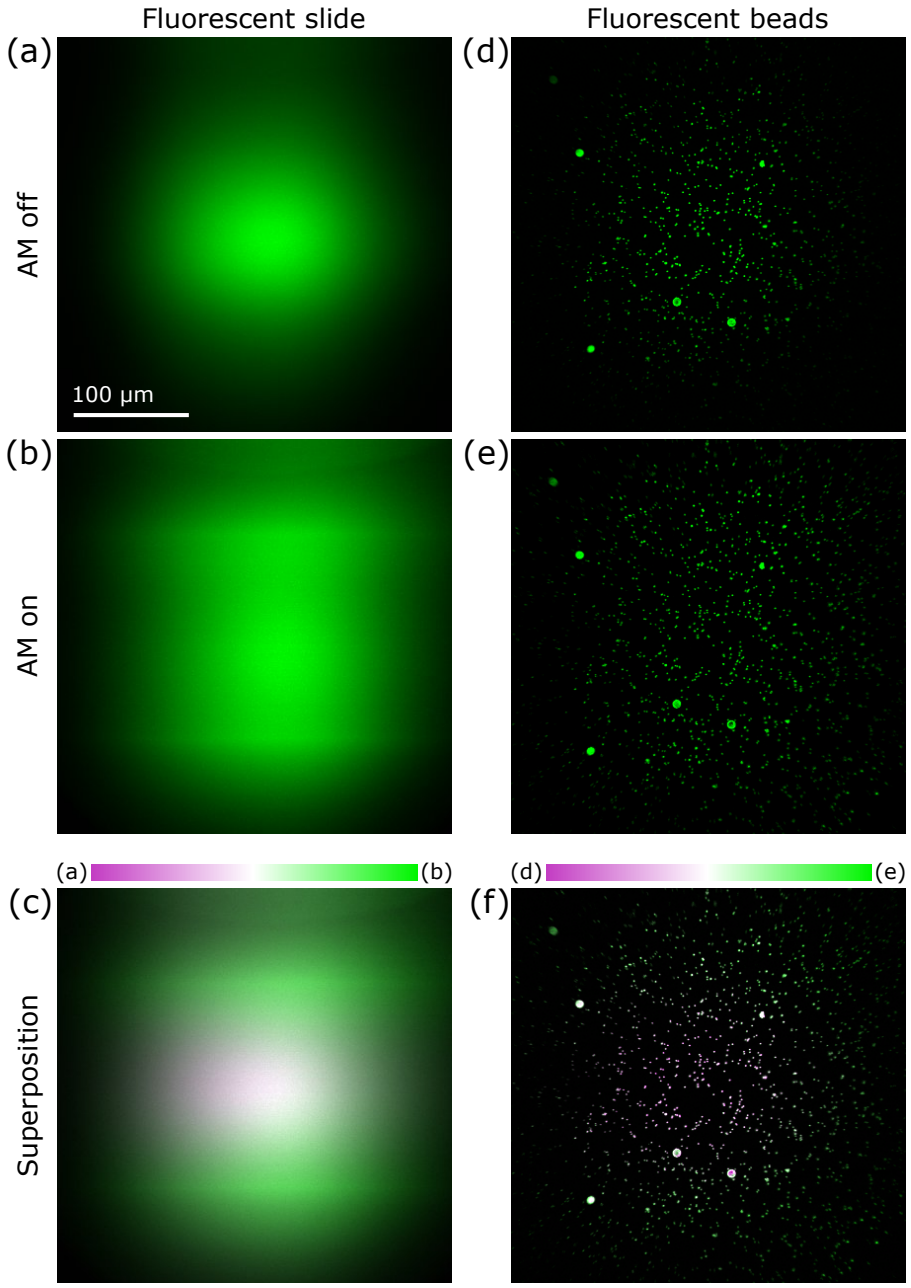

Figure 5.4: Experimental effect of amplitude modulation on fluorescence uniformity and field of view for full-frame line-scanning mode. (a)–(c) Imaging a uniformly fluorescent sample. (d)–(f) Imaging a suspension of 1 and 5 μm beads. (a) and (d) are with amplitude modulation (AM) off; (b) and (e) with amplitude modulation on. (c) and (f) are superimposed plots of (a),(b) and (d),(e) respectively as indicated by the colour-bars above them. (c) and (f) highlight differences in fluorescence with amplitude modulation on (green) and amplitude modulation off (magenta). Note that equal contributions of magenta and green produce white regions.

The signal-to-noise ratio can be so poor around the edges of the field of view that post-processing is unable to recover the desired signal anyway. If images are sufficiently uniform, neighbouring regions can be joined together to produce large-scale mosaic images. This is useful for understanding the anatomy of an entire mouse brain slice before imaging a specific region. In the cases that fluorescence has been achieved by viral injection, large-scale imaging can be used to assess how far the virus has spread and identify regions of most interest. Amplitude modulation produces a uniform brightness across a wider area and so the size of the tiles being stitched together could potentially be increased. However, the fluorescent signal from biological samples I have experimented on was too weak to demonstrate any benefits from amplitude modulation. A more favourable signal to noise ratio could be achieved by either using a more powerful laser (currently 2 W) or enabling acoustic drive powers of over 10 W.

A second benefit of uniform image brightness is that it avoids having a bright-central region overload the PMTs if the signal is too strong. This means that the signal from the extremities of the field of view cannot simply be increased by boosting the laser power, since the central brightness will overload the PMTs. This is further complicated by the use of calcium indicators because fluorescence levels will fluctuate over a large range depending on activity. In the experimental results, amplitude modulation reduced the transmission efficiency of the AOL by 75% because I used low acoustic drive powers (< 4 W). In the case of very bright samples, such as beads and the uniform fluorescent strip, sufficient output laser power could still be achieved by maximising the input laser power. However, I found the utility of amplitude modulation was limited when imaging biological samples due to the weakness of the fluorescent signal, as discussed in the previous paragraph.

It has been claimed that the most effective way to achieve a large acceptance angle (and thus field of view) with an AOL is to use narrow transducer AODs for X- and Y- because acceptance angle is proportional to transducer width [61]. Amplitude modulation provides an alternative means to increase acceptance angle and so it is worth asking if it would be beneficial to replace the narrow transducer AODs with wide transducer AODs driven with high acoustic power. I expect it would not be of benefit, given the very large acoustic drive powers that would be needed: for example, I have found that increasing acoustic drive power by a factor of eight to go from the first to the second diffraction efficiency maximum only doubled the acceptance angle. This modelling therefore supports the claim that decreasing transducer width is most effective for increasing acceptance angle. However, amplitude modulation does offer to further increase acceptance angle if practical limits on transducer width are reached. In practice then, acceptance angle is optimised by finding the best trade-

off between minimising the transducer width and maximising the possible drive power, with emphasis on the transducer width.

To make systematic progress on developing amplitude modulation and have more a detailed model, it would be sensible to examine a single AOD, measuring the efficiency-amplitude dependence over a range of incidence angles and drive frequencies, comparing it to the ray-based model. This would provide sufficient information to determine how far amplitude modulation can go and whether it is worth upgrading the existing AOLs to use higher drive powers given the AOD transducer widths.

6

NONLINEAR DRIVE THEORY AND MODELLING

Nonlinearly-chirped drive frequencies have been proposed to enable arbitrary-direction straight-line-scanning and curved-scanning using a spherical AOL [3, 65, 72], as discussed in Section 2.4. This is in contrast to linearly-chirped drive frequencies which enable line-scanning in only lateral directions (axial position must be constant during scan) and pointing in 3D space. Nonlinear drives are also predicted to enable spherical aberration correction for a new design of AOL using six AODs. However, this is not possible with a conventional AOL (four AODs) and so the issue of spherical aberration correction is deferred until Chapter 8. The present Chapter deals with the theory of nonlinear drives for performing line-scanning and curved-scanning using a conventional AOL (four AODs), and the following Chapter presents AOL microscope images acquired experimentally using nonlinear drives.

By assuming zero separation between the AODs in an AOL, the physical effect of the drive coefficients $a, b, c, d, \ldots$ in Eq. (2.10) are well-defined and straightforward to determine. An AOD's drive frequency is equal to the time-derivatives of the acoustic phase across the AOD as given by Eq. (2.9). For a cylindrical AOL, the acoustic phases across the two AODs $\Phi_+(t - x/V)$ and $\Phi_-(t + x/V)$ can be expressed as Taylor series, where the Taylor coefficient $\Phi_\pm^{(n)}$ denotes the n^{th} time-derivative of the acoustic phase across the $\pm$-oriented AOD evaluated at $t = x = 0$:

$$\Phi_\pm(t \mp \frac{x}{V}) = \sum_{n=1}^{N} \frac{1}{n!} \Phi_\pm^{(n)} \left(t \mp \frac{x}{V}\right)^n \tag{6.1}$$

Assuming zero-spacing between AODs and taking the AOD apertures to be centred at $x = 0$, the Taylor coefficients can be directly related to an effect on the optical wavefront leaving the AOL and its physical interpretation. To do this, Eq. (2.8) is applied twice to arrive at an expression for the optical phase ϕ:

$$\phi = \omega t - \frac{2\pi}{\lambda} z \pm \Phi_+(t - \frac{x}{V}) \pm \Phi_-(t + \frac{x}{V}) \tag{6.2}$$

The incident optic wave is assumed to be planar with angular frequency ω and wavelength λ, while the $\pm$ signs are decided by whether the AODs diffract into the $+1$ or -1 mode. To determine the form of an optical wavefront, it is necessary to consider $\phi =$ constant and make z the subject. Once the wavefront expression is determined, any terms independent of x can be discarded as global phase shifts.

There are some aspects of this phase-based calculation which require closer scrutiny. Technically, Eq. (2.8) applied to the optical phase inside an AOD crystal. To apply it to the optical phase outside the crystal, the condition of continuous phase across the air-crystal boundary can be applied. Providing the acoustic phase shifts are parallel to the apertures as shown in Fig. 3.1, this leads to Eq. (6.2). However, the expression for the optic phase ϕ is generally not even an approximate solution to the scalar wave equation (see Eq. (3.7) of [109]), except when the acoustic phases are linear. To extract sensible results from the phase, it must be converted to a wavefront assumed to be located just after the AOD and then treated using geometric optics. To see Eq. (6.2) cannot in general be a valid representation of an optical wave, note that the wavefront is invariant under changes of z. Despite this conceptual issue, predictions that follow from this approach have been experimentally verified [3]. Indeed, inconsistencies in optics are not unprecedented and do not necessarily affect the utility of a theory (the boundary conditions used in the Fresnel-Kirchhoff diffraction theory [109], for example). In Section 6.1, I use rays to derive a more refined theory that relies only on Eq. (2.1), making the derivation cleaner but also more complex. Importantly, the results that follow from Eq. (2.1) when the AOD spacing is zero are consistent with those arrived at using Eq. (6.2).

The simplicity and demonstrated validity of the results that follow from of Eq. (6.2) make them very worth examining. The results are summarised in Table 6.1, adapted from [3] (I calculated the expressions in the publication but the interpretations had been realised before I began my PhD). For a spherical AOL, the results can be applied independently to the two constituent cylindrical AOLs aligned in the x and y-directions. Furthermore, the physical effects of the Taylor coefficient combinations shown in Table 6.1 are linearly independent so arbitrary-direction line-scans can be constructed by combining lateral and axial scans and positioned in 3D space by adding lateral and axial shifts. Once acoustic phases have been determined, they can be related to the acoustic drive frequencies using Eq. (2.9). However, this implicitly assumes that the transducers are located at $x = 0$. To account for the proper positions of the transducers, drive frequencies must be translated as described in Section 3.1.4.

Table 6.1: Summary of theoretical results for a cylindrical AOL with zero inter-AOD spacing and operating in the +1 diffraction mode. Acoustic phase Taylor coefficients specified in upper case letters translate to the drive frequency coefficients used throughout the thesis in lower case. (Adapted from [3])

n	$\Phi_+^{(n)}$	$\Phi_-^{(n)}$	Optical wavefront out	Physical interpretation
1	A	A	$z = \text{constant}$	no net effect
1	A	$-A$	$z = \frac{-\lambda A}{\pi V} x$	lateral shift: $\frac{\lambda A}{\pi V}$ rad
2	B	B	$z = \frac{\lambda B}{2\pi V^2} x^2$	axial shift: $\frac{\lambda B}{\pi V^2}$ dioptres
2	B	$-B$	$z = \frac{-\lambda B}{\pi V} tx$	lateral velocity: $\frac{\lambda B}{\pi V}$ rad/s
3	C	C	$z = \frac{\lambda C}{2\pi V^2} tx^2$	axial velocity: $\frac{\lambda C}{\pi V^2}$ dioptres/s
3	C	$-C$	$z = \frac{-\lambda C}{2\pi V} t^2 x + \frac{-\lambda C}{6\pi V^3} x^3$	lateral acceleration + coma-like aberration
4	D	D	$z = \frac{\lambda D}{4\pi V^2} t^2 x^2 + \frac{\lambda D}{24\pi V^4} x^4$	axial acceleration + spherical-like aberration

To summarise, the use of nonlinearly-chirped drive frequencies has been solved for AOLs in which the AOD spacing is made zero by use of 4f optical systems or if the cumulative AOD spacing is much smaller than the focal length of the optical beam. However, the key limitation is that the AOD spacing in a compact AOL can be the same magnitude as the focal length: three intervals of 5 cm AOD spacing gives 15 cm cumulatively compared with focal lengths routinely down to 50 cm. In this Chapter, I develop new geometric optics theory to remove this limitation by accounting for the evolution of the optical beam as it propagates over the spaces between AODs. I first establish a general theory for propagating aberrations between planar surfaces normal to the optic axis. I then apply the theory to determining nonlinearly-chirped AOL drive frequencies, which are expressed as power series. Because practical application requires truncation of the power series, I use a wave-based model to explore the effect of neglecting higher-order terms in the series and comparing the results with the zero-spacing approximation.

6.1 ANALYTIC LOCAL EVOLUTION OF RAY-PROFILES

Modelling the propagation of aberrations is an area of active research. The theoretical basis of this Chapter originates from [110] which de-

rives the equations that govern the evolution of Taylor expansion coefficients of a geometric wavefront. The benefit of such an approach over numerical wavefront propagation is that analytic equations can be manipulated algebraically, are differentiable and are fast to compute. The approach to propagating wavefronts in [110] was to express the wavefront as a Taylor series and then determine how the Taylor coefficients evolve as the wavefront propagates through space. An assumption of their approach was that the wavefront was normal to the optic axis at the Taylor expansion point and therefore the results cannot be applied to an AOD. However, by adapting their derivation, I formulate a theory with no such assumption, describing propagation between planar surfaces instead of surfaces defined by wavefronts. I then show this theory can be readily applied to AODs driven with nonlinear frequency chirps.

The extensive formalism drawn on in [110] masks the simplicity of the underlying mathematics: the derivation essentially involves repeated application of the chain rule to their Eq. (11). I now set up the derivation for propagating between planes (lines mathematically since the derivation is 2D) rather than wavefronts. Let $m(x,z)$ be the slope of a ray passing through the point (x,z):

$$m(x,z) = \frac{\Delta x}{\Delta z} \tag{6.3}$$

The goal is to determine how the Taylor coefficients that describe $m(x,z)$ evolve as the bundle of rays propagate between z_1 and z_2. A straight line with slope $m(x_1,z_1)$ passing through (x_1,z_1) will pass through (x_2,z_2) where $x_2 - x_1 = (z_2 - z_1)m(x_1,z_1)$. Given that (x_1,z_1) and (x_2,z_2) both lie on the same straight line it follows that

$$m(x_1,z_1) = m(x_2,z_2) \tag{6.4}$$

The zero-order Taylor coefficients are equal if the Taylor expansion points are taken to be (x_0,z_1) and $(x_0 + (z_2 - z_1)m(x_0,z_1),z_2)$, for arbitrary x_0. For this reason, I impose this relation on the Taylor expansion points and thus write their expansions as

$$\begin{aligned} m(x,z_1) &= \sum_n \frac{1}{n!} m_1^{(n)} (x - x_0)^n \\ m(x,z_2) &= \sum_n \frac{1}{n!} m_2^{(n)} (x - x_0 - (z_2 - z_1)m(x_0,z_1))^n \end{aligned} \tag{6.5}$$

Taking the derivative of Eq. (6.4) with respect to x_2 and applying the chain rule:

$$\begin{aligned} \frac{\partial m(x_2,z_2)}{\partial x_2} &= \frac{\partial m(x_1,z_1)}{\partial x_1} \Big/ \frac{\mathrm{d}x_2(x_1)}{\mathrm{d}x_1} \\ &= \frac{\partial m(x_1,z_1)}{\partial x_1} \Big/ \left[1 + (z_2 - z_1)\frac{\partial m(x_1,z_1)}{\partial x_1}\right] \end{aligned} \tag{6.6}$$

This expression determines the first-order Taylor coefficient. Repeated application of the chain rule to Eq. (6.6) yields expressions for all subsequent Taylor coefficients in Eq. (6.5):

$$\begin{aligned} m_2^{(0)} &= m_1^{(0)} \\ m_2^{(1)} &= m_1^{(1)} \Big/ \left(1 + [z_2 - z_1]\, m_2^{(1)}\right) \\ &\vdots \end{aligned} \tag{6.7}$$

To make a closer analogy to the results of [110], I work with ray-profiles $\Gamma(x)$, which I define as the negative integral of the ray gradients along lines satisfying $z =$ constant. Ray-profiles $\Gamma_1(x)$ and $\Gamma_2(x)$ along the lines $z = z_1$ and $z = z_2$ respectively are thus related to the ray slopes by their derivatives:

$$\frac{\mathrm{d}\Gamma_1(x_1)}{\mathrm{d}x_1} = -m(x_1, z_1), \quad \frac{\mathrm{d}\Gamma_2(x_2)}{\mathrm{d}x_2} = -m(x_2, z_2) \tag{6.8}$$

Rewriting and continuing Eq. (6.7) in terms of ray-profiles where $\Gamma_i^{(n)}$ denotes the n^{th} derivative of $\Gamma_i(x)$ evaluated at $x = x_0$ for $i = 1$ and $x = x_0 - (z_2 - z_1)\Gamma_1^{(1)}(x_0)$ for $i = 2$ yields the following:

$$\begin{aligned} \Gamma_2^{(1)} &= \Gamma_1^{(1)} \\ \Gamma_2^{(2)} &= \gamma \Gamma_1^{(2)} \\ \Gamma_2^{(3)} &= \gamma^3 \Gamma_1^{(3)} \\ \Gamma_2^{(4)} &= \gamma^4 (\Gamma_1^{(4)} + 3\tau\gamma\Gamma_1^{(3)2}) \\ \Gamma_2^{(5)} &= \gamma^5 \left[\Gamma_1^{(5)} + 5\gamma\tau\Gamma_1^{(3)} \left(2\Gamma_1^{(4)} + 3\gamma\tau\Gamma_1^{(3)^2}\right)\right] \\ \gamma &= \left(1 - \tau\Gamma_1^{(2)}\right)^{-1} \\ \tau &= z_2 - z_1 \end{aligned} \tag{6.9}$$

To summarise, the evolution of a ray-profile after propagating over an optical path length τ can be calculated from the Taylor coefficient relations above. More compactly, I write the relation between the ray-profile Γ_1 and the propagated ray-profile Γ_2 in terms of the propagation operator $\mathcal{P}_\tau$, where the propagator acts by transforming each Taylor coefficient as given by Eq. (6.9):

$$\Gamma_2 = \mathcal{P}_\tau[\Gamma_1] \tag{6.10}$$

The Taylor coefficient relations for ray-profiles in Eq. (6.9) can be compared to those for wavefronts as derived in [110] to emphasize the similarity between ray-profiles and wavefronts:

$$
\begin{aligned}
w_2^{(2)} &= \beta w_1^{(2)} \\
w_2^{(3)} &= \beta^3 w_1^{(3)} \\
w_2^{(4)} &= \beta^4 \left[w_1^{(4)} + 3\tau \left(\beta w_1^{(3)^2} - w_1^{(2)^4} \right) \right] \\
w_2^{(5)} &= \beta^5 \left[w_1^{(5)} + 5\beta\tau w_1^{(3)} \left(2w_1^{(4)} + 3\beta\tau w_1^{(3)^2} - 6w_1^{(2)^3} \right) \right] \\
\beta &= \left(1 - \tau w_1^{(2)} \right)^{-1}
\end{aligned}
\tag{6.11}
$$

The up to third-order, the results are the same for ray-profiles as for wavefronts. This should not come as a great surprise because in the case that deflection angles are small (paraxial approximation), there should be no material difference between the two approaches because the wavefronts will be nearly flat. Above third-order, the results are simpler for ray-profiles than wavefronts: the only difference is the absence of the last term in the brackets on the right-hand side. Intuition for why the term is missing can be gained by realising that spherical wavefronts correspond to parabolic ray-profiles.

The equations for wavefronts in [110] apply only in the special case when the central ray about which the Taylor expansion is performed is parallel to the optic axis: $w_1^{(1)} = w_2^{(1)} = 0$. By changing from wavefronts to ray-profiles, I have removed this constraint and gained the additional relation $\Gamma_2^{(1)} = \Gamma_1^{(1)}$ for which there is no analogous result in [110]. This is essential in order for the theory to be applicable to AODs.

6.2 APPLICATION TO AN AOL

The ray-profile theory can be readily applied to an AOL. Recall that rays are deflected by $\pm\lambda F/V$ in accordance with Eq. (2.1). This implies that ray-profiles are shifted by the spatial integral of $\lambda F/V$, which is proportional to the acoustic phase. I represent the AOD ray-profile shifts as Taylor series and calculate the required coefficients to produce a focus with a particular trajectory. The final ingredient is that each ray-profile shift Taylor coefficient is proportional to a single acoustic frequency power series coefficient, making it easy to convert the ray-profile shifts into usable drive frequency ramps.

The local ray-profile propagation theory is very manageable in 2D but becomes considerably more cumbersome in 3D. Thus, it is a great advantage that a spherical compact AOL can be viewed as two cylindrical AOLs (see Section 2.2). The nonlinear drives can be derived in 2D and trivially extended to 3D due to the orthogonality of the cylindrical AOLs that comprise a spherical AOL.

The application of the ray-profile theory to a cylindrical AOL is illustrated in Fig. 6.1. The points chosen for the ray-profile propagation coincide with where the base ray intersects the two AODs at

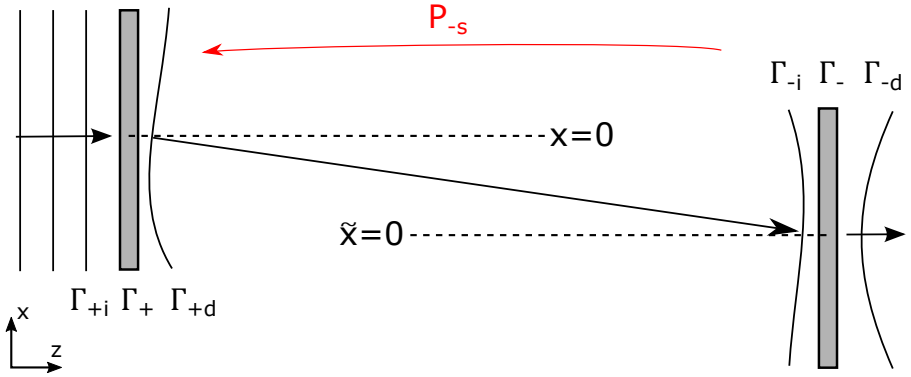

Figure 6.1: Ray-profile calculation in a cylindrical AOL. AODs shown in grey and ray-profiles (Γ) shown as solid lines. Dotted lines $x = 0$ and $\tilde{x} = 0$ shown for illustration. Calculation of Γ_{+d} from Γ_{-i} using the propagator $\mathcal{P}_{-s}$ shown in red and defined by Eq. (6.10). The ray-profiles should not be confused with wavefronts. Rather, the profiles are defined along lines parallel to the AOD and the reader should visualise the ray-profile curves as coming out of the page on a third axis.

$t = 0$ (Section 3.1.3), and move laterally with the first AOD's acoustic wave. At the first AOD, the base ray is taken to be incident at $x = 0$, which in practice should roughly correspond to the centre of the first AOD. Let $\Gamma_{\pm i}$ and $\Gamma_{\pm d}$ respectively denote the incident and diffracted ray-profiles for the first and second AODs, where the $\pm$ indicates the direction of their respective acoustic waves. These two ray-profiles are related by a profile shift $\Gamma_{\pm}$ produced by the acoustic wave across the AOD. The input beam to the first AOD is taken to have a planar ray-profile $\Gamma_{+i} = 0$ so the ray-profiles leaving the first AOD is simply the pattern imposed on it by the acoustic wave: $\Gamma_{+d}(x - Vt) = \Gamma_{+}(x - Vt)$. The ray-profile leaving the first AOD $\Gamma_{+d}(x - Vt)$ is related to the ray-profile entering the second AOD $\Gamma_{-i}(x - Vt)$ by back-propagation:

$$\begin{aligned} \Gamma_{+d}(x - Vt) &= \mathcal{P}_{-s}[\Gamma_{-i}(\tilde{x} - Vt)] \\ \tilde{x} &= x + \psi s \Gamma^{(1)}_{-i} \end{aligned} \tag{6.12}$$

where s is the distance between the AODs and $\psi = \pm 1$ is the AOD diffraction mode, introduced to avoid proliferation of $\pm$ signs. The variable $\tilde{x}$ is needed due to the lateral displacement of the base ray between the two AODs and is used for the ray-profile Taylor expansion on the second AOD. Note the expansion point $(x - Vt)$ moves with the first AOD's acoustic wave because $x = 0$ corresponds to the centre of the first AOD. Furthermore, the position of $\tilde{x} = 0$ relative to the AOL depends on first AOD's drive frequencies through the value of $\Gamma^{(1)}_{-i}$. Finally, a minus sign is needed in $\mathcal{P}_{-s}$ because it represents back-propagation (going backwards in time). Putting this

together provides a way to recover the profile shift of the first AOD from the ray-profile incident to the second AOD:

$$\Gamma_+(x - Vt) = \mathcal{P}_{-s}[\Gamma_{-i}(\tilde{x} - Vt)] \tag{6.13}$$

For the cylindrical AOL to focus the wave at $(x_{\mathrm{AOL}}(t), z_{\mathrm{AOL}}(t))$ relative to the centre of the second AOD ($x = \psi s\theta_0$) at time t, the ray-profile leaving the second AOD needs to be parabolic:

$$\begin{aligned} \Gamma_{-d}(t, \tilde{x}) &= \frac{(x - \psi s\theta_0 - x_{\mathrm{AOL}}(t))^2}{2z_{\mathrm{AOL}}(t)} \\ &= \frac{\left(\tilde{x} - s\left[\Gamma_{-i}^{(1)} + \psi\theta_0\right] - x_{\mathrm{AOL}}(t)\right)^2}{2z_{\mathrm{AOL}}(t)} \end{aligned} \tag{6.14}$$

where θ_0 is the optimal deflection angle as described in Section 3.1.4 and depends on the AOD diffraction mode. Finally, the diffracted ray-profile of the second AOD can be equated to the incident ray-profile and its associated profile shift:

$$\Gamma_{-d}(t, \tilde{x}) = \Gamma_{-i}(\tilde{x} - Vt) + \Gamma_-(\tilde{x} + Vt) \tag{6.15}$$

Crucially, when both sides of Eq. (6.15) are Taylor expanded in powers of $\tilde{x}$, the different signs in the arguments of the functions on the right-hand side enable the equating of coefficients without ambiguity. The application of these equations is algorithmic: I begin by specifying the ray-profile leaving the cylindrical AOL needs to be in order to produce the desired focal trajectory. I then Taylor expand Eq. (6.15) and equate coefficients to determine Γ_- and Γ_{-i}, and from the latter I recover Γ_+ using Eq. (6.13). Applying this method yields the Taylor coefficients for $\Gamma_+(x - Vt)$ and $\Gamma_-(\tilde{x} + Vt)$ expanded at 0. These can be converted to a frequency power series in time that is used to drive the AOD transducers as shown in Eq. (2.10). If the AODs are operating in the $\psi = \pm 1$ diffraction mode, the coefficients for the ray-profile and frequencies are directly proportional:

$$\begin{aligned} a_\pm &= \mp\frac{\psi V^1}{\lambda\, 0!}\Gamma_\pm^{(1)}, & b_\pm &= \frac{\psi V^2}{\lambda\, 1!}\Gamma_\pm^{(2)} \\ c_\pm &= \mp\frac{\psi V^3}{\lambda\, 2!}\Gamma_\pm^{(3)}, & d_\pm &= \frac{\psi V^4}{\lambda\, 3!}\Gamma_\pm^{(4)} \end{aligned} \tag{6.16}$$

where the sign differences for $a_\pm$ and $c_\pm$ are due to the acoustic waves propagating in opposite directions. Importantly, the derivation assumes the transducers of the AODs are located at $x = 0$. The frequency power series must be shifted to the actual transducer positions, using the relation between time and space for the acoustic waves, as described in Section 3.1.4.

6.3 THEORETICAL RESULTS

To recapitulate, the method I use to derive nonlinear chirp coefficients starts by specifying the desired microscope focal trajectory, which is related to but not the same as the AOL focal trajectory. I calculate the AOL focal trajectory and the associated ray-profile leaving the AOL. I then expand the ray-profile and identify the highest power n of terms involving $x^{n-m}t^m$. I represent the input ray-profile to the second AOD and the profile shift of the acoustic wave as generic n^{th}-order Taylor series, expanding each term entirely. I equate coefficients and attempt to solve for each Taylor coefficient.

6.3.1 *Linear drives (lateral line-scanning)*

As a proof-of-principle, I use the ray-profile method to re-derive the cylindrical AOL drive equations, Eq. (2.6). A key point to note from Eqs. (3.13) and (3.14) is that constant velocity lateral scanning by the AOL results in constant velocity lateral scanning after the objective. Thus, for lateral line-scanning I set the axial focal position to a constant and take the lateral position to have an arbitrary velocity: $x_{\text{AOL}} = x_0 + vt$, $z_{\text{AOL}}(t) = z_0$. Substituting these into Eq. (6.14) and then into Eq. (6.15) yields

$$\frac{\left(\tilde{x} - s\left[\Gamma_{-i}^{(1)} + \psi\theta_0\right] - x_0 - vt\right)^2}{2z_0} = \Gamma_{-i}(\tilde{x} - vt) + \Gamma_{-}(\tilde{x} + Vt) \quad (6.17)$$

I then expand the brackets on the left and Taylor expand the right in order to equate coefficients, dropping terms that are independent of x since these are global profile shifts and have no observable effect:

$$\begin{aligned} & \frac{-s\left[\Gamma_{-i}^{(1)} + \psi\theta_0\right] - x_0}{z_0}\tilde{x} + \frac{1}{2z_0}\tilde{x}^2 - \frac{v}{z_0}\tilde{x}t \qquad (6.18) \\ = \;& \Gamma_{-i}^{(1)}(\tilde{x} - Vt) + \frac{1}{2}\Gamma_{-i}^{(2)}(\tilde{x} - Vt)^2 + \Gamma_{-}^{(1)}(\tilde{x} + Vt) + \frac{1}{2}\Gamma_{-}^{(2)}(\tilde{x} + Vt)^2 \\ = \;& \left(\Gamma_{-i}^{(1)} + \Gamma_{-}^{(1)}\right)\tilde{x} + \frac{1}{2}\left(\Gamma_{-i}^{(2)} + \Gamma_{-}^{(2)}\right)\tilde{x}^2 - \left(\Gamma_{-i}^{(2)} - \Gamma_{-}^{(2)}\right)V\tilde{x}t \end{aligned}$$

Having expanded the position-time brackets on the far right, the relevant coefficients are of $\tilde{x}, \tilde{x}^2, \tilde{x}t$. I have left out $\Gamma_{2-}^{(n>2)}$ and $\Gamma_{2}^{(n>2)}$ because these are trivially zero. Equating coefficients with the additional pair deflection ratio relation of Eq. (3.17) I find

$$\begin{aligned} \Gamma_{-i}^{(1)} + \Gamma_{-}^{(1)} &= \frac{-s\left[\Gamma_{-i}^{(1)} + \psi\theta_0\right] - x_0}{z_0}, & \Gamma_{-i}^{(2)} + \Gamma_{-}^{(2)} &= \frac{1}{z_0} \qquad (6.19) \\ \Gamma_{-i}^{(1)} + \psi\theta_0 &= \mathcal{R}\left(\Gamma_{-}^{(1)} - \psi\theta_0\right), & \Gamma_{-i}^{(2)} - \Gamma_{-}^{(2)} &= \frac{v}{Vz_o} \end{aligned}$$

where $\mathcal{R}$ is the pair deflection ratio discussed in Section 3.1.4. Solving for the ray-profiles, I find

$$\Gamma_{-}^{(1)} = \psi\theta_0 - \frac{x_0}{\mathcal{R}(s+z_0)+z_0}, \qquad \Gamma_{-}^{(2)} = \frac{1-v/V}{2z_0} \tag{6.20}$$
$$\Gamma_{-i}^{(1)} = -\psi\theta_0 - \frac{\mathcal{R}x_0}{\mathcal{R}(s+z_0)+z_0}, \qquad \Gamma_{-i}^{(2)} = \frac{1+v/V}{2z_0}$$

I then back-propagate Γ_{-i} to find Γ_{+} using Eq. (6.9):

$$\Gamma_{+}^{(1)} = -\psi\theta_0 - \frac{\mathcal{R}x_0}{\mathcal{R}(s+z_0)+z_0}, \quad \Gamma_{+}^{(2)} = \frac{1+v/V}{2z_0+s(1+{}^{v}/_{V})} \tag{6.21}$$

I find that $\Gamma_{+}^{(n\geq 3)} = 0$. If I use Eq. (6.16) to relate the Taylor coefficients to the drive frequency coefficients, I recover both Eqs. (2.6) and (3.18), verifying this approach for linear chirps.

6.3.2 *Quadratic drives (arbitrary-direction-scanning)*

For arbitrary-direction line-scanning, the microscope focal trajectory has constant velocity. A complication is that this does not correspond to constant velocity scanning by the AOL. Rather, the axial-component of the focal position after the AOL is inversely related to the time t:

$$x_{\mathrm{AOL}} = \frac{x_0+vt}{1+\mathcal{C}t}, \qquad z_{\mathrm{AOL}}(t) = \frac{z_0}{1+\mathcal{C}t} \tag{6.22}$$

By Eqs. (3.13) and (3.14) this AOL focal position maps to the post-objective focal position as

$$x_{\mathrm{obj}} = \frac{-f_{\mathrm{obj}}(x_0+vt)}{Mnz_0}, \qquad z_{\mathrm{obj}} = \frac{-f_{\mathrm{obj}}^2(1+\mathcal{C}t)}{M^2nz_0} \tag{6.23}$$

where $\mathcal{C}$ is evidently proportional to the axial scan speed. Substituting Eq. (6.22) into Eq. (6.14) and dropping terms independent of x as before results in

$$\begin{aligned}
\Gamma_{-d}(t,\tilde{x}) &= \left(\tilde{x} - s\left[\Gamma_{-i}^{(1)} + \psi\theta_0\right] - \frac{x_0+vt}{1+\mathcal{C}t}\right)^2 \frac{1+\mathcal{C}t}{2z_0} \\
&= \frac{1+\mathcal{C}t}{2z_0}\left(\tilde{x}^2 - 2s\left[\Gamma_{-i}^{(1)} + \psi\theta_0\right]\tilde{x} - 2\frac{x_0+vt}{1+\mathcal{C}t}\tilde{x}\right) \\
&= \frac{-s\left[\Gamma_{-i}^{(1)} + \psi\theta_0\right] - x_0}{z_0}\tilde{x} + \frac{1}{2z_0}\tilde{x}^2 \\
&\quad - \frac{v + sC\left[\Gamma_{-i}^{(1)} + \psi\theta_0\right]}{z_0}\tilde{x}t + \frac{\mathcal{C}}{2z_0}\tilde{x}^2 t
\end{aligned} \tag{6.24}$$

Having expanded the brackets on the far right, the relevant coefficients are of $\tilde{x}, \tilde{x}^2, \tilde{x}t, \tilde{x}^2t, \tilde{x}t^2$. I now apply Eq. (6.15), Taylor expand

the right (ignoring terms independent of x) and equate coefficients, as in the preceding section:

$$\begin{aligned} & \Gamma_{-i}(\tilde{x}-Vt)+\Gamma_{-}(\tilde{x}+Vt) \qquad (6.25)\\ = \; & \Gamma_{-i}^{(1)}(\tilde{x}-Vt)+\frac{1}{2}\Gamma_{-i}^{(2)}(\tilde{x}-Vt)^2+\frac{1}{6}\Gamma_{-i}^{(3)}(\tilde{x}-Vt)^3+\\ & \Gamma_{-}^{(1)}(\tilde{x}+Vt)+\frac{1}{2}\Gamma_{-}^{(2)}(\tilde{x}+Vt)^2+\frac{1}{6}\Gamma_{-}^{(3)}(\tilde{x}+Vt)^3\\ = \; & \left(\Gamma_{-i}^{(1)}+\Gamma_{-}^{(1)}\right)\tilde{x}+\frac{1}{2}\left(\Gamma_{-i}^{(2)}+\Gamma_{-}^{(2)}\right)\tilde{x}^2-\left(\Gamma_{-i}^{(2)}-\Gamma_{-}^{(2)}\right)V\tilde{x}t+\\ & \frac{1}{6}\left(\Gamma_{-i}^{(3)}+\Gamma_{-}^{(3)}\right)\tilde{x}^3-\frac{1}{2}\left(\Gamma_{-i}^{(3)}-\Gamma_{-}^{(3)}\right)V\tilde{x}^2t+\\ & \frac{1}{2}\left(\Gamma_{-i}^{(3)}+\Gamma_{-}^{(3)}\right)V^2\tilde{x}t^2 \end{aligned}$$

I have not explicitly written out $\Gamma_{-i}^{(n>3)}$ and $\Gamma_{-}^{(n>3)}$ because they are all zero. Note that $\Gamma_{-i}^{(1)},\Gamma_{-}^{(1)}$ are unchanged from Eq. (6.20) and $\Gamma_{-i}^{(2)},\Gamma_{-}^{(2)}$ only need v replacing by $v+sC\left[\Gamma_{-i}^{(1)}+\psi\theta_0\right]$ to be valid here. Therefore, I equate coefficients for only $\tilde{x}^3$, $\tilde{x}^2t$ and $\tilde{x}t^2$ to find two new relations:

$$\Gamma_{-i}^{(3)}+\Gamma_{-}^{(3)}=0, \qquad \Gamma_{-i}^{(3)}-\Gamma_{-}^{(3)}=\frac{-\mathcal{C}}{Vz_0} \qquad (6.26)$$

These can be solved simultaneously to find

$$\Gamma_{-i}^{(3)}=\frac{-\mathcal{C}}{2Vz_0}, \qquad \Gamma_{-}^{(3)}=\frac{\mathcal{C}}{2Vz_0} \qquad (6.27)$$

As before, I back-propagate Γ_{-i} to find Γ_{+} using Eq. (6.9) and this time include up to the fourth order for completeness:

$$\Gamma_{+}^{(3)} = -\left[1+\frac{s}{2z_0}\left(1+\frac{v}{V}\right)\right]^{-3}\Gamma_{-}^{(3)} \qquad (6.28)$$

$$\Gamma_{+}^{(4)} = -3s\left[1+\frac{s}{2z_0}\left(1+\frac{v}{V}\right)\right]\Gamma_{+}^{(3)^2} \qquad (6.29)$$

I then relate the third order Taylor coefficients to the quadratic drive frequency coefficient c using Eq. (6.16). I conclude the quadratic drive derivation with the remark that I was able to get the right values for three coefficients of $\tilde{x}^3,\tilde{x}^2t,\tilde{x}t^2$ even though I could only choose values for two Taylor coefficients $\Gamma_{-i}^{(3)},\Gamma_{-}^{(3)}$; it was fortunate that the system of equations was linearly dependent. I do not have such good fortune if I attempt to use cubic chirps to produce accelerating lateral scans: the outgoing ray-profile is aberrated by a non-zero $\Gamma_{-d}^{(3)}$ coefficient, which I briefly discuss next.

6.3.3 *Cubic drives (parabolic curved-scanning)*

For curved scans, the microscope focal trajectory accelerates axially. In this case, the AOL trajectory denominators need adjusting to be parabolic:

$$x_{\mathrm{AOL}} = \frac{x_0 + vt}{1 + \mathcal{C}t + \mathcal{D}t^2}, \qquad z_{\mathrm{AOL}}(t) = \frac{z_0}{1 + \mathcal{C}t + \mathcal{D}t^2} \tag{6.30}$$

By Eqs. (3.13) and (3.14) this AOL focal position maps to a post-objective focal position where x_{obj} is linear in time and z_{obj} is quadratic:

$$x_{\mathrm{obj}} = \frac{-f_{\mathrm{obj}}(x_0 + vt)}{Mnz_0}, \qquad z_{\mathrm{obj}} = \frac{-f_{\mathrm{obj}}^2(1 + \mathcal{C}t + \mathcal{D}t^2)}{M^2 n z_0} \tag{6.31}$$

The derivation of ray profile Taylor coefficients is analogous to the previous derivations but with more and longer expressions. Therefore, I do not present it here but mention that when attempting to equate coefficients an additional and unwanted term corresponding to 2D spherical-like aberration has to be introduced. The resulting ray-profile where the last term corresponds to aberration is given by

$$\begin{aligned} \Gamma_{-d}(\tilde{x}, t) \quad = \quad & \left(\tilde{x} - s\left[\Gamma_{-i}^{(1)} + \psi\theta_0\right] - \frac{x_0 + vt}{1 + \mathcal{C}t + \mathcal{D}t^2}\right)^2 \frac{1 + \mathcal{C}t + \mathcal{D}t^2}{2z_0} \\ & + \frac{\mathcal{D}\tilde{x}^4}{12V^2 z_0} \end{aligned} \tag{6.32}$$

This result is analogous to the last line of Table 6.1, where axial acceleration and spherical-like aberration are introduced together. For small values of $\mathcal{D}/z_0$ the aberration term is negligible and good resolution with gently curving scan trajectories can be achieved.

6.3.4 *Impossibility of continuous periodic scanning*

Refilling AODs with new acoustic frequency ramps limits the AOL duty cycle. For some applications, it would be desirable to use a single periodic frequency ramp to repeatedly and continuously trace out a focal trajectory of interest with 100% duty cycle. It follows from the preceding ray-profile theory that such periodic scanning is impossible at high-speed without introducing intolerable levels of aberration.

Above quadratic drive frequencies (cubic, quartic, etc.), aberrations are necessarily introduced by a cylindrical AOL. I gave a concrete example for cubic chirps in Section 6.3.3, where 2D-spherical-like aberration was generated. The generality of this rule can be seen by noting that the term involving $x^{n>2}$ corresponds to aberration and the ray-profile coefficients $\Gamma_{-i}^{(n)}, \Gamma_{-}^{(n)}$ must be chosen to cancel out the x^n term. Subsequently, it is not possible to cancel out $x^{n-1}t$, which also corresponds to aberration for $n > 3$. These aberrations are not necessarily

large enough to matter in a practical sense and I have been able to use cubic drives to image curved surfaces with good resolution.

The Taylor expansion of any indefinite continuous scan trajectory would have an infinite number of terms. This is easily proven by noting a Taylor series of only a finite number of terms is not periodic. Of course, there could be pathological cases where a convergent Taylor series does not exist for a particular periodic trajectory. However, such cases would require an entirely different approach to frequency drive synthesis and I disregard it on those grounds. Putting this together with the preceding paragraph leads to the conclusion that aberration-free periodic scanning is impossible with a cylindrical AOL, and therefore with a spherical AOL too.

To follow up on the claim that aberrations can be negligible, it has been shown that slow-speed periodic scanning is possible [58]. However, the aberrations become larger the faster the scanning is performed because this is effectively a time-scaling of the frequency-time polynomial. Therefore, doubling scan-speeds will double aberration terms linear in time, quadruple terms quadratic in time and so on. Any aberration terms with a large time exponent will balloon, rapidly degrading the resolution to the point of being unusable. The rule is that any frequency ramp that deviates far from being linear over the scale of the AOD's aperture will produce significant aberrations.

The interest in continuous periodic scanning is to avoid the fill-time inactivity period that arises from needing acoustic ramps to propagate across the AOD apertures, and thereby achieve a 100% duty cycle. The options that remain open in the quest for 100% duty cycle are to explore intricate amplitude modulation or non-analytic frequency chirps (cannot be expressed by a convergent power series), though these both strike me as very implausible. It is worth emphasising that AOLs only suffer from a low duty cycle when imaging in pointing mode or using short line-scans (inactive for up to 95% of the total image acquisition period). In contrast, long line-scans have duty cycles of up to 80%, and the AOD fill-time is much less of an issue.

6.4 SIMULATION OF AXIAL LINE-SCANNING

To explore the benefits of the nonlinear equations derived using ray-profiles in Section 6.3 over those in Table 6.1 derived using a zero-AOD-spacing approximation, I have performed ray and FFT-based wave simulations of axial line-scanning with a cylindrical AOL microscope. The ray model clearly demonstrates stigmatic focusing over a range of z_{AOL} when an AOL with zero AOD spacing is driven with equal cubic chirps. When AOD spacing is increased (non-zero), aberrations appear. The scale of these ray aberrations can be reduced by properly scaling the value of c on the first AOD as per $\Gamma_{+}^{(3)}$ in Eq. (6.28), which is proportional to c according to Eq. (6.16). Further

improvements can be made by including higher-order chirp corrections on the first AOD, the first two of which are d as per $\Gamma_+^{(4)}$ in Eq. (6.29) and e as per $\Gamma_+^{(5)}$ for which I have not explicitly written out an expression for.

In practical microscope operation, it is the size of the PSF which is primarily of concern. I therefore used FFT-based wave simulations in 2D (using 1D FFTs) to explore the effect of the zero-spacing approximation on PSF size. In Fig. 6.2, I show the PSF from a number of snapshots of different axial scans. The axial scan used moved from $z_{\text{obj}} = -140\ \mu$m to $z_{\text{obj}} = 20\ \mu$m over a 20 μs period. Optical wavelength was 920 nm, acoustic velocity was 613 m/s and AOD apertures were taken as 16 mm. Figure 6.2(a) shows the PSF for an AOL with zero AOD spacing using equal c values on both AODs, for which rays would focus stigmatically in 2D. Figure 6.2(b) shows the PSF for a cylindrical AOL with non-zero AOD spacing (10 cm; equivalent to 5 cm spacing in spherical AOL), still using equal c values on both AODs. In this case, there is evidently some skew and the two-photon axial FWHM is elongated by 30%. Figure 6.2(c) shows the same axial scan as Fig. 6.2(b) but at a time when the focus is at $z_{\text{obj}} = 140\ \mu$m and therefore a large amount of spherical aberration is present due to being far from the objective's front focal plane. Such is the magnitude of the spherical aberration that the aberration visible in Fig. 6.2(b) has been completely dominated and is no longer visible.

Figure 6.2(d) shows the PSF for an AOL with non-zero AOD spacing (10 cm), but with the c value on the first AOD scaled as per Eq. (6.28), and d and e corrections added to the first AOD as per Eq. (6.29). Within the numerical resolution of the simulation, the PSF has the same axial FWHM as Fig. 6.2(a), though some minor PSF distortion is visible. Figure 6.2(e) is the same as Fig. 6.2(d) but without the e correction on the first AOD. Further PSF distortion is visible, with a 10% increase in the two-photon axial FWHM. Figure 6.2(f) is the same as Fig. 6.2(d) but without d or e corrections added to the first AOD. This is a pathological case: by 'correctly' scaling the c on the first AOD, the PSF has been degraded. The two-photon axial FWHM is 70% larger than for Figs. 6.2(a) and (d), so using too-short-a-truncation is worse than just using the equal c values as shown in Fig. 6.2(b).

To attempt an intuitive explanation of why truncating the power series can lead to worse aberrations if the series is too short, I begin by noting that acoustic waves are constructed around $t = 0$. As the scan progresses, the acoustic waves move across the AODs. Away from $t = 0$, higher-order terms contribute to lower-order aberrations. To illustrate this, consider a quartic chirp $d(t - x/V)^4 = dV^{-4}x^4 + dV^{-3}tx^3 + dV^{-2}t^2x^2 + dV^{-1}t^3x$, where the $dV^{-3}tx^3$ is analogous to a cubic chirp that grows in magnitude with time. Thus, the large amount of 2D-coma-like aberration seen in Fig. 6.2(f) is due to the absence of the $dV^{-3}tx^3$ chirp term. Thus, the analytic model has moved

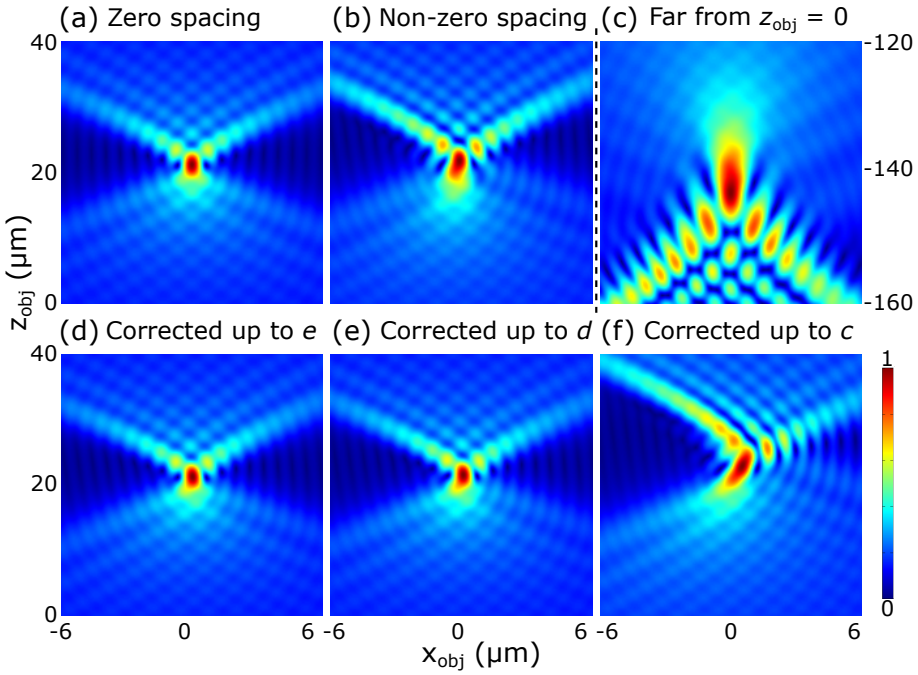

Figure 6.2: FFT-based wave simulations of 2D PSFs during axial scanning with a cylindrical AOL. Normalised optical field amplitude shown. (a) PSF for an AOL with zero AOD spacing using equal c values on both AODs. (b) PSF for an AOL with non-zero AOD spacing (10 cm), still using equal c values on both AOD. (c) The same axial scan as in (b) but at a time when the focus is at $z_{obj} = -140\,\mu$m. (d) PSF for an AOL with non-zero AOD spacing, but with the c value on the first AOD scaled and d and e corrections added to the first AOD, calculated theoretically. (e) Same as (d) but without the e correction on the first AOD. (f) Same as (d) but without d or e corrections added to the first AOD.

some of the cubic-chirp contribution into the higher-order drive coefficients on the first AOD, making a number of higher-order coefficients essential. In contrast, the zero-spacing approximation tries to put the cubic-chirp contributions on the cubic chirp alone so 2D-coma-like aberrations are small, unavoidable and not always negligible. By a similar argument, for larger times, e and then f terms might be expected to dominate the 2D-coma-like aberration since their contributions analogous to cubic chirps grow with t^2 and t^3 respectively. Based on this, I would speculate that more higher-order chirp correction terms would be required for longer scans than short scans, similar to fitting a power series to a sine curve. At any rate, it indicates the need to be careful when truncating the higher-order correction power series.

6.5 DISCUSSION

I have adapted geometric wavefront propagation theory to derive rules for ray-profile propagation. I have used the propagation rules to derive nonlinear drive coefficients for arbitrary-direction line-scanning and curved scanning with an AOL, without the need for a zero-AOD-separation approximation. This represents advances in both geometric optics and AOL drive theory.

Linearly-chirped acoustic waves introduce only curvature and deflection into an optical beam. Nonlinearly-chirped acoustic waves introduce time-dependent amounts of both of these plus unwanted aberrations. The key idea behind using nonlinear AOL frequency drives is that equal and opposite aberrations are introduced by the counter-propagating acoustic waves. These cancel out, leaving only the time-dependent curvature and deflection. A quadratically-chirped acoustic wave (c) will introduce a cubic phase aberration plus curvature with a linear dependence on time and is used for arbitrary-direction line-scanning by cancelling out the cubic phase aberration with the other counter-propagating acoustic wave. Similarly, cubic chirps will introduce a quartic phase aberration plus curvature with a quadratic dependence on time, which is used for curved-scanning. The aberrations introduced by the first AOD of a cylindrical AOL are cancelled out at the second AOD. Thus, when AOD spacings are allowed to be non-zero, the frequency ramp on the first AOD of a cylindrical AOL should theoretically differ slightly from the second AODs to allow for propagation of the optical field. The purpose of the ray-profile propagation theory I have developed is to determine the minor frequency adjustments that were needed to allow for AOD spacing.

I believe that the ray-profile propagation theory will be applicable to other areas of optics which make use of AODs, and potentially a wide range of other optical elements. It has two key advantages over the wavefront theory [110]. First, the ray-profiles are described along a plane (mathematically a line because the derivation is in 2D), which is convenient because optical elements are often modelled as thin. Second, there is no requirement to assume the central ray is propagating parallel to the optic axis. This is essential for use with diffractive devices and may be beneficial for optical setups which do not have a fixed optic axis. I have derived the ray-profile theory in 2D only, but extension to 3D should be easily achieved by replacing the chain rule with the appropriate partial derivatives. Computer algebra will be highly beneficial since the equations will be inconveniently long. Speculatively, I propose this geometric aberration propagation theory may be ideally suited for developing optical systems using flat metalenses, which are an emerging area of research [111].

The ray-profile propagation theory is a suitable tool for calculating nonlinear drive coefficients for a compact AOL. Previous calculations of nonlinear drive coefficients required the approximation of zero AOD spacing [3], which I have successfully removed. This has the potential to yield better image quality for the case of large chirps or long scans with an axial component. The inclusion of high-order chirp corrections poses a practical problem since frequency ramps are currently synthesised from only four coefficients a, b, c, d and higher coefficients e, f, g... cannot be included. Experiments using nonlinear chirps for arbitrary-direction scanning have been in remarkably close agreement with theory (see Chapter 7 for examples). However, to date, better results for curved scans have been achieved using the zero-spacing approximation than the analytic power series, which may be due to not being able to include the e frequency coefficient.

I have performed simulations of axial scanning to compare the zero-spacing approximation and my Taylor series solution. Using an FFT-based wave model for a range of realistic drive parameters, I found that the simulated AOL microscope's two-photon axial FWHM was 30% longer when I used a zero-spacing approximation than when I used the ray-profile Taylor series up to e. However, care must be taken when truncating drive frequency Taylor series: FFT simulations suggest using only a small number of Taylor series terms can actually make the PSF worse than using the zero-AOD-spacing approximation. In contrast, within the numerical accuracy of the simulations, the two-photon FWHM for an AOL with non-zero AOD spacing using ray-profile Taylor series chirps up to e was as good as for an AOL with zero AOD spacing. Away from the front focal plane of the microscope objective, spherical aberration dominates aberrations produced by the zero-spacing approximation.

It has previously been claimed that AOLs can image arbitrary user-defined trajectories [62]. However, it was achieved by fitting short lateral scans to an arbitrary path. This approach has a very low duty cycle for tightly curved trajectories since scans needed to be short to achieve an acceptable fit and gives an unavoidably poor fit for a trajectory moving axially. The drive frequencies for arbitrary-direction line-scanning and curved-scanning, which have been derived in this Chapter for a compact AOL, mean that AOL microscopes will be able to better fit their scans to regions of interest (see Chapter 7 for examples). The ability to efficiently fit scan trajectories to dendritic trees will enable a host of useful experiments to be performed for the first time.

7 IMAGING USING NONLINEAR DRIVES

In this Chapter I explore three new microscope imaging modes depicted in Fig. 7.1. These three imaging modes use nonlinearly-chirped drive frequencies (those defined by Eq. (2.10) with non-zero $c, d, \ldots$ coefficients). All AOL imaging reported to date has used linearly-chirped drive frequencies (only a and b coefficients in Eq. (2.10) are non-zero). Theory simplified by assuming zero AOD spacing and experimental proof-of-principle have indicated that nonlinear drives can enable arbitrary-direction line-scanning and curved-scanning with an AOL [3, 65, 72]. In Chapter 6 I derived more refined theory for nonlinear drives that allowed for non-zero AOD spacing. The use of nonlinear drives promises faster imaging by enabling scan trajectories to be fitted more efficiently to regions of interest and reduce the problem of small sample movement by imaging complete surfaces or volumes.

7.1 ARBITRARY PLANE IMAGES

Arbitrary plane mode shown in Fig. 7.1(a) is a generalisation of the full-frame line-scanning mode shown in Fig. 2.1(a). Conventionally, line-scans in the x-direction were used to image a square lying in the xy-plane as in Fig. 2.1(a). Arbitrary plane mode images a rectangle of any orientation and aspect ratio (ratio of the lengths of the rectangle's sides). The need for this imaging mode is that regions of interest can be imaged efficiently by fitting a rectangle to them but do not often sit conveniently in the xy-plane.

Some rectangles can be imaged using either laterally-orientated line-scans (linearly-chirped acoustic frequencies) or line-scans that have an axial component (nonlinearly-chirped acoustic frequencies). For example, a laterally-scanned xz-plane is shown in Fig. 7.2(b) and an axially-scanned xz-plane is shown in Fig. 7.2(c). This provides a way to directly compare the quality of images acquired using linear and nonlinear drives and I have acquired images using both fluorescent beads and neurons *in vivo* for this purpose. Figure 7.2(d) shows 1 μm beads images acquired using lateral and axial line-scans in the top and middle panels respectively. These two images are shown overlaid (green and magenta; overlap appears white) in the bottom panel, with no observable difference in resolution.

Figures 7.2(e) and (f) show neuronal images acquired from a mouse with a cranial window *in vivo*. These images were acquired using lateral and axial scans, and correspond to Figs. 7.2(b) and (c) respec-

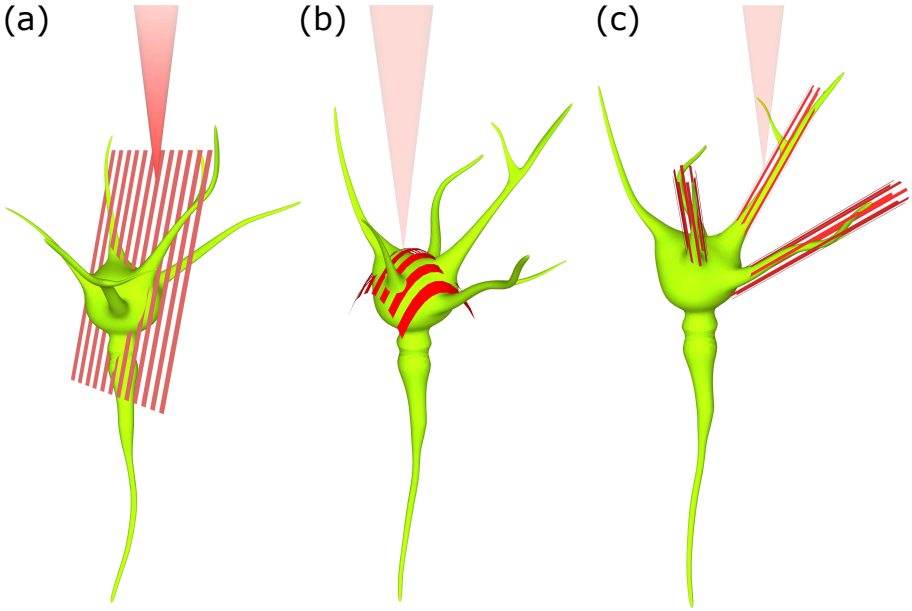

Figure 7.1: The three new imaging modes using nonlinear drives for an AOL microscope: (a) arbitrary plane, (b) curved surface, (c) glove. (Figure produced by Dr. G. Konstantinou)

tively. The red and green channels corresponds to the fluorescent indicators tdTomato and GCaMP6f [112]. There is no observable difference in the red channel, but the green channel does vary between the two because GCaMP6 is activity-dependent. Microscope resolution appears to be the same for images acquired using either lateral or axial line-scans. More detailed evaluation of the resolution could be achieved by imaging sub-micron beads to directly measure the PSF when imaging with lateral and axial line-scans. In particular, it would be interesting to see if the PSF of scans differed depending on scan-speed, scan-direction and where the scan was centred in 3D space.

To perform the axial scans, I calculated the first four drive frequency coefficients (a, b, c, d) using results from Section 6.3.2. In particular, as and bs were calculated using Eqs. (6.20) and (6.21), cs using Eqs. (6.27) and (6.28), ds using Eq. (6.29) (for line-scanning d is zero on X- and Y-), and Eq. (6.16) was used to convert from ray-profiles (Γ) to drive frequency coefficients. Higher-order coefficients $(e, f, \ldots)$ are not currently supported by the microscope hardware. I have described the control software I developed to perform nonlinear imaging with the AOL microscope in detail in Appendix D. An alternative way to calculate the drive coefficients a, b, c, d is to use the results of Table 6.1. These results assume AOD spacing is zero and are therefore simpler but at the potential expense of poorer image resolution. For many situations, simulations I have performed suggest that the reduction in image quality due to using results from Table 6.1 instead of Section 6.3.2 will be small if not negligible. Further experimental

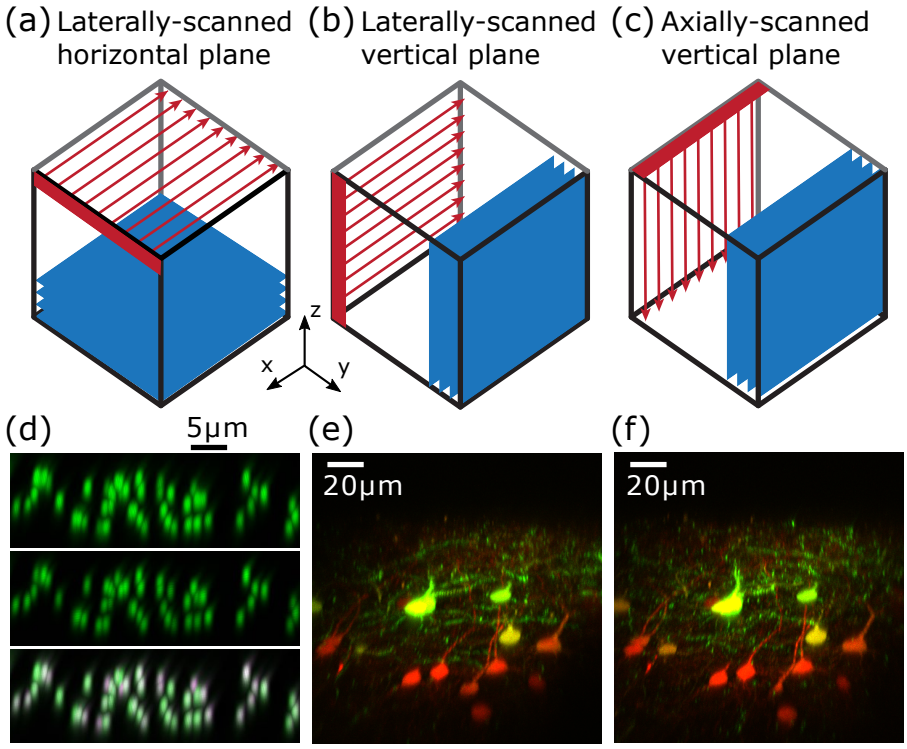

Figure 7.2: Imaging using axial scanning compared with lateral scanning. (a) Conventional full-frame line-scanning imaging: a series of line-scans in the x-direction are used to image an xy-plane. (b) Similar to (a) using series of line-scans in the x-direction but to image an xz-plane instead. (c) Imaging an xz-plane the same as (b) but using line-scans in the z-direction. (d) Images of 1 μm fluorescent beads in the xz-plane. Top acquired as (b), middle as (c), bottom is overlay of top and middle in green and magenta (overlap appears white). (e) and (f) *in vivo* neuronal imaging of mouse with cranial window. Red channel is tdTomato; green channel is GCaMP6f. (e) acquired as (b) and (f) acquired as (c). (Panels (a)–(c) produced by Dr. A. Valera)

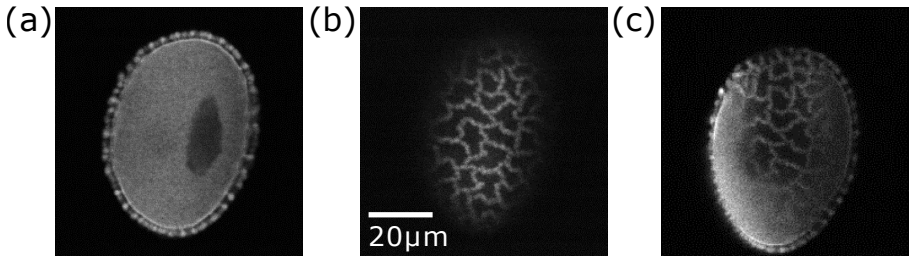

Figure 7.3: Large pollen grain (approximately 50 × 60 μm). (a) Line-scanned xy-plane through centre of the pollen grain. (b) Line-scanned xy-plane across surface of the pollen grain. (c) Curved-scanned ellipsoidal surface fitted to the surface of the pollen grain. Scale bar in (b) applies to (a) and (c) also.

work could be performed to quantify the merit of using the results of Section 6.3.2 over the simpler results of Table 6.1.

7.2 CURVED SURFACE IMAGES

Curved surface imaging, as shown in Fig. 7.1(b), fits continuous high-duty-cycle curved-scans efficiently to biological structures of interest that do not lie in a plane. As stated in Table 6.1 and Section 6.3.3, an issue with curved-scanning is that 2D-spherical-like aberration is introduced by a cylindrical AOL. In a spherical AOL, these combine to form a quatrefoil pattern aberration. Fortunately, for gentle curves (large radius of curvature) these aberrations appear to be negligible, though I cannot offer more precise quantification. Further experimentation and simulations could determine the effect of these aberrations more clearly. The curved-scans are theoretically parabolic but since the radius of curvature is large there is no practical distinction between parabolas and circles for the length of scans considered.

To demonstrate curve surface mode, I have imaged a pollen grain. Figure 7.3(a) shows a line-scanned xy-plane through the centre of the pollen grain, with detail visible at the edges but a uniform centre. Figure 7.3(b) shows a line-scanned xy-plane across the surface, which fades out quickly as the surface curves away from the xy-plane. In Fig. 7.3(c), I have fitted curved-scans to the pollen grain such that the surface detail is visible over the entire pollen grain. The curved-scans have trajectories of the form $z \propto x^2$. To achieve a better fit to the pollen grain, I imaged a curved-surface that is locally ellipsoidal (rather than cylindrical) by setting the axial apex of each curved-scan according to $z \propto y^2$. Both the edge seen in Fig. 7.3(a) and the surface in Fig. 7.3(b) are both visible indicating a good fit.

One issue I have encountered when acquiring curved-surface images is that the drive frequencies calculated using the analytic ray-profile method of Chapter 6 to account for non-zero AOD spacing do not perform well. Instead, I used the results of Table 6.1 to perform

curved-scans, implicitly assuming AOD spacing to be negligible. Although I do not have conclusive evidence, I strongly suspect the problem is that the microscope supports only four drive frequency coefficients (a, b, c, d). In Section 6.4, simulations indicated that the PSF was sensitive to how the drive frequency power series was truncated: axial line-scanning primarily uses c but also required at least d for a good PSF. Extrapolating, curved-scanning primarily uses d so I would expect at least e to be required for a good PSF.

7.3 GLOVE MODE

Glove mode shown in Fig. 7.1(c) is a minimal volumetric imaging protocol. The advantages of volumetric imaging are that regions of interest can be averaged and small sample movements do not ruin an experiment. In glove mode, high repetition rates are achieved by imaging only small volumes tightly fitted around regions of interest. Like arbitrary plane mode, glove mode makes use of arbitrary-direction line-scanning through the application of nonlinearly-chirped drive frequencies.

In developing glove mode, I have collaborated with Dr. A. Valera. We have leveraged the dendritic tracing features of Vaa3D [113] to automate line-scan fitting to regions of interest by integrating it with the microscope control software (see Appendix D). An outline of the glove mode work-flow is as follows: first, a full-frame volume is acquired by the microscope by performing a z-stack. The volume is rendered in 3D by Vaa3D as shown in Fig. 7.4(a). The user then roughly traces out neurons by dragging the mouse cursor which Vaa3D fits to the nearest structures in the 3D image. Alternatively Vaa3D allows fully automated tracing of the neuronal morphology. The Vaa3D traces are used by MATLAB to calculate a minimum-bounding cuboid around each trace, shown in Fig. 7.4(b). The line-scan direction for each cuboid is chosen to align with the longest axis to maximise imaging speed. The selected volumes are then imaged at high-speed and a 3D time-lapse of the regions is acquired for analysis. A snapshot of such a time-lapse is shown in Fig. 7.4(c).

Despite being volumetric, glove mode can achieve fast acquisition speeds. For a ball-park example, a dendrite may be traced using a 4×5 grid of line-scans, with each line-scan taking 50 μs. This yields a speed of $1/N$ kHz when imaging N dendrites. This figure depends sensitively on the desired resolution, length of the dendrites and the straightness of the dendrites. In future, if curved-scans are also used in glove mode, regions of dendrites with near-uniform curvature could be imaged using fewer scans. A current limitation of the AOL microscope acquisition system is line-scan duration is set by a single parameter and takes milliseconds to change. Consequently, when imaging using line-scans at high-speed, all line-scans must have

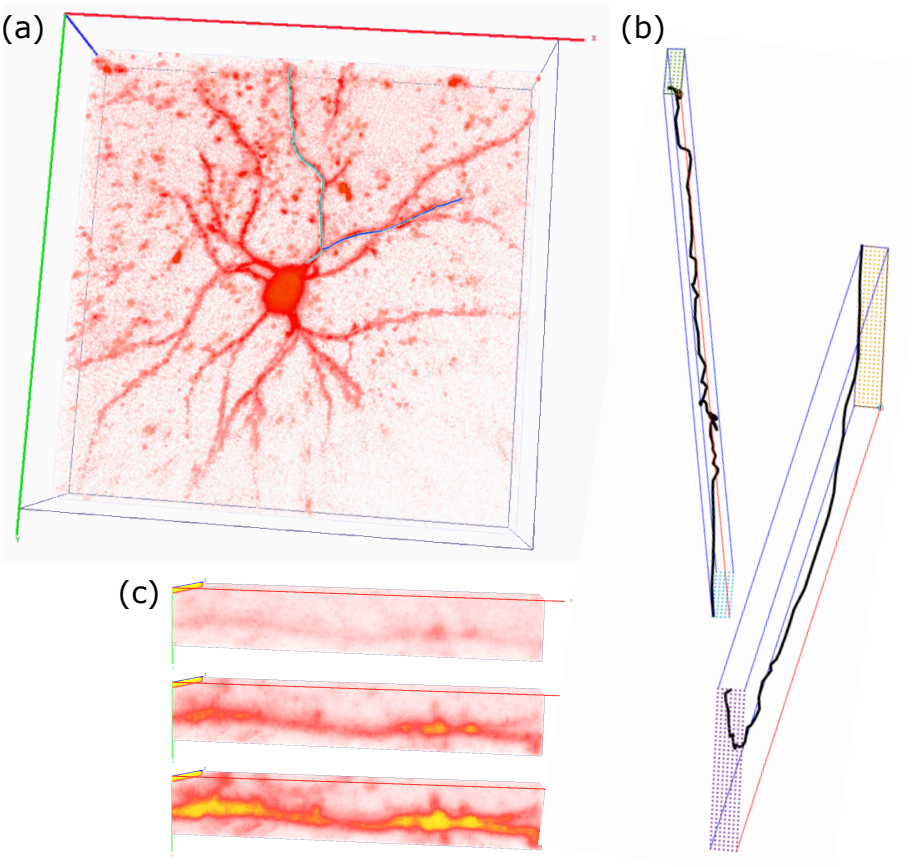

Figure 7.4: (a) 3D rendering in Vaa3D with user-defined neuronal tracings using tdTomato and GCaMP6 fluorescent dyes. Fluorescent signal shown in red; two dendrites have been traced, shown in blue and cyan respectively. (b) Fitting cuboids to neuronal tracings in MATLAB. The dots on each end of the cuboids indicate the start and stop positions of each line-scan. (c) Three snapshots of a 3D time-lapse of a dendrite section rendered in Vaa3D. This image corresponds to one of the cuboids shown in (b). This signal is from activity-dependent GCaMP6, with strong signal shown in yellow. The three snapshots depict increasing levels of dendritic activity, from top to bottom. (Data acquired by Dr. A. Valera)

the same temporal length. This is an issue when imaging dendrites of different lengths in glove mode because line-scans need to have different scan-speeds for them to have the same temporal length. Alternatively, line-scans can be forced to all be as long as the longest dendrite. Both of these solutions are inefficient and Dr. V. Griffiths is currently working on removing this limitation of the acquisition system.

7.4 DISCUSSION

I have implemented AOL microscope control software that uses the nonlinear drive theory I developed in Chapter 6 and used it to demonstrate new, nonlinear imaging modes with an AOL. In collaboration with Dr. A. Valera and Miss C. Baragli, I have experimentally demonstrated arbitrary-direction line-scanning of a mouse brain *in vivo* using an AOL microscope. I found no observable difference between laterally-scanned images acquired using linear drives and axially-scanned images using nonlinear drives, and I was surprised that no calibration was needed when switching between the two. In collaboration with Dr. P. A. Kirkby, I have experimentally demonstrated curved-scanning of a pollen grain surface. These proof-of-principle experiments largely demonstrate that nonlinear chirps work as expected in an AOL microscope. One complication was the the drive frequencies calculated using the theory of Chapter 6 for curved-scanning did not perform well. I expect this is because the AOL microscope control system currently only supports drive frequencies up to fourth-order in time (a, b, c, d) but a more detailed examination is needed.

When using nonlinear frequency drives, individually the AODs produce aberrations in the optical wavefront. For nonlinear drives to be useful, the AODs in a cylindrical AOL must produce equal and opposite aberrations that cancel out, as described in Chapter 6. Any error in frequency ramp timings will lead to incomplete cancellation of any time-dependent aberrations. For a quadratic chirp (c), the curvature is time-dependent and ramp timing errors will produce astigmatism. For a cubic chirp (d), a third-order phase aberration is produced linear in time. Such aberrations will spoil the PSF and therefore careful synchronisation of the frequency ramp timings is required when using nonlinear frequency drives. In the case that the chirps are linear, timing offsets produce only a lateral focal shift and point spread quality is unaffected. This explains why frequency ramp timings have not previously received much attention nor needed such precise calibration. The fact that good quality images were produced using nonlinear frequency drives shows that the ramp timings have been successfully tuned in order for the counter-propagating acoustic waves to balance each other out and produce a stigmatic focus.

The primary benefit of nonlinear chirps for AOL microscopes is that they enable new imaging modes, which offer faster imaging rates by better fitting regions of interest and reduce the problem of small sample movements by imaging areas and volumes instead of isolated points. As stated in Section 7.1, planes of arbitrary orientation can be imaged using only lateral line-scans and therefore require only linear drives. However, nonlinear drives enable the most efficient line-scan direction to be used. For illustration, when imaging a tall-but-narrow rectangle lying at 45^{o} to the z-direction with a desired resolution of 40×400 pixels (laterally narrow, axially long; reasonable dimensions for a section of dendrite), the speed up by using nonlinear drives is a factor of 6 for 50 ns dwell times. A more subtle benefit of imaging planes and volumes instead of isolated points is that regions can be averaged in a variety of ways to improve the signal to noise ratio. Imaging modes that acquire points in isolation may seek to improve signal to noise by increasing dwell time. However, this is quickly limited by the tendency of biological samples to sustain damage under prolonged illumination.

Of the three new imaging modes, I expect glove mode will find the greatest utility. The ability to image large sections of multiple dendrites, axons and somata efficiently will enable synaptic integration to be studied in new ways. With the high-speed of the scans, it could be possible to visualise the propagation of action potentials through the axon, soma and multiple dendrites of a neuron, and discern between local and global activity. The automated tracing software feature of Vaa3D hugely simplifies the microscope-user's task of specifying what regions for the microscope to trace and makes glove mode accessible to experimentalists. Very recently, Dr. V. Griffiths, Dr. A. Valera and I have succeeded in integrating real-time movement correction [74] with the nonlinear imaging mode software, though this is very preliminary and only the most basic testing of movement-corrected imaging has been performed with this software. Movement correction uses short and fast line-scans to identify sample movements and shift drive frequencies to compensate in real-time. This will mean that volumes can be more tightly fitted to regions of interest in glove mode since sample movement will not be a concern. Further development is required to make movement corrected glove mode accessible to experimentalists.

8

SPHERICAL ABERRATION CORRECTION

In an AOL microscope, light passes through an AOL and is relayed into a microscope objective [61]. The microscope objectives used are infinity corrected, which means they are designed to focus collimated light beams in their front focal plane. When the AOL adds curvature to shift the focus out of the objective's front focal plane, the focus suffers from spherical aberration as seen by comparing Figs. 8.1(a) and (b), and the axial resolution is reduced as shown in Fig. 8.1(e). It has been shown that AODs can be used for aberration correction by using nonlinearly chirped acoustic drives [65] and therefore a natural approach to correcting the spherical aberration would be to use the AOL itself without additional optical components. However, it has been proven theoretically that the conventional AOL design consisting of four AODs (4-AOD AOL) is unable to correct for spherical aberration [3], which is illustrated in Figs. 8.1(c) and (e). To overcome this limitation of the 4-AOD AOL, a new AOL design (6-AOD AOL) has been proposed [3] consisting of six AODs oriented in increments of 60^{o} as shown in Fig. 8.1(f). The theory indicates that a 6-AOD AOL would be able to correct for spherical aberration using cubic frequency chirps as illustrated in Figs. 8.1(d) and (e).

A challenge with driving the 6-AOD AOL is that the AODs are not orthogonal. Therefore the AODs must be considered simultaneously and a full 3D treatment is required. This contrasts with the conventional 4-AOD AOL in which the action of the four AODs can be decoupled into two pairs acting in the orthogonal x and y-directions respectively and can be understood in 2D. The geometric aberration theory I developed in Chapter 6 can be straightforwardly generalised to 3D, as would be necessary for a 6-AOD AOL. However, the arguments used to apply the theory to the 4-AOD AOL cannot be used for the 6-AOD AOL. For the 4-AOD AOL, in Section 6.2 I simply considered a cylindrical AOL, which consists of two AODs. The 1D optical field incident at the first AOD and leaving the last AOD were both specified, which enabled the 1D field to be determined in between the AODs. For a 6-AOD AOL the optical field incident at the first AOD and leaving the last AOD can both be specified in 2D, rather than 1D. Despite the additional dimension of the optical field, I cannot see how to systematically determine the 2D optical fields in between each of the six AODs (five gaps). This problem is made harder by the enormity of the equations involved, which require a computer algebra system to formulate and solve. Consequently, when calculating nonlinearly-chirped frequency drives for the 6-AOD AOL, the

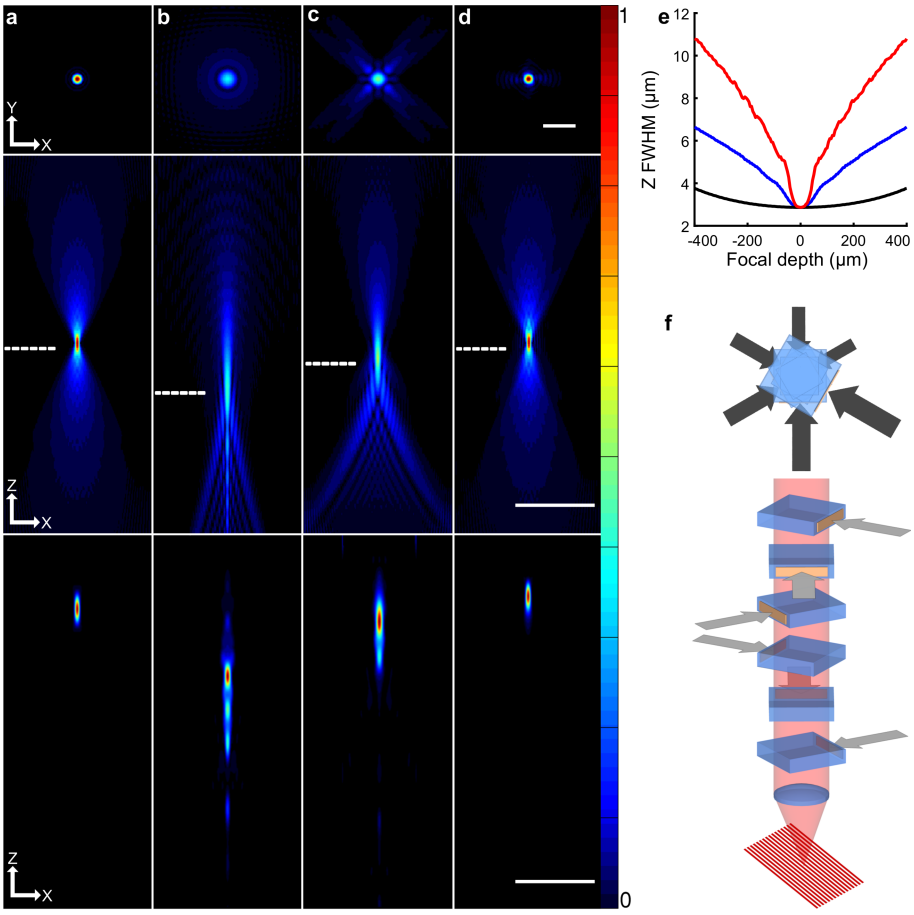

Figure 8.1: Model comparing effectiveness of 4-AOD AOL and 6-AOD AOL at correcting spherical aberration. (a)–(d) Calculated using Fourier model described in Section 8.1.1, top: xy amplitude profile at location indicated by dashed lines in middle panel, middle: xz amplitude profile, bottom: xz two-photon profile. a Focus without spherical aberration. (b) Focus with spherical aberration. (c) Attempted correction of spherical aberration using (standard) 4-AOD AOL. (d) Correction of spherical aberration using 6-AOD AOL. Scale bars from top to bottom: 1 μm, 5 μm, 5 μm. (e) Relationship between full width half maximum of two-photon excitation in xz plane and number of waves of spherical aberration introduced, for uncorrected (red), 4-AOD AOL corrected (blue) and 6-AOD AOL corrected. (f) Top: direction of acoustic waves in 6-AOD AOL; bottom: diagram of 6-AOD AOL and spherical lens controlling an optical beam. The code for generating (a)–(e) is available online [5]. (Published in [3], panel (f) produced by Dr. G. Konstantinou)

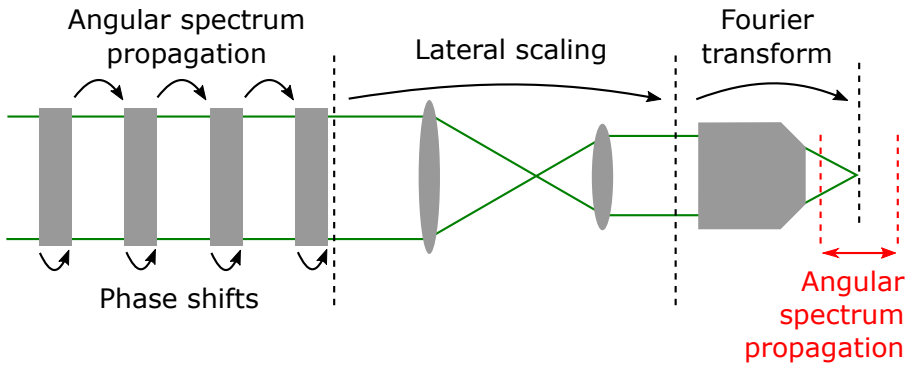

Figure 8.2: Outline of the AOL microscope Fourier model. AODs shown on the left, magnifying 4f relay in the centre and objective on the right.

zero-AOD-spacing approximation is used, analogously to the results in Table 6.1 for a cylindrical AOL. In particular, this means that the nonlinear chirps used for spherical aberration correction have been calculated using this approximation.

In this Chapter, I begin by modelling the spherical aberration associated with axial focal displacements to evaluate correction using a 4-AOD and a 6-AOD AOL. This modelling has been published in [3]. Despite the difficulties in accounting for non-zero AOD spacing in a 6-AOD AOL, I succeed in deriving the drive equations needed to calculate the linear chirps required for a 6-AOD AOL to focus stigmatically. The 6-AOD AOL drive equations are analogous to Eq. (2.7) for the 4-AOD AOL. Finally, I apply the numerical ray-based model from Chapter 4 to compare the predicted field of view with that of a 4-AOD AOL.

8.1 MODELLING AOL MICROSCOPE ABERRATIONS

8.1.1 *AOL wave model in 3D*

One of the main motivations for developing AOL-based wavefront shaping is to correct for aberrations during AOL-based 3D microscopy. Dr. P. A. Kirkby had modelled AOL aberrations in 2D using an Fourier-transform-based model with an excellent fit to experimental results (Fig. 4 of [3]). I have therefore extended this approach, generalising to full 3D aberrations by using 2D FFTs in a complete microscope context.

My FFT AOL model is outlined in Fig. 8.2: each AOD was modelled as a phase shift depending on the drive frequencies. Angular spectrum propagation (using FFTs) was used to move the optical wave from one AOD to the next. The magnifying 4f relay was modelled as a lateral scaling of the optical wave. To simulate an infinity-corrected

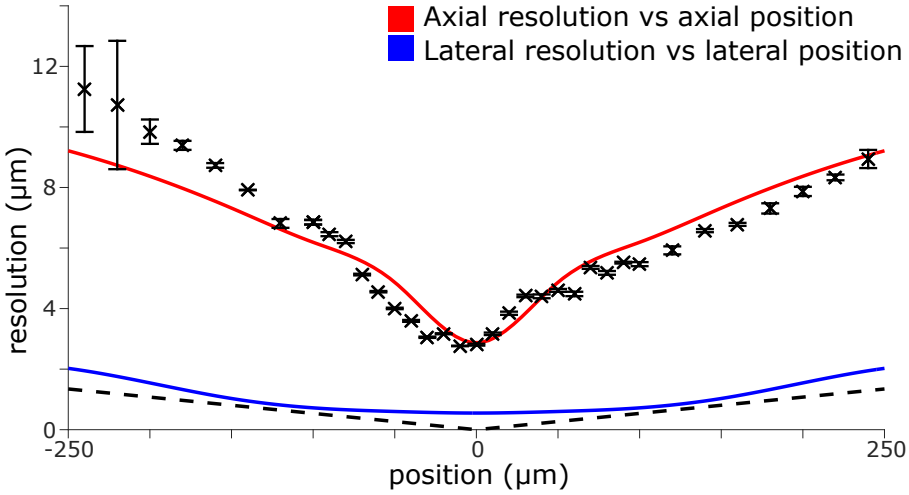

Figure 8.3: AOL microscope resolution. Black crosses with error bars and red line show axial resolution against axial position. Blue line and dashed black line shown lateral resolution against lateral position. Black crosses with error bars are experimental data measured by Dr. G. Konstantinou (poor signal to noise ratio at -200 μm led to the two large error bars; slight asymmetry possibly due to aberration introduced by the sample or slight misalignment of microscope's optical path). Red and blue lines are simulated data using my Fourier model. I calculated the dashed black line using Eq. (8.1).

objective, the optical wave at the back focal-plane of the objective was Fourier transformed (using an FFT) to calculate the field in its front focal plane of the objective. My rationale for using a Fourier transform to model the infinity-corrected objective is that a Fourier transform maps the sine of incidence angles to lateral positions, which is necessarily satisfied by the microscope objective (in the forward direction only) in order to be aberration-free. Additionally, [109] shows the optical field in front and back focal-planes are Fourier transform pairs under paraxial conditions and therefore the correct plane to use at the rear of the objective is the back focal-plane. Finally, the field in the natural focal plane was forward and back-propagated to calculate the full 3D optical field in the focal region. The 4f relay magnification was set at 0.8 and a 20$\times$ water immersion objective lens (NA $\simeq$ 0.7) was used. The input optical beam had a flat phase-profile and a Gaussian amplitude profile of 5.6 mm $1/e$ width.

In the simplest case, the model considers a single wavelength and single instant in time. By repeatedly running simulations over a range of wavelengths and times, the model can simulate chromatic dispersion and temporal effects. To account for spatial chromatic dispersion, multiple optical wavelengths were used, weighted to fit 140 fs laser pulses (5 nm FWHM at 800 nm wavelength; 7 nm FWHM at 920 nm). The optical fields for different wavelengths were added in quadra-

ture, appropriate for calculating time-averaged intensity. I used this to predict the resolution of the AOL microscope as shown in Fig. 8.3. The black crosses with error bars in Fig. 8.3 are experimental measurements (made by Dr. G. Konstantinou) of axial resolution against axial position that are in agreement with the red line I calculated using the model. I repeated the model simulation using only a single wavelength which made negligible difference. Thus the degradation in resolution can be attributed to spherical aberration. The threefold increase in resolution over a typical axial range makes spherical aberration a serious limitation of AOL microscopes. The blue line indicates the average dependence of lateral resolution on lateral focal position and is nearly independent of axial focal position. I calculated the dashed black line using a simple equation for angular chromatic dispersion that follows from Eqs. (3.14) and (3.15):

$$\frac{\Delta x_{\text{obj}}}{x_{\text{obj}}} = \frac{\Delta\lambda}{\lambda} \tag{8.1}$$

where x is the lateral position, Δx is the lateral spatial FWHM, λ is the centre wavelength and $\Delta\lambda$ is the wavelength FWHM. The dashed black line demonstrates that chromatic effects cause the deterioration of lateral resolution.

8.1.2 *Simulated spherical aberration correction*

I used the FFT AOL model to simulate the correction of spherical aberration by spherical AOLs. Figure 8.1(a) shows the predicted xy and xz amplitude profiles of an optical field free from spherical aberration, together with the xz two-photon profile below. Figure 8.1(b) shows how the amplitude field is altered when 10 waves of spherical aberration were added to the simulation.

When 5 waves of fourth-order phase per AOD we added to a conventional AOL consisting of four AODs, part of the spherical aberration could be compensated for, producing a higher amplitude at the focal spot, Fig. 8.1(c). Examination of the xy-projection revealed that a weak quatrefoil aberration remained, due to the inability of orthogonally arranged AODs to generate cross terms, as discussed in [65]. Nevertheless, the 4-AOD AOL could compensate for 50% of the axial elongation of the two-photon profile induced by aberrations over a focal range of ±400 μm at NA = 0.7 as illustrated by Figs. 8.1(c) and (e). Interestingly, applying the model to a 6-AOD AOL showed almost complete compensation over the focal range as illustrated by Figs. 8.1(d) and (e). In order to compensate 10 waves of spherical aberration, corresponding to ±375 μm of defocus, we required 4.7 waves of fourth-order acoustic phase per AOD. The capacity to fully correct spherical aberration means that a 6-AOD AOL mi-

croscope has the potential to image at higher spatial resolution over a larger axial range than existing AOL microscopes.

8.2 6-AOD AOL DRIVE EQUATIONS

There is good theoretical and experimental evidence that suggests that a 6-AOD AOL could correct spherical aberration. However, each AOD in an AOL must be driven with precise time-dependent frequency chirps in order to scan and focus light. In this Section I derive the drive equations for a 6-AOD AOL that allow for non-zero AOD spacing. The drive equations are used to calculate linear frequency chirps to focus light stigmatically with a chosen focal length and lateral scan velocity. Until now, drive equations had been derived only for a few AOL designs in which the orientation of the acoustic waves are restricted to the $\pm x$ and $\pm y$-directions (see Section 2.3). Deriving the drive equations for a 6-AOD AOL is more difficult because the AODs are not orthogonal.

In this Section, I develop a matrix formalism that can handle any number of AODs arranged at oblique angles, based on matrices. I have used the formalism to derive the drive equations for the 6-AOD AOL and explore their properties. The drive equations are used to calculate the linear chirp coefficients (the bs). The key simplification is that drive ramp power series Eq. (2.10) is restricted to being linear in time as in Eq. (2.2). The advantage of the linear algebra approach opposed to the recursive ray equation is that the algebra clearly allows the linear chirps to be solved for independently of the constant frequency coefficients. Thus, the problem of calculating AOL drive frequencies becomes two sequential tasks: find the linear chirps and then find the constant coefficients. To subsequently include nonlinear chirps ($c, d, \ldots$) for axial scanning or spherical aberration correction, these are added on separately, calculated using a zero-AOD-separation approximation.

8.2.1 *2D matrix derivation*

The propagation of rays through an AOL driven with linear chirps can be described by matrices. Assuming acoustic waves are restricted to the $\pm x$ directions as in a cylindrical AOL, a 2D treatment suffices and 2×2 matrices can be used. Recalling Eqs. (3.3) and (3.2) and restricting the acoustic chirps to be linear as in Eq. (2.2), the recursive equation for ray propagation in 2D (x, z) through an AOD with acoustic wave travelling in the positive x-direction becomes

$$x_{n+1} = x_n + m_n s_n \tag{8.2}$$

$$m_n = m_{n-1} + \frac{\lambda}{V}\left[a_n + b_n\left(t - \frac{x_n}{V}\right)\right] \tag{8.3}$$

where $m_n = k_{nx}/k_{nz}$, which is the gradient of the ray. In Eq. (8.3) I have assumed the AOD is diffracting into the $+1$ mode; an assumption that can be easily removed later on. These two equations correspond to physically distinct processes. Equation (8.2) describes ray propagation through the space between AODs and Eq. (8.3) describes diffraction by the AOD. I converted these two equations into two separate ABCD matrix equations [114] with an additional, time-dependent column-matrix necessary for diffraction angle:

$$\begin{pmatrix} x' \\ m' \end{pmatrix} = \begin{pmatrix} 1 & s \\ 0 & 1 \end{pmatrix}\begin{pmatrix} x \\ m \end{pmatrix} \tag{8.4}$$

$$\begin{pmatrix} x' \\ m' \end{pmatrix} = \begin{pmatrix} 1 & 0 \\ -\frac{\lambda b}{V^2} & 1 \end{pmatrix}\begin{pmatrix} x \\ m \end{pmatrix} + \frac{\lambda}{V}(a+bt)\begin{pmatrix} 0 \\ 1 \end{pmatrix} \tag{8.5}$$

The matrix in Eq. (8.4) is readily identified as the textbook free-space propagation transformation. The use of unprimed and primed position and gradient variables x, m here is to indicate the values before and after propagation. Equation (8.5) is a little more unusual: the first term on the right-hand side is the standard ABCD matrix for propagation through a thin lens but the second term is non-standard and accounts for the AOD's time-dependent deflection angle. For an AOD with acoustic waves travelling in the negative x-direction, the sign of the second term on the right-hand side of Eq. (8.5) needs changing. If the AOD operates in the -1 mode then the signs of a and b need changing wherever they appear in Eq. (8.5).

8.2.2 *3D matrix derivation*

When the acoustic directions in an AOL are not restricted to $\pm x$ and $\pm y$, a full 3D treatment is necessary and 4×4 matrices are required. I determined the 3D version of Eq. (8.5) to be

$$\begin{pmatrix} x' \\ y' \\ m'_x \\ m'_y \end{pmatrix} = \begin{pmatrix} \mathbb{I} & \mathbb{O} \\ -\mathbb{T} & \mathbb{I} \end{pmatrix}\begin{pmatrix} x \\ y \\ m_x \\ m_y \end{pmatrix} + \frac{\lambda\,(a+bt)}{V}\begin{pmatrix} 0 \\ 0 \\ \cos\theta \\ \sin\theta \end{pmatrix} \tag{8.6}$$

where $\mathbb{I}$ is the 2×2 identity, $\mathbb{O}$ is the 2×2 matrix of zeros and $\mathbb{T}$ is the matrix defined below

$$\mathbb{T} = \frac{\lambda b}{V^2}\begin{pmatrix} \cos^2\theta & \cos\theta\sin\theta \\ \cos\theta\sin\theta & \sin^2\theta \end{pmatrix} \tag{8.7}$$

The 3D version of Eq. (8.4) is standard [114, 115]:

$$\begin{pmatrix} x' \\ y' \\ m_x' \\ m_y' \end{pmatrix} = \begin{pmatrix} \mathbb{I} & s\mathbb{I} \\ \mathbb{O} & \mathbb{I} \end{pmatrix} \begin{pmatrix} x \\ y \\ m_x \\ m_y \end{pmatrix} \tag{8.8}$$

To make working with the preceding matrix equations more compact, I introduce the follow notation:

$$\begin{aligned} \mathbb{P} &= \begin{pmatrix} \mathbb{I} & s\mathbb{I} \\ \mathbb{O} & \mathbb{I} \end{pmatrix} \qquad \mathbb{Q} = \begin{pmatrix} \mathbb{I} & \mathbb{O} \\ -\mathbb{T} & \mathbb{I} \end{pmatrix} \\ \mathbf{x} &= \begin{pmatrix} x \\ y \\ m_x \\ m_y \end{pmatrix} \qquad \mathbf{q} = \frac{\lambda\,(a+bt)}{V} \begin{pmatrix} 0 \\ 0 \\ \cos\theta \\ \sin\theta \end{pmatrix} \end{aligned} \tag{8.9}$$

The significance of the terms is as follows: $\mathbb{Q}$ determines whether the AOL will focus stigmatically and the focal length, $\mathbf{q}$ determines the time-dependent xy-position of the focus, and $\mathbb{P}$ propagates the rays between AODs. The formalism developed here is most useful for calculating the linear chirps (the bs).

8.2.3 *Example: 3-AOD AOL drive equations*

Here I show how to apply the matrix formalism to an AOL comprising three AODs equally spaced and arranged at 120° angles. The example is easy to extend to an AOL with any spacings and at any angles. Modelling the AOL is a matter of applying Eqs. (8.6) and (8.8) successively to the initial ray state-vector $\mathbf{x}$, where diffraction by the n^{th} AOD is represented by multiplying by $\mathbb{Q}_n$ and adding $\mathbf{q}_n$, and subsequent propagation to the next AOD or the focal plane is represented by multiplying by $\mathbb{P}_n$:

$$\mathbf{x}' = \mathbb{P}_3\left[\mathbb{Q}_3\mathbb{P}_2\left[\mathbb{Q}_2\mathbb{P}_1\left[\mathbb{Q}_1\mathbf{x}+\mathbf{q}_1\right]+\mathbf{q}_2\right]+\mathbf{q}_3\right] \tag{8.10}$$

Expanding this yields terms which can be separated to give a time-independent matrix and a sum of column-vectors linear in time:

$$\begin{aligned} \mathbf{x}' &= \mathbb{P}_3\mathbb{Q}_3\mathbb{P}_2\mathbb{Q}_2\mathbb{P}_1\mathbb{Q}_1\mathbf{x} \\ &+ \left\{\mathbb{P}_3\mathbb{Q}_3\mathbb{P}_2\mathbb{Q}_2\mathbb{P}_1\mathbf{q}_1 + \mathbb{P}_3\mathbb{Q}_3\mathbb{P}_2\mathbf{q}_2 + \mathbb{P}_3\mathbf{q}_3\right\} \end{aligned} \tag{8.11}$$

The required constraint for a focus moving with lateral velocity (v_x, v_y), Eq. (3.1.3) can be expressed as

$$[\mathbb{P}_3\mathbb{Q}_3\mathbb{P}_2\mathbb{Q}_2\mathbb{P}_1\mathbb{Q}_1]_{11,12,21,22} = \mathbb{O} \tag{8.12}$$

$$[\mathbb{P}_3\mathbb{Q}_3\mathbb{P}_2\mathbb{Q}_2\mathbb{P}_1\dot{\mathbf{q}}_1 + \mathbb{P}_3\mathbb{Q}_3\mathbb{P}_2\dot{\mathbf{q}}_2 + \mathbb{P}_3\dot{\mathbf{q}}_3]_{1,2} = \begin{pmatrix} v_x \\ v_y \end{pmatrix}$$

where $\dot{\mathbf{q}}_n$ is the time-derivative of $\mathbf{q}_n$ which depends on b_n and not a_n. The notation $[\,]_{11,12,21,22}$ indicates the four top-left elements of a 4×4 matrix and $[\,]_{1,2}$ indicates the top two elements of a 4-element column vector. Because this method considers only linear chirps, the axial velocity is necessarily zero. The desired b_ns are the solutions to the above equation. The 4×4 matrices are too extensive to multiply out by hand. To solve these equations for the bs, I used MATLAB's Symbolic Math Toolbox. For the 3-AOD AOL, there is a solution for a stationary focal position when $s = 0$:

$$b_1 = b_2 = b_3 = \frac{V^2}{\lambda}\frac{2}{3z_{\text{AOL}}} \tag{8.13}$$

Once the linear chirps are determined the hard work is done and it remains to constrain each a_n. Whilst this is possible using matrices, I have found it far more practical to use the base ray as described in Section 3.1.3. Applying the matrix method to the conventional compact AOL yields the drive equations given in [61] (note that I have used Cartesian coordinates whereas [61] describes lateral deflections using angles). The solution for the proposed AOL comprising six AODs [3] is discussed in Section 8.2.4. To recapitulate, the linear algebra approach presented here is a compact method for calculating the linear chirps required for an AOL to produce a stationary focus or one moving with constant lateral velocity.

8.2.4 *6-AOD AOL drive equations*

The 6-AOD AOL considered here has a *cyclic* arrangement: consecutive AODs are rotated by 60° as shown in Fig. 8.1(f). This is analogous to 4-AOD AOLs which have consecutive AODs rotated by 90°. The cyclic arrangement belongs to a group with the property that the optical beam is not parallel to the input or output at any stage inside the AOL. The benefit of this property is that undiffracted components of beams can be blocked with an aperture after the AOL, providing the operational drive frequency bandwidth does not exceed the minimum drive frequency. An example of another arrangement with this property would be $0°, 60°, 120°, 300°, 240°, 180°$. An example of an arrangement that does not have this property would be $0°, 180°, 120°, 300°, 240°, 120°$ for which the beam is near-parallel to the input and output after each pair of AODs. I have derived the drive equations for every arrangement that has this desired property

and have not found any with an (obvious) advantage over the cyclic arrangement. Therefore, I have used the cyclic arrangement throughout this Chapter.

I took the optical distance separating AODs to be $s = 5$ cm, and the distance from the sixth AOD to the focus to be z_{AOL} (for high efficiency, $|z_{\mathrm{AOL}}| > 1$ m). I have derived drive equations for the 6-AOD AOL with a stationary focal position. Additionally, I have derived the drive equations for a focus moving with arbitrary speed but restricted to scan at one of the angles $0^{\mathrm{o}}, 60^{\mathrm{o}}, 120^{\mathrm{o}}, 180^{\mathrm{o}}, 240^{\mathrm{o}}, 300^{\mathrm{o}}$ (the six acoustic wave directions). The drive equations have a free parameter $\mathcal{S}$ (for *split*), which corresponds to the distribution of chirps between AODs 1,3,5 and AODs 2,4,6 when $s \ll z_{\mathrm{AOL}}$; a 6-AOD AOL can be thought of as two 3-AOD AOLs (discussed in Section 8.2.3). The interpretation of three particular values of $\mathcal{S}$ are as follows: 0 corresponds to putting the linear chirps on only AODs 1,3,5; $2/3 z_{\mathrm{AOL}}$ corresponds to putting the chirps on AODs 2,4,6; and $1/3 z_{\mathrm{AOL}}$ splits the chirps evenly. Without further modelling or experiment it is not clear which value of $\mathcal{S}$ is optimal but I choose the symmetric value because intuitively at least sharing the workload makes sense. To be clear on the difference between $\mathcal{S}$ and the pair deflection ratio $\mathcal{R}$, $\mathcal{S}$ applies to the linear chirp coefficients (bs) for the 6-AOD AOL whereas $\mathcal{R}$ applies to the constant coefficients (as) for the 4-AOD AOL. For the 6-AOD AOL there are four degrees of freedom when deciding how to assign the constant coefficients (as) between the six AODs. However there is not an obvious way to characterise these so I have not introduced any notation to describe them. These degrees of freedom would be worthy of further consideration if the 6-AOD AOL proves to have significant benefits over the 4-AOD AOL since the field of view will depend on them.

The drive equations are too long and ungainly to print here so I have put them in Appendix B for the interested reader. The length of the equations makes them impossible to manipulate or understand in any algebraic way. However, both myself and Dr. P. A. Kirkby have independently verified the purely linear chirps calculated using the 6-AOD AOL drive equations produce a stigmatic focus by using numerical ray tracing. See Fig. 8.4(a) for a ray tracing example of stigmatic focusing by a 6-AOD AOL. To compare the expected performance of the 6-AOD AOL with that of the 4-AOD AOL I applied the ray-based model from Section 4.1. The simulated field of views (full-frame pointing mode, linear drives) are shown in Fig. 8.4(b) and are very comparable for the two designs. However, due to the aberration correction potential, the 6-AOD AOL would be expected to have better axial range performance.

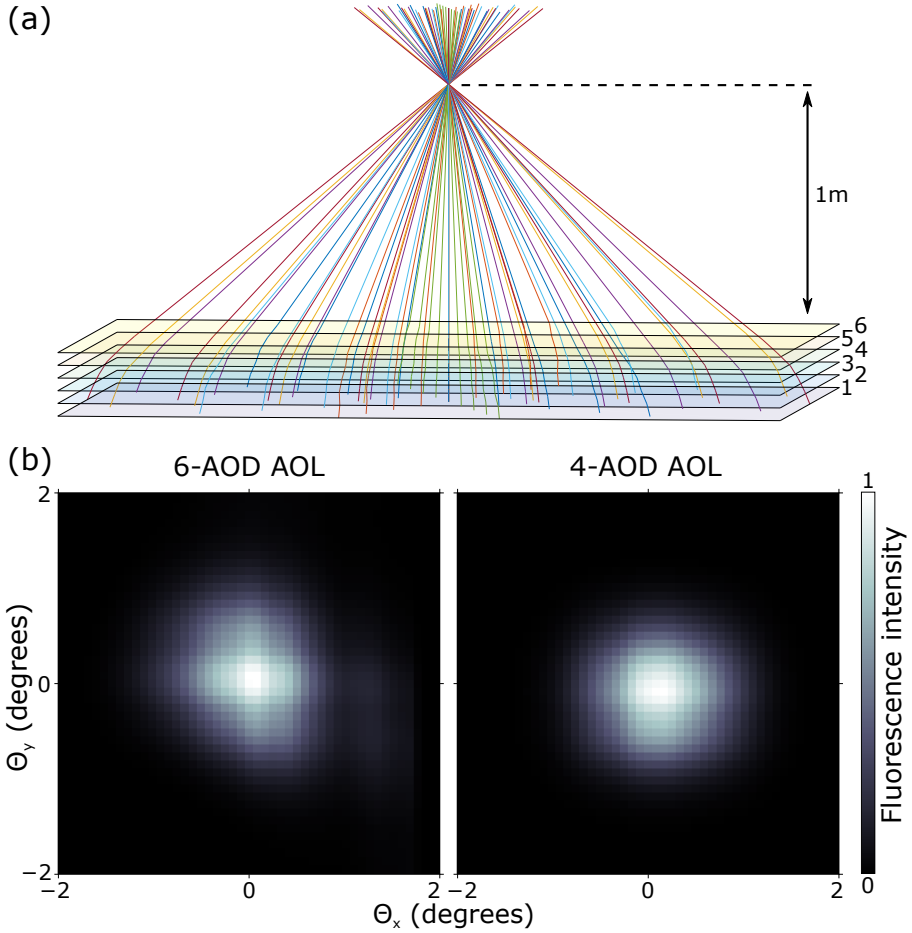

Figure 8.4: (a) Ray tracing showing stigmatic focusing by a 6-AOD AOL using the 6-AOL AOL drive equations I have derived. (b) Field of view comparison in full-frame pointing mode for a 6-AOD AOL (left) and a 4-AOD AOL with $\mathcal{R} = 1$ (right).

8.3 DISCUSSION

I have developed an FFT-based AOL model to predict PSFs and enable me to explore the addition (or correction) of aberrations. I estimate that up to 4 waves of spherical aberration correction is needed for remote focusing, over an axial range of ±150 μm with an idealized 20× water-immersion objective lens. Experimental results with cylindrical AOLs [3] and my model of aberration correction with spherical AOLs suggest that AOL-based wavefront shaping could be used to improve the spatial resolution of 3D AOL microscopy. Although a 4-AOD AOL cannot fully correct for spherical aberrations due to the required cross-terms, the partial correction that can be achieved reduces the focus-dependent axial extension of the two-photon profile by 50%. At ±150 μm, this means the FWHM is reduced from 7 to 4.5 μm, keeping the axial FWHM between 3–4.5 μm over a 300 μm axial range. Given that small neurons have cell bodies of ∼10 μm diameter, the reduction in axial two-photon PSF using a 4-AOD AOL will reduce fluorescence contamination from tissue above and below the region of interest.

In addition to correcting a particular amount of spherical aberration, the 6-AOD AOL also adds unwanted curvature which grows as $O\left(t^2\right)$, analogous to the last row of Table 6.1. The problem here is that the amount of spherical aberration introduced by the objective changes with focal length and therefore the defocusing will progressively spoil the correction. This imposes a limit on how long spherical aberration is effective for or rather the focal position motion must be allowed for. My simulations suggest that the aberration correction is of good quality for around 10 μs but the focal position moves significantly. This suggests curved scans will need to be used for spherical aberration-compensated imaging. In addition to spherical aberration, the first eight Zernike modes can be compensated by a 6-AOD AOL, the last two for brief durations and the first six for entire frequency ramps.

The theory in [3] assumed zero separation between AODs. The experiments and the simulations of [3] have not explored the issue of AOD spacing, and do not add curvature with the AODs ($b_n = 0$, $n = 1, 2, 3, 4, 5, 6$). Simulations which take the spacing between AODs to be 5 cm reveal that aberration correction is still good but imperfect. The separation can be partially accounted for by scaling the cubic chirps with distance as suggested by Dr. P. A. Kirkby. I have verified this both through simulations and also theoretically by making the approximation that rays intersection each AOD at the same position which makes the 3D nonlinear problem tractable. With further theoretical work it might be possible to calculate exact relations for the higher-order chirps used for axial scanning and spherical aberration correction. However, I have not found a way to do this. A theoreti-

cally simpler alternative would be to use 4f relays between the AODs (similar to those in Fig. 2.5). Whilst this would introduce new practical challenges, it may be the only way to achieve a good PSF for arbitrary-direction scanning with a 6-AOL AOL.

For practical operation of a compact 6-AOD AOL (non-zero AOD spacing) it is necessary to be able to focus stigmatically over an axial range comparable to a 4-AOD AOL. I have succeeded in deriving the drive equations that account for non-zero AOD spacing for pointing and line-scanning in three specific lateral directions. The reason that the drive equations are much harder to derive for the 6-AOD AOL than the 4-AOD AOL is because the AODs are not orthogonal and therefore the problem is fully 3D. The drive equations are too long to print in this thesis so I have provided a short MATLAB script to generate them in Appendix B. The problems with the drive equations being so long are that they cannot be manipulated by hand and no intuition can be gained from them. An approximate means to extend the drive equations to arbitrary lateral directions is to use linear combinations of the known directions. This was proposed independently by Dr. P. A. Kirkby and Prof. R. A. Silver. I have carried out some limited simulations of doing this and it appears that it works well. Thus, lateral scanning should be possible with a 6-AOD AOL.

In theory, a 6-AOD AOL can correct the first eight Zernike modes and is able to scan at high speed as well as imaging discrete points. A recently proposed arrangement of four AODs oriented in 45^{o} increments (45^{o}-4-AOD) [65] could correct spherical aberration and all but one of the first twelve Zernike modes. It operates by firing a single laser-pulse precisely synchronised with the AOD drive frequencies to avoid the problem of acoustic wave propagation. In Section 9 I further show that the 45^{o}-4-AOD can also theoretically perform high-speed lateral line-scans, which has not been reported in the literature and may have been overlooked. With the extensive theoretical challenges associated with driving a compact 6-AOD AOL, the 45^{o}-4-AODs may turn out to be a more viable option for aberration corrected AOD-based imaging. However, the 45^{o}-4-AOD lacks the ability to perform high-speed axial scanning because the AODs are not arranged to generate pairs of counter-propagating acoustic waves. For the same reason, the 45^{o}-4-AOD would not be able to perform any aberration correction whilst line-scanning. In contrast, Dr. P. A. Kirkby has proposed that a 6-AOD AOL could perform spherical aberration-corrected axial line-scans by using a combination of fifth-order frequency coefficients e and third-order coefficients c, and empirical simulations I have performed assuming zero AOD spacing support this. However, how to adjust frequency coefficients to account for non-zero AOD spacing in a compact 6-AOD AOL may require further theoretical progress if the PSF produced by a 6-AOD AOL using nonlinear drives is to be of sufficiently high quality.

9 ALTERNATIVE AOL DESIGNS

Whilst the compact AOL design can conveniently be inserted into existing microscopes without difficulty, it does have drawbacks compared to the single-relay design (see Fig. 2.5). The main limitations of the compact design are transmission efficiency and ease of assembly, both because of the need for polarisers to filter unwanted diffraction modes after each AOD. There is the additional challenge of increased drive equation complexity, although this problem has been solved to a large extent. I propose two novel AOL designs which are variants of the single-relay design, and detail how the 45°-4-AOD could perform continuous straight-line scans.

9.1 DIFFERENT ACOUSTIC VELOCITIES: INDEFINITE POINTING

In Chapter 6 I showed that maintaining a focus indefinitely is impossible with an AOL (except when driven with constant frequencies). To remind the reader, at the end of every AOD frequency drive ramp the AOL must be idle for the AOD fill time of approximately 25 μs to allow new ramps to propagate across the AODs. This leads to a low duty cycle for pointing mode and short line-scans. Here I describe a modified AOL design which is theoretically interesting on the grounds that it can focus on a fixed point in 3D space indefinitely. Contrast this with existing AOL designs for which focal spots exist for at most several microseconds when the AOL adds a large amount of curvature to the optical beam.

A stationary focal position can in principle be achieved by having co-propagating acoustic waves (same direction), as opposed to counter-propagating. This only works when the acoustic velocities are different. The linear drive equations for a cylindrical AOL generalised to allow different acoustic velocities between the two AODs are

$$\begin{aligned} b_1 &= \frac{V_1^2}{\lambda} \frac{V_2 + v}{z_{\mathrm{AOL}} (V_1 + V_2) + s (v + V_2)} \\ b_2 &= \frac{V_2^2}{\lambda} \frac{V_1 - v}{z_{\mathrm{AOL}} (V_1 + V_2)} \end{aligned} \tag{9.1}$$

In the case of counter-propagating acoustic waves $V_1 = -V_2$, Eq. (2.6) is recovered. Also note, $V_1 = V_2$ leads to a divide-by-zero issue, which is why counter-propagating acoustic waves have been used in AOLs. However, there is no problem with co-propagating waves providing

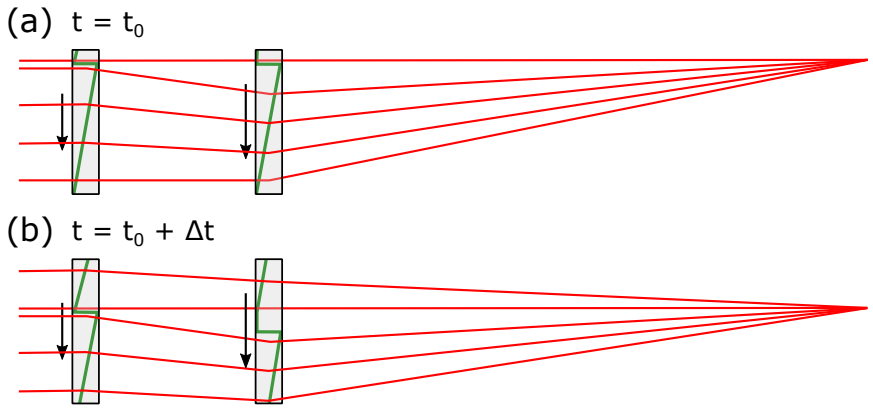

Figure 9.1: Quasi-continuously-operating AOL. Co-ordinated frequency jumps are used to enable the AOL to maintain a stigmatic focus over multiple ramps. (a) The rays (red) passing through a particular frequency ramp (green) on the first AOD are projected onto a smaller area the second AOD, all passing through the same ramp. This means there is a gap between the rays on the second AOD rays from different ramps on the first AOD. At $t = t_0$ the ramp edges are at the top of the AODs and the ray gap is at the top of the second AOD. (b) After some time Δt has passed, the ray gap progressively moves across the ramp edge on the second AOD, as can be seen. In this figure, the acoustic wave propagates faster across the second than the first. The ramps are synchronised between the AODs and the ramp on the second AOD is necessarily longer for this to be possible. By the time the ramp reaches the bottom of the second AOD it has caught up with the bottom of the ray gap. This way, rays are kept to matched ramps on the first and second AODs and imaging can be indefinite.

$V_1 \neq V_2$. It is not practically desirable to have to use different AOD crystal materials or transducer orientations to achieve $V_1 \neq V_2$. Fortunately, an optical trick can be used to make equal acoustic velocities appear to be different: a magnifying 4f relay can be used between the AODs. Since the single-relay design is already common, it should be trivial to adapt the designs to use magnifying relays.

The use of counter-propagating acoustic waves in an AOL mean a stigmatic focus is only possible when a single acoustic frequency ramp is present across each AOD aperture. However, when the acoustic waves are co-propagating with different speeds, consecutive ramps do not necessarily destroy the stigmatic focus because the new ramps both start on the same side as illustrated in Fig. 9.1. Therefore, the focal trajectory can be maintained over multiple frequency ramps. A key idea is that rays from each ramp across the first AOD are mapped to a smaller area on the second AOD, which are covered by single ramps. An implied limitation is that the first AOD must produce a convergent beam, which restricts the sign of its linear chirp. This means the modified design would have a more limited axial range than the conventional AOL. Furthermore, this modified cylindrical AOL falls short of indefinitely scanning any trajectory of interest, which is the ultimate goal.

An interesting theoretical point raised here is that an AOL has traditionally been considered to need counter-propagating acoustic waves. However, it is not so important that the acoustic waves are counter-propagating so much as they have different velocities (equal and opposite in the conventional case). Exploring this idea further leads to the conclusion that a cylindrical AOL comprising three AODs with different acoustic velocities could perform aberration-free laterally-accelerating scans (compare with Table 6.1). Going further, a cylindrical AOL comprising four AODs with four different acoustic velocities could perform spherical-like aberration correction without introducing axial acceleration or, conversely, aberration-free axial-accelerating scans. Because adding extra AODs comes at a high price, both literally and in terms of reduced transmission efficiency, the ideas expressed in this paragraph are unlikely to be of much practical benefit.

9.2 MULTI-PASS AOD AXIAL SCANNER

Two-photon microscopes are found only in larger well-funded labs due to their high price. The availability of AOL microscopes will therefore be further limited, possibly restricted to labs with significant optics expertise. The headline advantage of an AOL is the fast and precise control of focal position in 3D space. Galvos provide an affordable means of performing fast 2D scanning. I therefore propose an affordable AOD-based unit that controls focal length, which could be combined with galvos for fast 3D focal position control.

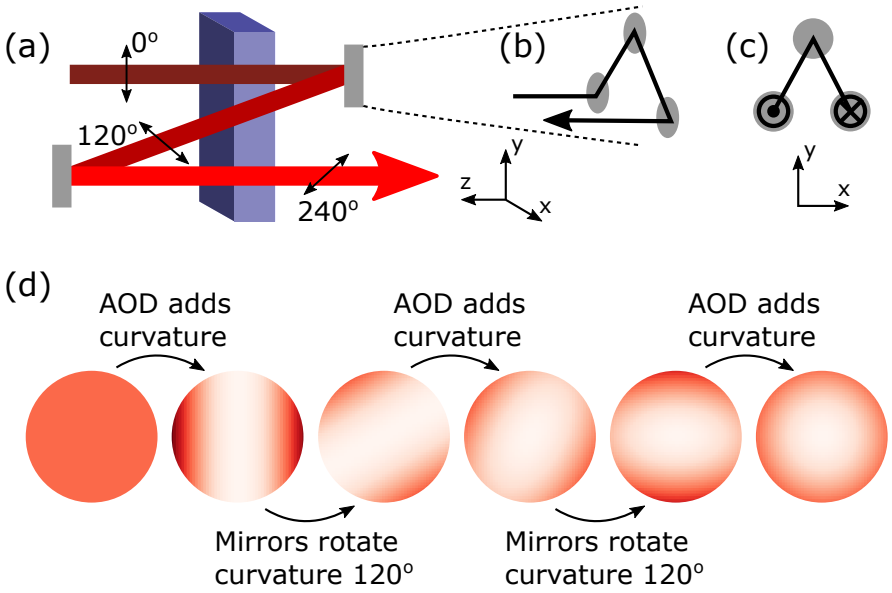

Figure 9.2: A single-AOD axial-scanning unit. (a) An optical beam is passed through the same AOD three times. It is twice reflected by mirror-triplets which rotate the curvature by 120°. These mirror triplets are shown side-on in (b) and front-on in (c). (d) The curvature evolves with each AOD-pass and each mirror-triplet reflection. The six key stages are shown going from a flat wavefront to a parabolic wavefront.

A single AOD could be used to jump rapidly and discretely between focal planes, whilst correcting for spherical aberration. The basis of using a single AOD is that an optical beam must be passed through the single AOD multiple times. This is shown in Fig. 9.2(a). Between each pass, the curvature of the beam must be relayed and rotated, which is possible using an appropriate arrangement of lenses and mirrors. The rotation of the curvature is achieved using mirror-triplets as shown side-on in Fig. 9.2(b) and face-on in Fig. 9.2(c). The evolution of the curvature as it passes through the single-AOD system is depicted in Fig. 9.2(d).

Three is the least number of passes required for an AOD to emulate a spherical lens. Triple-passing means there are effectively three AODs, despite there only being one physically present. The theory for stationary focusing using a 3-AOD AOL was detailed in Section 8.2.3. Taking AOD separation to be zero ($s = 0$), the drive equations were given by Eq. (8.13). It is a prerequisite that the frequency drives are the same on each of the three AODs for the 3-AOD AOL because the proposed implementation only has a single AOD used to diffract the optical beam trice. Spherical aberration can be controlled using the cubic chirp coefficient d. Thus, a single AOD should be capable of shifting the axial focal position at 30 kHz over a 2 mm range with a 20× objective, without introducing spherical aberration.

A triple-passed AOD can jump discretely between focal planes but would be unable to offer high-speed axial scanning. A 4-pass AOD (90° rotations of curvature between passes) is able to perform high-speed axial scanning but not spherical aberration correction. As may be expected, a 6-pass AOD (60° rotations of curvature between passes) would be able to perform both high-speed axial scanning and spherical aberration correction. Doubtlessly this many passes would pose quite a practical challenge. Alternatively a double pass through an orthogonal pair of AODs provides all the functionality of a 4-pass single AOD: doubling the number of AODs halves the number of passes.

A multi-pass axial scanner would have inferior functionality compared to an AOL (no lateral scanning; only axial). It would, however, be simpler and cheaper (due to fewer AODs). It may even be straightforward to multiplex axial scanners to achieve a 100% duty cycle. I propose the idea on the grounds that such an axial scanner would be an affordable upgrade for many existing galvo-based two-photon microscopes which have fast lateral scanning but only slow axial scanning using (for example) a piezo-mounted objective.

9.3 LINE-SCANNING WITH 45°-4-AOD

Here I propose how a 45°-4-AOD can perform high-speed lateral line-scanning. Recall that this system could control the first 14 Zernike modes when operated with single-laser-pulse strobing. Additionally, this arrangement of AODs is also theoretically capable of high-speed scanning in lateral directions, which has not been recognised in the literature. I give an outline of this now. The AODs can be taken to have zero spacing, aided by the use of a 4f relay. For linear frequency chirps, the AOD ray profile shifts (which are proportional to the acoustic phases, see Section 6.2) can be written as

$$\begin{aligned} \Gamma_1 &= B_1(Vt-x)^2 \quad , \qquad \Gamma_2 = B_2\left(Vt-\frac{y+x}{\sqrt{2}}\right)^2 \\ \Gamma_3 &= B_3(Vt-y)^2 \quad , \qquad \Gamma_4 = B_4\left(Vt-\frac{y-x}{\sqrt{2}}\right)^2 \end{aligned} \tag{9.2}$$

Combining AODs 1,3 and 2,4 and taking $B_1 = B_3$ and $B_2 = B_4$ yields the following relations

$$\begin{aligned} \Gamma_1+\Gamma_3 &= B_1\left(x^2+y^2\right) - 2B_1Vt(x+y) \\ \Gamma_2+\Gamma_4 &= B_2(x^2+y^2) - 2\sqrt{2}B_2Vty \end{aligned} \tag{9.3}$$

These two combinations both correspond to stigmatic foci moving with constant velocities. This is because the AODs in each pair are at

right-angles to each other. The resultant wavefront from combining these two orthogonal pairs is

$$\begin{aligned}\Gamma_1+\Gamma_3+\Gamma_2+\Gamma_4 &= (B_1+B_2)\left(x^2+y^2\right)- \\ &\quad 2Vt\left(B_1x+\left[B_1+\sqrt{2}B_2\right]y\right)\end{aligned} \tag{9.4}$$

There are three quantities of interest here: focal length $1/2\,(B_1+B_2)$, lateral scan speed $V\left(B_1^2+\left[B_1+\sqrt{2}B_2\right]^2\right)^{1/2}/\,(B_1+B_2)$ and the scan direction. In practice it will be the focal length and scan speed that are specified since the orientation of lateral scans do not particularly matter when imaging a plane. The useful application of this is that full-frame line-scanning mode imaging of a 3D biological structure could be performed to identify regions of interest. Regions of interest would be subsequently imaged in multi-point mode, augmented with aberration correction for high-resolution functional imaging. The ability to perform high-speed scanning opens up the possibility of implementing real-time movement correction in the same way as for an AOL microscope. A complication is that the laser input would have to be readily swapped between 80 MHz for scanning and 80 kHz for strobing but this should not be a major challenge, for example using a Pockels cell.

A fundamental limitation of this arrangement is the scanning speed has a lower limit of $1.3V$. If a lower limit on dwell time is set at 50 ns, the shortest focal length possible for a 512×512 image over a 40 mrad field of view with $V=613$ m/s is 0.5 m. With the optical arrangement of the compact AOL microscope, 0.5 m focal length corresponds to an axial range of over 500 μm , which is unlikely to be a practical limitation. At any rate, the focal scan speed in the front focal plane of the objective can be set arbitrarily and this is likely to be the most commonly imaged plane. Thus, by combining the single-pulse strobing with AOL-like high-speed scanning, the 45°-4-AOD should be able to perform high-speed full-frame line-scanning imaging as well as aberration-corrected multi-point imaging, both with movement correction.

9.4 SPHERICAL ABERRATION-CORRECTING OPTICS

It would be ideal if the spherical aberration arising from remote focusing could be corrected using fixed optical components. Here I propose an optical system using only four lenses: two standard achromatic lenses of equal focal length and two specially-designed lenses that introduce quartic phase shifts instead of parabolic phase shifts. The two standard lenses are arranged as a unit magnification 4f optical system and the special lenses are placed in between these as shown in Fig. 9.3. The first special lens adds spherical aberration via

a positive phase shift which grows with the fourth power of radius ($\phi = r^4$). The second special lens subtracts spherical aberration via a negative phase shift which grows with the fourth power of radius ($\phi = -r^4$).

When a planar wavefront is incident on the system, the beam is focussed down symmetrically around the centre of the 4f system such that the quartic phase shifts introduced by special lenses are equal and opposite, and cancel each other out. When a positively/negatively curved wavefront is incident, the focus moves forwards/backwards from the centre of the 4f system. This means that the quartic phase shifts introduced are no longer equal and do not cancel out, leaving positive/negative residual spherical aberration. By positioning the special lenses at the right distance (to be determined either theoretically or empirically) from the centre of the 4f system and the right way around, the net spherical aberration introduced for a given focus should be able to balance out with the spherical aberration introduced by remote focusing.

This optical arrangement has the potential to remove one of the major limitations of many remote focusing microscopes. The major hurdle will be acquiring the special optical elements, which are non-standard. Further theory for the magnitude of the quartic phases that need to be introduced for typical remote-focusing microscope operation (and for the chosen focal lengths of the standard lenses) would be useful prior to experimentation. However, I believe lateral deflections would cause this system to fail and therefore I do not expect it to work with an AOL, in which lateral and axial control cannot be separated.

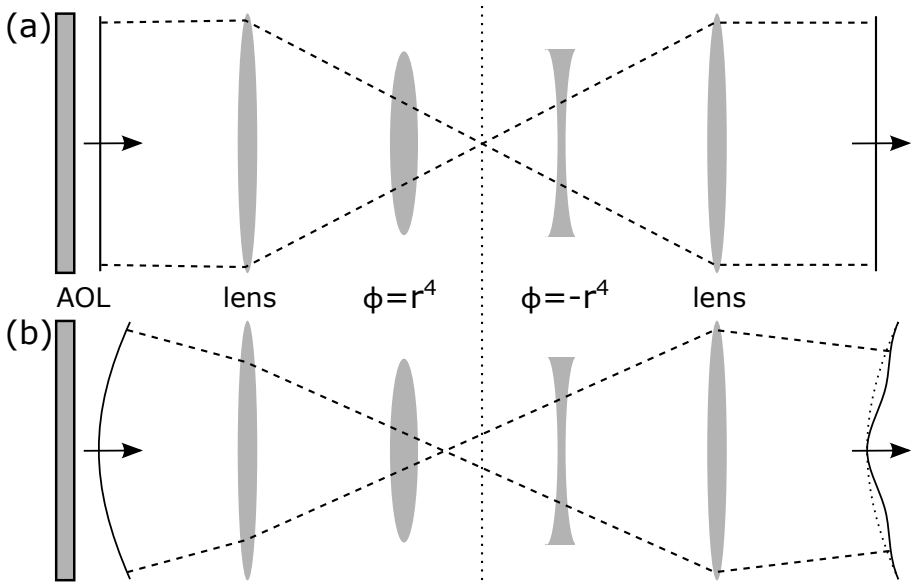

Figure 9.3: Correcting spherical aberration using a fixed optical arrangement following the AOL. A 4f system is used with two additional special lenses introducing quartic phase shifts ($\phi = \pm r^4$) placed in-between the two lenses, equidistant from the middle. (a) A planar wavefront passes through gaining and losing equal amounts of spherical aberration at the special elements. (b) A curved wavefront focuses off-centre such that it is larger at one of the special elements than the other. Thus, net spherical aberration is present in the outgoing wavefront.

10

SUMMARY DISCUSSION

The progress described within this thesis has introduced new AOL microscope features and mitigated several limitations. Here I outline the most significant of these and highlight some of the wider implications. I have found an AOL microscope can image over a field of view within a factor of two of a galvo system [75, 76] by using the optimal drive frequency ramps and matching transducer width to available acoustic drive powers. Transmission efficiency can be made near-uniform across a 350 μm field of view (20$\times$ objective) by modulation of acoustic drive amplitude (power). However, since laser power has to be lost in the middle of the field of view to achieve this, I found the signal to noise was too poor in biological samples currently to demonstrate the benefits. I have advanced nonlinear drive theory for AOLs by developing new geometrical optics theory. I have applied the theory to derive new nonlinear drive equations for a 4-AOD AOL, which remove the zero-AOD-spacing approximation needed in existing theory. By developing software specially for the purpose, I have demonstrated arbitrary-direction line-scans and curved-scans. In particular, I have demonstrated three nonlinear imaging modes (arbitrary-plane, curved-surface, glove) with a 4-AOD AOL for the first time. I have derived the 6-AOD AOL linear drive equations, needed for basic AOL operation. This is promising because my simulations indicate that a 6-AOD AOL can near-perfectly correct the spherical aberration that arises due to remote focusing by using nonlinear drives. Furthermore, simulations indicate a 4-AOD AOL can partially-correct spherical aberration to a useful extent.

I have made progress by developing a range of models, which I have corroborated with experimental measurements. The models I have developed can be separated into phase (determining drive frequencies, linear and nonlinear) and amplitude (predicting AOL transmission efficiency). Analytic phase models include the recursive ray equation of Chapter 3 (linear and nonlinear drives, any number of AODs and orientations but difficult to solve except for linearly-driven cylindrical AOL), ray-profile Taylor series propagation of Chapter 6 (linear and nonlinear drives for cylindrical and 4-AOD AOL only), and the matrix formalism of Chapter 8 (any number of AODs and orientations but linear drives only; used to derive 6-AOD AOL drive equations). To explore the results I derived from the analytic models in more detail, I developed numerical FFT-based phase models in 2D (cylindrical AOL only; Chapter 6) and 3D (any number of AODs and orientations, includes chromatic effects, but slower or lower res-

olution than 2D; Chapter 8). A large effort went towards developing the first AOL transmission efficiency model, which was the subject of Chapter 4 and used to explore the effect of pair deflection ratio ($\mathcal{R}$) in Chapter 3. I applied an analytic model of a single-AOD to explore the prospective benefits of acoustic drive amplitude modulation in Chapter 5.

The field of view of AOL microscopes has been addressed from both the perspective of pair deflection ratio and acoustic drive amplitude modulation. I found the microscope's imaging volume was sensitively dependent on $\mathcal{R}$, with 0.3 being the optimal value for the AOL microscope I used. My ray-based AOL model was able to predict this optimisation and guide the experimental confirmation, greatly easing and expediting development [1]. In the front focal plane of the objective, the AOL microscope's field of view should be the same for full-frame pointing mode with $\mathcal{R} = 1$ as for full-frame line-scanning. In full-frame line-scanning mode, the model found that field of view was poor for long pixel dwell times. This is consistent with the finding that short dwell times are necessary in order to perform full-frame line-scanning far from the front focal plane of the objective [2]. It further predicted that extremely short dwell times lead to decreased transmission efficiency but greater uniformity, and the dwell time should be inversely proportional to axial focal displacement for a consistent field of view. I hope that the transmission efficiency model will enable researchers to further examine the effect of varying AOL design parameters and thereby improve AOL performance.

Acoustic drive amplitude modulation was applied to line-scanning for the first time, and I found that total fluorescence across the field of view could be increased by up to 62% in full-frame line-scanning mode as well as greatly improving the brightness uniformity when ample laser power was available. However, the transmission efficiency of the AOL is reduced significantly by using amplitude modulation because uniformity is achieved by reducing AOD diffraction efficiency where it is naturally highest. Consequently, laser power was insufficient to demonstrate field of view and uniformity improvements for biological samples.

I have refined nonlinear drive theory for the compact (4-AOD) AOL by developing new geometric optics theory that analytically determines the evolution of an optical beam propagating through a uniform refractive index. The evolution of the beam is described in terms of Taylor series coefficients which represent the integral of ray gradients over a line in 2D space. A 3D generalisation is possible but becomes much more challenging to use due to the increase in the number of coefficients. The effect of an AOD on the Taylor series coefficients can be directly related to the drive frequency coefficients $a, b, c, d, \ldots$ enabling me to calculate nonlinear drive equations for arbitrary-direction scanning and curved-scanning with a 4-

AOD AOL. These scan modes form the basis of three new AOL imaging modes (arbitrary-plane, curved-surface, glove) and I have demonstrated all three of these experimentally. Glove mode will likely find the greatest experimental utility: a handful of dendrites can be traced semi-automatically and low-resolution volumetric imaging of them can be performed at hundreds of Hz. This opens the possibility of watching multiple dendrites as well as somata and axons in near-real-time such that local and global excitations could be distinguished in a way not presently possible. I hope that experimentalists will find this useful when examining the response of awake mice to various stimuli.

Following from the nonlinear drive theory I develop, I have shown the low duty-cycle of pointing and short line-scans is an inherent feature of AOLs, which is theoretically unavoidable. To increase the duty cycle, one option would be to run multiple AOLs in parallel such that one is operating whilst the others are ramp-loading. This would require precise synchronisation between AOLs and careful optical alignment to match AOL beam paths into the objective, which should be feasible. However, this would involve a total of eight AODs, which makes it a very expensive solution and therefore it is worth looking for alternatives. It may be possible to alter the design of an AOL subtly to improve the duty cycle but this is an open question for the future. I proposed an idea that goes some way to removing the AOD acoustic fill time requirement of existing AOLs in Section 9.1 but this has its own short-comings and doesn't overcome pointing and short line-scan duty cycle limitations.

The goal of implementing spherical aberration correction in an AOL has been closely tied with the development of a 6-AOD AOL. I have made progress on this, deriving the drive equations necessary for a compact 6-AOD AOL using a general procedure I developed in Section 8.2 for linear chirps. This general approach will enable the capabilities of new AOL designs featuring non-orthogonal AOD arrangements to be evaluated systematically. However, the calculation of nonlinear frequency ramps still relies on approximating AOD spacing as zero. Simulations of nonlinear frequency drives empirically suggest that cubic frequency chirps can be scaled according to AOD spacing to improve the effectiveness of the spherical aberration correction. Even so, a complete theoretical approach to fast axial line-scanning with a 6-AOD AOL needs to be found if it is to be on a par with the 4-AOD AOL. Alternatively, a non-compact design of 6-AOD AOL can be considered which uses 4f systems between the AODs to make the AOD spacing effectively zero. Then the results in Table 6.1 would involve no approximation and should be capable of producing diffraction limited PSFs. A challenger technology, the 45°-4-AOD promises a greater number of correctable Zernike modes with two fewer AODs. Additionally, in Section 9.3 I show how the 45°-4-AOD

can perform high-speed lateral scanning. However, the 6-AOD AOL has two big prospective advantages: axial scanning and aberration-corrected line-scanning.

I expect future AOL microscope development to take three paths. Firstly, developing software: increasing maximum acquisition speeds, building new tools for analysis and making the microscope easier to use. Secondly, exploring variants of the conventional 4-AOD AOL: experimenting with the 6-AOD AOL and other possibilities, some of which I suggest in Section 9. Thirdly and more speculatively, exploring more intricate amplitude modulation: putting multiple frequencies across an AOD concurrently is equivalent to amplitude modulation because of the interference beat patterns. Such amplitude modulation opens the possibility of splitting the optical beam into multiple sub-beams to form 3D point lattices. Alternatively, amplitude modulation could be used to reduce optical beam width and therefore increase the size of the microscope PSF. Both of these may find applications for uncaging and photo-stimulation.

Future modelling will presumably focus on diffraction efficiency dependence on amplitude and unifying amplitude and phase models. The ray-based numerical model of Chapter 4 has been successful at calculating AOL transmission efficiencies when supplemented with a handful of experimental measurements. The main limitation is that it cannot infer PSFs. Conversely, the FFT model of Chapter 8 is able to calculate PSFs but is not able to compute the transmission efficiency of the AOL. Therefore, if these models were unified in a satisfactory manner, the resulting model would be able to comprehensively predict AOL microscope performance. One manner to proceed would be to use the FFT model between the AODs and from the last AOD to the focal volume. The propagation through the AODs would be handled by the ray model. To do this, the incident optical field would be approximated by a bundle of rays, propagated by the ray model, and synthesised back into a field again. One question such a model would be able to address is how detected fluorescence intensity from a uniform sample should depend on axial position, since this depends on both the transmission efficiency due to frequency ramp gradient and PSF degradation due to spherical aberration.

To conclude, AOL microscopes in their current state of development offer functional imaging modes that are unavailable with competing technologies: glove mode and random-access pointing can be performed at unparalleled speeds with real-time movement correction. In addition to having unique capabilities, AOL microscopy provides high-duty-cycle full-frame line-scanning for fast 3D structural imaging and more specialized imaging modes such as large-scale mosaic imaging of an entire mouse brain slice. Further to this, AOL microscopes remain to be applied to uncaging and photo-stimulation, which have the potential to significantly extend their advantages over

competing microscope technologies. It is beyond doubt that AOL microscopes will enable new ways of directly observing spatially-dispersed neuronal activity in 3D. Therefore, I believe AOL microscope technology has reached the stage when it should be disseminated to other neuroscience labs. If this is successful, the challenge will be for neuroscientists to translate microscope data into a greater understanding of neural circuits and their distributed processing of sensory information.

Part III

APPENDIX

A

GEOMETRIC DERIVATION OF AOL DRIVE EQUATIONS

The original derivation of the drive equations for a compact cylindrical AOL followed a geometrical ray argument [61] reproduced here because it is a cornerstone of the thesis. I begin by solving for a stationary focus before solving for a moving focus.

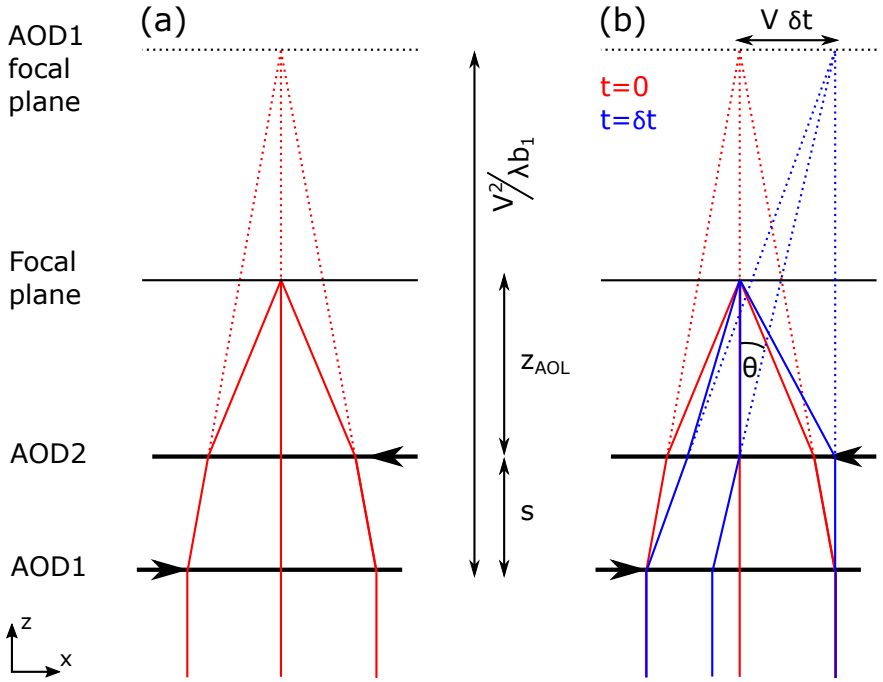

Figure A.1: Geometrical derivation of drive equations for a cylindrical AOL: collimated light is focused by two AODs with counter-propagating acoustic waves. The dashed lines show the path the rays would take in the absence of the second AOD. The distance between the AODs is s, the distance from the second AOD to the focus is z_{AOL}. The distance from the first AOD to where the focus would be if the second AOD wasn't there is $V^2/\lambda b_1$. (a) Ray paths at one instant of time. (b) Red rays as in (a) with blue rays showing the path taken a short time after the red rays. The path is time-dependent because the acoustic waves propagate across the AOD.

A.1 STATIONARY FOCUS

With reference to Fig. A.1(a), the acoustic frequencies F_+ and F_- across the first and second AODs respectively are given by

$$F_\pm = a_\pm + b_\pm \left(t \mp \frac{x}{V} \right) \tag{A.1}$$

As explained in Section 2.5.2, the focal lengths of the AODs are determined by the strength of the acoustic frequency chirps $b_\pm$. In order to focus at an axial displacement of f from the second AOD then, we can apply the *thin lens equation [109]*,

$$\frac{1}{f_+ - s} + \frac{1}{f_-} = \frac{1}{z_{\text{AOL}}} \tag{A.2}$$

with Eq. (2.5) to arrive at the first constraint, which determines the focal length. Assuming the AODs are operating in the $+1$ diffraction mode:

$$\frac{\lambda b_-}{V^2} = \frac{-1}{V^2/\lambda b_+ - s} + \frac{1}{z_{\text{AOL}}} \tag{A.3}$$

Now I derive the second constraint, to ensure the focal position is stationary. Examine Fig. A.1(b): the effective focal position of the first AOD will be moving laterally with velocity V. The second AOD, at the origin, must add additional deflection $\delta\theta$ in order to keep the resultant focus stationary. Adding angular deflection of $\delta\theta$ corresponds to a frequency shift δF_- at the second AOD:

$$\delta\theta = \frac{\lambda \delta F_-}{V} = \frac{\lambda b_- \delta t}{V} \tag{A.4}$$

A second relation holds for $\delta\theta$ by applying trigonometry to Fig. A.1(b) and applying small-angle approximations:

$$\delta\theta = \frac{V \delta t}{V^2/\lambda b_+ - s} \tag{A.5}$$

Equating Eqs. (A.4) and (A.5) leads to the second constraint to ensure the focus is stationary:

$$\frac{\lambda b_-}{V^2} = \frac{1}{V^2/\lambda b_+ - s} \tag{A.6}$$

Solving the two constraints, Eqs. (A.3) and (A.6), leads to unique chirps for a stationary focus:

$$b_+^{\text{stat}} = \frac{V^2}{\lambda} \frac{1}{2z_{\text{AOL}} + s}, \quad b_-^{\text{stat}} = \frac{V^2}{\lambda} \frac{1}{2z_{\text{AOL}}} \tag{A.7}$$

The $a_\pm$ in A.1 do not affect the focal length but determine the lateral position of the focus. How the $a_\pm$ should be determined is discussed in the results of this thesis (Section 3.1.4) and in [1]. Having arrived at the solution for a stationary focus, I next generalise the derivation to find the solution for a moving focus.

A.2 MOVING FOCUS

A single AOD drive with a linearly-chirped acoustic frequency produces a focus moving with the acoustic propagation speed V in the same direction as the acoustic wave (Section 2.3.1). A cylindrical AOL can produce a focal position that moves with any lateral velocity. To derive the linear chirps for this, it is only necessary to adjust Eq. (A.6). The angular deflection $\delta\theta$ must under/over compensate to achieve positive/negative scan velocity. By re-examining Fig. A.1(b), to achieve a lateral focus velocity of v I replace Eq. (A.5) with

$$\delta\theta = \frac{V\delta t}{V^2/\lambda b_+ - s} - \frac{v\delta t}{z_{\mathrm{AOL}}} \tag{A.8}$$

Equating Eqs. (A.8) and (A.5) yields the scanning-adjusted version of Eq. (A.6):

$$\frac{\lambda b_-}{V^2} = \frac{1}{V^2/\lambda b_+ - s} - \frac{v}{V z_{\mathrm{AOL}}} \tag{A.9}$$

To find drive equations for $b_\pm$, I solve Eqs. (A.3) and (A.9) simultaneously to arrive at Eq. (2.6). Notice b^{stat} can be recovered by setting $v = 0$. This concludes the geometric derivation of drive equations for a cylindrical AOL as found in [61].

B

DRIVE EQUATIONS FOR 6-AOD-AOL

The drive equations for the 6-AOD AOL span over 14 pages in this font, making it impractical (and somewhat pointless) to print them here. The interested reader can generate the drive equations for themselves using the short MATLAB script included in Listing B.1. Excluding white-space and comments, only 28 lines of MATLAB code are needed to calculate the 6-AOD AOL drive equations.

The script returns two possible sets of drive equations. However, ray-tracing simulations indicated that one set could be discarded on the basis that the rays took undesirable paths. Note that matrices M and D in the code below are analogous to the first and second line of the right-hand side of Eq. (8.11) respectively. Units are assumed to be SI except the focal speed v is in multiples of the acoustic velocity V and the drive equations need to by scaled by V^2/λ. The script has been tested in MATLAB R2013a.

Listing B.1: MATLAB script to calculate 6-AOD AOL drive equations.

```
syms c1 c2 c3 c4 c5 c6 f v % declare six linear
% chirps c1-c6, the focal length f, and the focal
% scan speed v (in multiples of acoustic velocity)

s = 5e-2; % spacing between AODs
velocity_unit_vector = [1;0]; % focus moves in x-direction
% also works for 0.5*[-1, sqrt(3)] and 0.5*[-1, -sqrt(3)]

% set up some matrices for later use
I2 = sym(eye(2));
I4 = sym(eye(4));
C = cos(sym(2*pi/3));
S = sin(sym(2*pi/3));
R14 = [C*C S*C; C*S S*S];
R25 = [1 0; 0 0];
R36 = [C*C -S*C; -C*S S*S];

Ps = [I2 I2*s;zeros(2) I2]; % propagate between AODs
Pf = [I2 I2*f;zeros(2) I2]; % propagate to focus

% diffract at each AOD, taking acoustic directions to be
% [1 0], -[C S], [C -S], -[1 0], [C S], -[C -S]
Q1 = [I2 zeros(2); -c1*R14 I2];
Q2 = [I2 zeros(2); -c2*R25 I2];
Q3 = [I2 zeros(2); -c3*R36 I2];
Q4 = [I2 zeros(2); -c4*R14 I2];
Q5 = [I2 zeros(2); -c5*R25 I2];
Q6 = [I2 zeros(2); -c6*R36 I2];

% compute matrix 'M' to contrain for stigmatic focus
M = Pf*Q6*Ps*Q5*Ps*Q4*Ps*Q3*Ps*Q2*Ps*Q1;

% compute matrix 'D' to constrain for focus velocity
D14 = Pf*Q6*Ps*Q5*Ps*(Q4*Ps*Q3*Ps*Q2*Ps*c1-I4*c4);
D25 = Pf*Q6*Ps*(Q5*Ps*Q4*Ps*Q3*Ps*c2-I4*c5);
D36 = Pf*(Q6*Ps*Q5*Ps*Q4*Ps*c3-I4*c6);
D36q = D36(1:2,3:4) * [C;-S];
D25q = D25(1:2,3:4) * -[1;0];
D14q = D14(1:2,3:4) * [C;S];
D = D36q + D14q + D25q - v * velocity_unit_vector;

% bundle constrained expressions and solve computationally
eqs = [M(1:2,1:2), D];
drive_eqs = solve(eqs(:),'c1','c2','c3','c4','c5','c6');
% multiply drive_eqs by V^2/lambda to be in SI units
```

C

DERIVATION OF RAY-PROFILE RELATIONS

The MATLAB code in Listing C.1 generates the Taylor coefficient relations stated in Eq. (6.9) for propagating ray-profiles.

Listing C.1: MATLAB script to calculate ray-profile Taylor expansion coefficient relations.

```
% declare Taylor coefficients up to fifth order (y1-5) with
% lateral position x in start plane and propagation distance tau
syms y1 y2 y3 y4 y5 x tau

% define phase profile in start plane as Taylor ex_endansion
y = y1*x + y2*x^2/2 + y3*x^3/6 + y4*x^4/24 + y5*x^5/120;

x_end = x - diff(y)*tau; % relate lateral position
% in end plane to lateral position in start plane

y_end = sym(zeros(5,1));
y_end(1) = diff(y);
y_end(2) = diff(y_end(1))/diff(x_end);
y_end(3) = diff(y_end(2))/diff(x_end);
y_end(4) = diff(y_end(3))/diff(x_end);
y_end(5) = diff(y_end(4))/diff(x_end);

% evaluate end plane phase Taylor coeffs
y_end_0 = simplify(subs(y_end, x, 0));
```

D

MICROSCOPE CONTROL SOFTWARE

In order to implement the nonlinear frequency drive equations from Chapter 7 I wrote new software from scratch with Dr. B. Marin, Dr. G. Konstantinou and Dr. A. Valera. The architecture and design was principally determined by Dr. Marin who solved all the difficult technical challenges, leaving me to write the core of the code. Dr. Konstantinou has provided the knowledge on how to interface with motorised xyz-stage and the mouse-speed-logging wheel. Dr. Valera has extended the code to make it much more useful for biological experiments; he integrated Vaa3D for 3D and time-lapse imaging, and we worked closely together to implement glove mode. In this short Chapter, I outline how the software communicates with the various bits of hardware that make up an AOL microscope.

There are five interfaces used to communicate with the hardware. The xyz-stage is connected via a serial interface, supported natively by MATLAB and therefore easy to work with. The four analogue channels are off a National Instruments board, which is supported directly by MATLAB's Data Acquisition Toolbox, and is also easy to work with. The FPGA which synthesises the frequency ramps (synth FPGA) is designed to send and receive raw ethernet packets. MATLAB's support for raw ethernet didn't appear satisfactory for this purpose so I used WinPcap (on a Windows machine) to communicate with the synth FPGA. The speed-logging mouse-wheel broadcasts data on an IP multicast. Again this could not be set up natively from MATLAB and there was an additional requirement that speed data be acquired asynchronously without blocking the microscope image data acquisition. I therefore wrote a short Java class which spawned a thread to gather data from the wheel.

Finally, the NI FPGA C API was used to communicate the with microscope image data acquisition (DAQ) FPGA at very high speed. I used Peter Fiala's NiFpga Toolbox to auto-generate a working mex file (C code callable from MATLAB). The two channels of image data are stored on the DAQ FPGA in a pair of FIFOs, which can overflow if the PC is not reading data fast enough. To avoid FIFO overflows, I implemented a much large pair of FIFOs in software on the PC. When acquiring an image, a thread continuously reads data from the DAQ FIFOs into the software FIFOs. MATLAB can then read from the software FIFOs less regularly without risking an overflow. This has enabled very high data acquisition speeds of 65 ns/voxel with 28 bits per voxel (two concurrent 14-bit channels).

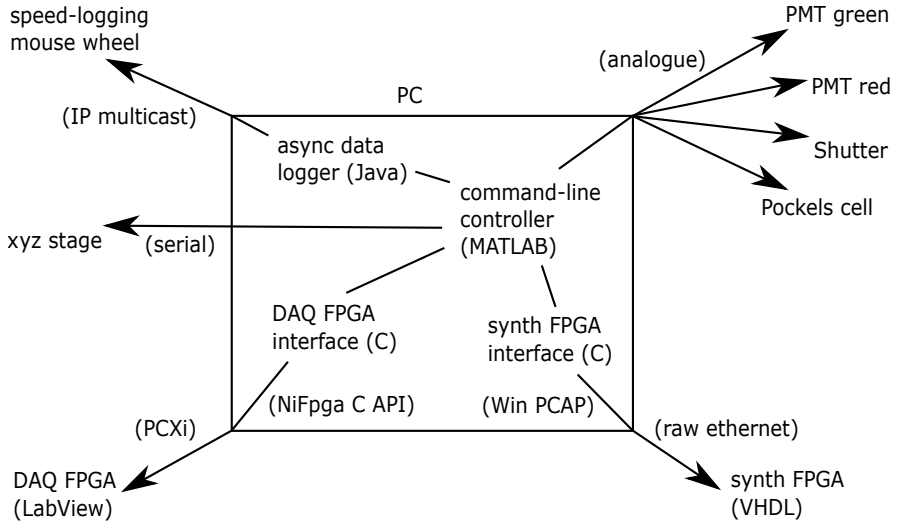

Figure D.1: MATLAB-based microscope controller schematic. Software is shown inside the box labelled PC, and hardware is shown outside. Arrows show software communicating with hardware and the interface technology used is shown in brackets (both inside and outside box). Key software components named and labelled with programming language in brackets.

BIBLIOGRAPHY

[1] Evans, G. J., Kirkby, P. A., Naga Srinivas Nadella, K. M., Marin, B., and Angus Silver, R. "Development and application of a ray-based model of light propagation through a spherical acousto-optic lens." In: *Opt. Express* 23.18 (2015), pp. 23493–510 (cit. on pp. 7, 35, 38–40, 50, 63, 66, 68, 73, 75, 76, 79, 82, 146, 154).

[2] Nadella, K. M. N. S., Roš, H., Baragli, C., Griffiths, V. A., Konstantinou, G., Koimtzis, T., Evans, G. J., Kirkby, P. A., and Silver, R. A. "Random access scanning microscopy for 3D imaging in awake behaving animals." In: *Submitted* (2016) (cit. on pp. 7, 28, 29, 31, 33, 34, 83, 85, 146).

[3] Konstantinou, G., Kirkby, P. A., Evans, G. J., Nadella, N. S., Griffiths, V. A., Mitchell, J. E., and Silver, R. A. "Dynamic wavefront shaping with an acousto-optic lens for laser scanning microscopy." In: *Opt. Express* 24.6 (2016), pp. 201–208 (cit. on pp. 7, 29, 33, 34, 44, 46–48, 52, 97–99, 113, 115, 123–125, 131, 134).

[4] Evans, G. J. *Ray-based AOL model*. 2014. URL: https://github.com/SilverLabUCL/aol_model (cit. on pp. 7, 72, 76).

[5] Evans, G. J. *FFT-based AOL model*. 2016. URL: https://github.com/SilverLabUCL/aol_fft_model (cit. on pp. 7, 124).

[6] Yuste, R. "From the neuron doctrine to neural networks." In: *Nat. Rev. Neurosci.* 16.8 (2015), pp. 487–497 (cit. on pp. 19, 23).

[7] DeFelipe, J. "The dendritic spine story: an intriguing process of discovery." In: *Front. Neuroanat.* 9 (2015), p. 14 (cit. on p. 19).

[8] Grant, G. "How the 1906 Nobel Prize in Physiology or Medicine was shared between Golgi and Cajal." In: *Brain Res. Rev.* 55.2 (2007), pp. 490–8 (cit. on p. 19).

[9] Hodgkin, A. L. and Huxley, A. F. "Action Potentials Recorded from Inside a Nerve Fibre." In: *Nature* 144.3651 (1939), pp. 710–711 (cit. on p. 19).

[10] Hodgkin, A. L. and Huxley, A. F. "A quantitative description of membrane current and its application to conduction and excitation in nerve." In: *J. Physiol.* 117.4 (1952), pp. 500–44 (cit. on p. 19).

[11] Häusser, M. "The Hodgkin-Huxley theory of the action potential." In: *Nat. Neurosci.* 3.Supp (2000), p. 1165 (cit. on p. 19).

[12] Berger, H. "Über das Elektrenkephalogramm des Menschen." In: *Arch. Psychiatr. Nervenkr.* 87.1 (1929), pp. 527–570 (cit. on p. 19).

[13] Tauer, U. "Dynamic Confocal Imaging of Living Brain: Advantages and risks of multiphoton microscopy in physiology." In: *Exp. Physiol.* 87.6.June 2001 (2002), pp. 709–714 (cit. on p. 20).

[14] Minsky, M. "Memoir on inventing the confocal scanning microscope." In: *Scanning* 10.4 (1988), pp. 128–138 (cit. on p. 19).

[15] Wilson, T. and Sheppard, C. *Theory And Practice Of Scanning Optical Microscopy*. 1984 (cit. on p. 19).

[16] Nwaneshiudu, A., Kuschal, C., Sakamoto, F. H., Anderson, R. R., Schwarzenberger, K., and Young, R. C. "Introduction to confocal microscopy." English. In: *J. Invest. Dermatol.* 132.12 (2012), e3 (cit. on p. 19).

[17] Amos, W. B. and White, J. G. "How the confocal laser scanning microscope entered biological research." In: *Biol. Cell* 95.6 (2003), pp. 335–42 (cit. on p. 19).

[18] White, J. G., Amos, W. B., and Fordham, M. "An evaluation of confocal versus conventional imaging of biological structures by fluorescence light microscopy." In: *J. Cell Biol.* 105.1 (1987), pp. 41–8 (cit. on p. 19).

[19] Salzberg, B. M., Davila, H. V., and Cohen, L. B. "Optical Recording of Impulses in Individual Neurones of an Invertebrate Central Nervous System." In: *Nature* 246.5434 (1973), pp. 508–9 (cit. on p. 19).

[20] Baker, B. J., Kosmidis, E. K., Vucinic, D., Falk, C. X., Cohen, L. B., Djurisic, M., and Zecevic, D. "Imaging brain activity with voltage- and calcium-sensitive dyes." In: *Cell. Mol. Neurobiol.* 25.2 (2005), pp. 245–82 (cit. on p. 21).

[21] Tsien, R. Y. "A non-disruptive technique for loading calcium buffers and indicators into cells." In: *Nature* 290.5806 (1981), pp. 527–528 (cit. on p. 21).

[22] Stosiek, C., Garaschuk, O., Holthoff, K., and Konnerth, A. "In vivo two-photon calcium imaging of neuronal networks." In: *Proc. Natl. Acad. Sci. U. S. A.* 100.12 (2003), pp. 7319–24 (cit. on p. 21).

[23] Grienberger, C. and Konnerth, A. "Imaging calcium in neurons." English. In: *Neuron* 73.5 (2012), pp. 862–85 (cit. on p. 21).

[24] Chalfie, M, Tu, Y, Euskirchen, G, Ward, W., and Prasher, D. "Green fluorescent protein as a marker for gene expression." en. In: *Science (80-.).* 263.5148 (1994), pp. 802–805 (cit. on p. 21).

[25] Lois, C., Hong, E. J., Pease, S., Brown, E. J., and Baltimore, D. "Germline transmission and tissue-specific expression of transgenes delivered by lentiviral vectors." en. In: *Science* 295.5556 (2002), pp. 868–72 (cit. on p. 21).

[26] Palikaras, K. and Tavernarakis, N. "Multiphoton Fluorescence Light Microscopy." In: *eLS*. Chichester, UK: John Wiley & Sons, Ltd, 2015, pp. 1–8 (cit. on p. 21).

[27] Denk, W, Strickler, J., and Webb, W. "Two-photon laser scanning fluorescence microscopy." In: *Science (80-.).* 248.4951 (1990), pp. 73–76 (cit. on p. 21).

[28] Zipfel, W. R., Williams, R. M., and Webb, W. W. "Nonlinear magic: multiphoton microscopy in the biosciences." In: *Nat. Biotechnol.* 21.11 (2003), pp. 1369–77 (cit. on p. 22).

[29] Denk, W. "Two-photon excitation in functional biological imaging." In: *J. Biomed. Opt.* 1.3 (1996), p. 296 (cit. on p. 22).

[30] Helmchen, F. and Denk, W. "Deep tissue two-photon microscopy." In: *Nat. Methods* 2.12 (2005), pp. 932–40 (cit. on p. 22).

[31] Lima, S. Q. and Miesenböck, G. "Remote control of behavior through genetically targeted photostimulation of neurons." English. In: *Cell* 121.1 (2005), pp. 141–52 (cit. on p. 22).

[32] Boyden, E. S., Zhang, F., Bamberg, E., Nagel, G., and Deisseroth, K. "Millisecond-timescale, genetically targeted optical control of neural activity." In: *Nat. Neurosci.* 8.9 (2005), pp. 1263–8 (cit. on p. 22).

[33] Li, X., Gutierrez, D. V., Hanson, M. G., Han, J., Mark, M. D., Chiel, H., Hegemann, P., Landmesser, L. T., and Herlitze, S. "Fast noninvasive activation and inhibition of neural and network activity by vertebrate rhodopsin and green algae channelrhodopsin." In: *Proc. Natl. Acad. Sci. U. S. A.* 102.49 (2005), pp. 17816–21 (cit. on p. 22).

[34] Nagel, G., Brauner, M., Liewald, J. F., Adeishvili, N., Bamberg, E., and Gottschalk, A. "Light activation of channelrhodopsin-2 in excitable cells of Caenorhabditis elegans triggers rapid behavioral responses." English. In: *Curr. Biol.* 15.24 (2005), pp. 2279–84 (cit. on p. 22).

[35] Lin, J. Y. "A user's guide to channelrhodopsin variants: features, limitations and future developments." In: *Exp. Physiol.* 96.1 (2011), pp. 19–25 (cit. on p. 23).

[36] Klapoetke, N. C. et al. "Independent optical excitation of distinct neural populations." In: *Nat. Methods* 11.3 (2014), pp. 338–46 (cit. on p. 23).

[37] Lo, S. Q., Koh, D. X. P., Sng, J. C. G., and Augustine, G. J. "All-optical mapping of barrel cortex circuits based on simultaneous voltage-sensitive dye imaging and channelrhodopsin-mediated photostimulation." In: *Neurophotonics* 2.2 (2015), p. 021013 (cit. on p. 23).

[38] Scanziani, M. and Häusser, M. "Electrophysiology in the age of light." In: *Nature* 461.7266 (2009), pp. 930–9 (cit. on p. 23).

[39] Thorlabs. *Dual-axis scanning galvanometer*. URL: https://www.thorlabs.com/newgrouppage9.cfm?objectgroup_id=6057 (cit. on pp. 23, 24).

[40] Callamaras, N and Parker, I. "Construction of a confocal microscope for real-time x-y and x-z imaging." In: *Cell Calcium* 26.6 (1999), pp. 271–9 (cit. on p. 24).

[41] Fan, G. Y., Fujisaki, H, Miyawaki, A, Tsay, R. K., Tsien, R. Y., and Ellisman, M. H. "Video-rate scanning two-photon excitation fluorescence microscopy and ratio imaging with cameleons." In: *Biophys. J.* 76.5 (1999), pp. 2412–20 (cit. on p. 24).

[42] Cheng, A., Gonçalves, J. T., Golshani, P., Arisaka, K., and Portera-Cailliau, C. "Simultaneous two-photon calcium imaging at different depths with spatiotemporal multiplexing." In: *Nat. Methods* 8.2 (2011), pp. 139–42 (cit. on p. 24).

[43] Kim, K. H., Buehler, C, and So, P. T. "High-speed, two-photon scanning microscope." In: *Appl. Opt.* 38.28 (1999), pp. 6004–9 (cit. on p. 24).

[44] Stelzer, E. H. and Lindek, S. "Fundamental reduction of the observation volume in far-field light microscopy by detection orthogonal to the illumination axis: confocal theta microscopy." In: *Opt. Commun.* 111.5-6 (1994), pp. 536–547 (cit. on p. 24).

[45] Keller, P. J., Ahrens, M. B., and Freeman, J. "Light-sheet imaging for systems neuroscience." en. In: *Nat. Methods* 12.1 (2015), pp. 27–9 (cit. on p. 24).

[46] Ahrens, M. B., Orger, M. B., Robson, D. N., Li, J. M., and Keller, P. J. "Whole-brain functional imaging at cellular resolution using light-sheet microscopy." en. In: *Nat. Methods* 10.5 (2013), pp. 413–20 (cit. on p. 24).

[47] Vettenburg, T., Dalgarno, H. I. C., Nylk, J., Coll-Lladó, C., Ferrier, D. E. K., Čižmár, T., Gunn-Moore, F. J., and Dholakia, K. "Light-sheet microscopy using an Airy beam." In: *Nat. Methods* 11.5 (2014), pp. 541–4 (cit. on p. 24).

[48] Bouchard, M. B., Voleti, V., Mendes, C. S., Lacefield, C., Grueber, W. B., Mann, R. S., Bruno, R. M., and Hillman, E. M. C. "Swept confocally-aligned planar excitation (SCAPE) microscopy for high speed volumetric imaging of behaving organisms." In: *Nat. Photonics* 9.2 (2015), pp. 113–119 (cit. on p. 24).

[49] Göbel, W., Kampa, B. M., and Helmchen, F. "Imaging cellular network dynamics in three dimensions using fast 3D laser scanning." In: *Nat. Methods* 4.1 (2007), pp. 73–9 (cit. on p. 25).

[50] Grewe, B. F., Voigt, F. F., van 't Hoff, M., and Helmchen, F. "Fast two-layer two-photon imaging of neuronal cell populations using an electrically tunable lens." In: *Biomed. Opt. Express* 2.7 (2011), pp. 2035–46 (cit. on p. 25).

[51] Botcherby, E., Juškaitis, R., Booth, M., and Wilson, T. "An optical technique for remote focusing in microscopy." In: *Opt. Commun.* 281.4 (2008), pp. 880–887 (cit. on p. 25).

[52] Botcherby, E. J., Smith, C. W., Kohl, M. M., Débarre, D., Booth, M. J., Juškaitis, R., Paulsen, O., and Wilson, T. "Aberration-free three-dimensional multiphoton imaging of neuronal activity at kHz rates." In: *Proc. Natl. Acad. Sci. U. S. A.* 109.8 (2012), pp. 2919–24 (cit. on p. 25).

[53] Rupprecht, P., Prendergast, A., Wyart, C., and Friedrich, R. W. "Remote z-scanning with a macroscopic voice coil motor for fast 3D multiphoton laser scanning microscopy." EN. In: *Biomed. Opt. Express* 7.5 (2016), p. 1656 (cit. on p. 25).

[54] Ng, M., Roorda, R. D., Lima, S. Q., Zemelman, B. V., Morcillo, P., and Miesenböck, G. "Transmission of olfactory information between three populations of neurons in the antennal lobe of the fly." In: *Neuron* 36.3 (2002), pp. 463–74 (cit. on p. 26).

[55] Salomé, R, Kremer, Y, Dieudonné, S, Léger, J.-F., Krichevsky, O, Wyart, C, Chatenay, D, and Bourdieu, L. "Ultrafast random-access scanning in two-photon microscopy using acousto-optic deflectors." In: *J. Neurosci. Methods* 154.1-2 (2006), pp. 161–74 (cit. on p. 26).

[56] Iyer, V., Hoogland, T. M., and Saggau, P. "Fast functional imaging of single neurons using random-access multiphoton (RAMP) microscopy." In: *J. Neurophysiol.* 95.1 (2006), pp. 535–45 (cit. on p. 26).

[57] Bansal, V. and Saggau, P. "Digital micromirror devices: principles and applications in imaging." In: *Cold Spring Harb. Protoc.* 2013.5 (2013), pp. 404–11 (cit. on p. 26).

[58] Kaplan, A, Friedman, N, and Davidson, N. "Acousto-optic lens with very fast focus scanning." In: *Opt. Lett.* 26.14 (2001), pp. 1078–80 (cit. on pp. 26, 36, 37, 40, 71, 72, 109).

[59] Reddy, G. D. and Saggau, P. "Fast three-dimensional laser scanning scheme using acousto-optic deflectors." In: *J. Biomed. Opt.* 10.6 (2005), p. 064038 (cit. on pp. 26, 31, 36, 37, 71).

[60] Duemani Reddy, G., Kelleher, K., Fink, R., and Saggau, P. "Three-dimensional random access multiphoton microscopy for functional imaging of neuronal activity." In: *Nat. Neurosci.* 11.6 (2008), pp. 713–20 (cit. on pp. 26, 36, 37).

[61] Kirkby, P. A., Nadella, K. M. N. S., and Silver, R. A. "A compact acousto-optic lens for 2D and 3D femtosecond based 2-photon microscopy." In: *Opt. Express* 18.13 (2010), pp. 13721–45 (cit. on pp. 26, 28, 31, 33, 34, 37, 39–41, 44, 45, 48, 64, 68, 71, 78, 83–85, 94, 123, 131, 153, 155).

[62] Katona, G., Szalay, G., Maák, P., Kaszás, A., Veress, M., Hillier, D., Chiovini, B., Vizi, E. S., Roska, B., and Rózsa, B. "Fast two-photon in vivo imaging with three-dimensional random-access scanning in large tissue volumes." In: *Nat. Methods* 9.2 (2012), pp. 201–8 (cit. on pp. 26, 31, 34, 36, 37, 39, 45, 48, 52, 69, 71, 78, 84, 87, 90, 113).

[63] Fernández-Alfonso, T, Nadella, K. M. N. S., Iacaruso, M. F., Pichler, B, Roš, H, Kirkby, P. A., and Silver, R. A. "Monitoring synaptic and neuronal activity in 3D with synthetic and genetic indicators using a compact acousto-optic lens two-photon microscope." In: *J. Neurosci. Methods* 222 (2014), pp. 69–81 (cit. on pp. 26, 33, 34, 36, 39).

[64] Bechtold, P., Hohenstein, R., and Schmidt, M. "Beam shaping and high-speed, cylinder-lens-free beam guiding using acousto-optical deflectors without additional compensation optics." In: *Opt. Express* 21.12 (2013), pp. 14627–35 (cit. on p. 27).

[65] Akemann, W., Léger, J.-F., Ventalon, C., Mathieu, B., Dieudonné, S., and Bourdieu, L. "Fast spatial beam shaping by acousto-optic diffraction for 3D non-linear microscopy." EN. In: *Opt. Express* 23.22 (2015), p. 28191 (cit. on pp. 27, 47, 97, 115, 123, 127, 135).

[66] Collings, N., Davey, T., Christmas, J., Chu, D., and Crossland, B. "The Applications and Technology of Phase-Only Liquid Crystal on Silicon Devices." EN. In: *J. Disp. Technol.* 7.3 (2011), pp. 112–119 (cit. on p. 27).

[67] *Meadowlark Optics*. URL: http://www.meadowlark.com (cit. on p. 27).

[68] Friedman, N, Kaplan, A, and Davidson, N. "Acousto-optic scanning system with very fast nonlinear scans." In: *Opt. Lett.* 25.24 (2000), pp. 1762–4 (cit. on pp. 27, 28, 31, 42).

[69] Chen, X., Leischner, U., Varga, Z., Jia, H., Deca, D., Rochefort, N. L., and Konnerth, A. "LOTOS-based two-photon calcium imaging of dendritic spines in vivo." en. In: *Nat. Protoc.* 7.10 (2012), pp. 1818–29 (cit. on p. 28).

[70] Diebold, E. D., Buckley, B. W., Gossett, D. R., and Jalali, B. "Digitally synthesized beat frequency multiplexing for sub-millisecond fluorescence microscopy." en. In: *Nat. Photonics* 7.10 (2013), pp. 806–810 (cit. on p. 28).

[71] Ducros, M., Goulam Houssen, Y., Bradley, J., De Sars, V., and Charpak, S. "Encoded multisite two-photon microscopy." In: *Proc. Natl. Acad. Sci. U. S. A.* 110.32 (2013), pp. 13138–43 (cit. on p. 28).

[72] Kirkby, P. A., Nadella, K. M. N. S., and Silver, R. A. *Methods and Apparatus to Control Acousto-Optic Deflectors (U.S. patent WO/2012/143702)* (cit. on pp. 29, 46, 97, 115).

[73] Kong, L., Tang, J., Little, J. P., Yu, Y., Lämmermann, T., Lin, C. P., Germain, R. N., and Cui, M. "Continuous volumetric imaging via an optical phase-locked ultrasound lens." In: *Nat. Methods* 12.8 (2015), pp. 759–62 (cit. on p. 29).

[74] Griffiths, V. A. "Real-time movement correction of 3D random access multi-photon imaging in awake animals." In: *Under Prep.* (2016) (cit. on pp. 29, 122).

[75] Femtonics. *FEMTO3D-RC*. URL: http://www.femtonics.eu/products/femto3d-rc (cit. on pp. 30, 92, 145).

[76] Scientifica. *Multiphoton Imaging System*. URL: http://www.scientifica.uk.com/products/multiphoton-imaging-system (cit. on pp. 30, 92, 145).

[77] Iyer, V., Losavio, B. E., and Saggau, P. "Compensation of spatial and temporal dispersion for acousto-optic multiphoton laser-scanning microscopy." In: *J. Biomed. Opt.* 8.3 (2003), pp. 460–71 (cit. on p. 34).

[78] Chiovini, B. et al. "Dendritic spikes induce ripples in parvalbumin interneurons during hippocampal sharp waves." In: *Neuron* 82.4 (2014), pp. 908–24 (cit. on pp. 36, 39).

[79] Froudarakis, E., Berens, P., Ecker, A. S., Cotton, R. J., Sinz, F. H., Yatsenko, D., Saggau, P., Bethge, M., and Tolias, A. S. "Population code in mouse V1 facilitates readout of natural scenes through increased sparseness." In: *Nat. Neurosci.* 17.6 (2014), pp. 851–7 (cit. on pp. 36, 37).

[80] Cotton, R. J., Froudarakis, E., Storer, P., Saggau, P., and Tolias, A. S. "Three-dimensional mapping of microcircuit correlation structure." English. In: *Front. Neural Circuits* 7 (2013), p. 151 (cit. on pp. 36, 37).

[81] Walker, E., Dvornikov, A., Coblentz, K., Esener, S., and Rentzepis, P. "Toward terabyte two-photon 3D disk." In: *Opt. Express* 15.19 (2007), pp. 12264–76 (cit. on p. 36).

[82] Reddy, G. D., Cotton, R. J., Tolias, A. S., and Saggau, P. "Random-Access Multiphoton Microscopy for Fast Three-Dimensional Imaging." In: *Adv. Exp. Med. Biol.* 859 (2015), pp. 455–72 (cit. on p. 37).

[83] Warner, A. W., White, D. L., and Bonner, W. A. "Acousto-optic light deflectors using optical activity in paratellurite." In: *J. Appl. Phys.* 43.11 (1972), p. 4489 (cit. on pp. 39, 51, 52).

[84] Gordon, E. I. "A review of acoustooptical deflection and modulation devices." In: *Appl. Opt.* 5.10 (1966), pp. 1629–39 (cit. on pp. 41, 49).

[85] Xu, J. and Stroud, R. *Acousto-Optic Devices: Principles, Design, and Applications*. Wiley, 1992, p. 652 (cit. on pp. 41, 48–52, 72–74, 87).

[86] Sheppard, C. J. and Gu, M. "Aberration compensation in confocal microscopy." EN. In: *Appl. Opt.* 30.25 (1991), pp. 3563–8 (cit. on p. 45).

[87] Botcherby, E. J., Juskaitis, R., Booth, M. J., and Wilson, T. "Aberration-free optical refocusing in high numerical aperture microscopy." In: *Opt. Lett.* 32.14 (2007), p. 2007 (cit. on p. 46).

[88] Booth, M. J. "Adaptive optics in microscopy." In: *Philos. Trans. A. Math. Phys. Eng. Sci.* 365.1861 (2007), pp. 2829–43 (cit. on p. 47).

[89] Chaigneau, E., Wright, A. J., Poland, S. P., Girkin, J. M., and Silver, R. A. "Impact of wavefront distortion and scattering on 2-photon microscopy in mammalian brain tissue." EN. In: *Opt. Express* 19.23 (2011), pp. 22755–74 (cit. on p. 47).

[90] Booth, M. J. "Adaptive optical microscopy: the ongoing quest for a perfect image." In: *Light Sci. Appl.* 3.4 (2014), e165 (cit. on p. 47).

[91] Ji, N., Milkie, D. E., and Betzig, E. "Adaptive optics via pupil segmentation for high-resolution imaging in biological tissues." In: *Nat. Methods* 7.2 (2010), pp. 141–7 (cit. on p. 47).

[92] Wang, K., Milkie, D. E., Saxena, A., Engerer, P., Misgeld, T., Bronner, M. E., Mumm, J., and Betzig, E. "Rapid adaptive optical recovery of optimal resolution over large volumes." In: *Nat. Methods* 11.6 (2014), pp. 625–8 (cit. on p. 48).

[93] Yano, T. and Watanabe, A. "Acousto-optic figure of merit of TeO2 for circularly polarized light." In: *J. Appl. Phys.* 45.3 (1974), p. 1243 (cit. on pp. 48, 74).

[94] Uchida, N. "Optical properties of single-crystal paratellurite (TeO2)." In: *Phys. Rev. B* 4.10 (1971), pp. 3736–3745 (cit. on pp. 48, 73).

[95] Goutzoulis. *Design and Fabrication of Acousto-Optic Devices*. CRC Press, 1994, p. 520 (cit. on p. 49).

[96] Martynyuk-Lototska, I, Mys, O, Zapeka, B, Kostyrko, M, Grabar, A, and Vlokh, R. "Acoustic and elastic anisotropy of acousto-optic Pb2P2Se6 crystals." In: *Appl. Opt.* 53.10 (2014), B103–9 (cit. on p. 49).

[97] Chang, I. "I. Acoustooptic Devices and Applications." In: *IEEE Trans. Sonics Ultrason.* 23.1 (1976), pp. 2–21 (cit. on p. 49).

[98] Korpel, A. *Acousto-Optics*. Vol. 6. Marcel Dekker Inc, 1988 (cit. on pp. 49, 52).

[99] Born, M. and Wolf, E. *Principles of Optics: Electromagnetic Theory of Propagation, Interference and Diffraction of Light*. CUP Archive, 1999, p. 986 (cit. on pp. 50, 72).

[100] Dixon, R. "Acoustic diffraction of light in anisotropic media." In: *IEEE J. Quantum Electron.* 3.2 (1967), pp. 85–93 (cit. on p. 51).

[101] Maák, P., Jakab, L., Barócsi, A., and Richter, P. "Improved design method for acousto-optic light deflectors." In: *Opt. Commun.* 172.1-6 (1999), pp. 297–324 (cit. on pp. 52, 72–74, 84).

[102] Mihajlik, G., Barócsi, A., and Maák, P. "Complex, 3D modeling of the acousto-optical interaction and experimental verification." In: *Opt. Express* 22.9 (2014), pp. 10165–80 (cit. on pp. 52, 71, 86).

[103] Buchdahl, H. A. *An Introduction to Hamiltonian Optics*. Courier Dover Publications, 1993, p. 360 (cit. on p. 61).

[104] Chroma. *Autofluorescent Plastic Slides*. URL: https://www.chroma.com/products/accessories/92001-autofluorescent-plastic-slides (cit. on p. 65).

[105] Kirkby, P. A., Nadella, K. M. N. S., and Silver, R. A. *Methods and apparatus to control acousto-optic deflectors (WO2011131933)*. 2011 (cit. on p. 69).

[106] Alonso, M. A. "Wigner functions in optics: describing beams as ray bundles and pulses as particle ensembles." In: *Adv. Opt. Photonics* 3.4 (2011), p. 272 (cit. on p. 73).

[107] Hu, Q., Zhou, Z., Lv, X., and Zeng, S. "Compensation of spatial dispersion of an acousto-optic deflector with a special Keplerian telescope." EN. In: *Opt. Lett.* 41.2 (2016), pp. 207–10 (cit. on p. 92).

[108] Kirkby, P. A., Silver, R. A., and Nadella, K. M. N. S. *Imaging apparatus and methods*. 2014 (cit. on p. 92).

[109] Goodman, J. W. *Introduction to Fourier optics*. McGraw-Hill, 1996, p. 441 (cit. on pp. 98, 126, 154).

[110] Esser, G., Becken, W., Müller, W., Baumbach, P., Arasa, J., and Uttenweiler, D. "Derivation of the propagation equations for higher order aberrations of local wavefronts." In: *J. Opt. Soc. Am. A. Opt. Image Sci. Vis.* 28.12 (2011), pp. 2442–58 (cit. on pp. 99–102, 112).

[111] Khorasaninejad, M., Chen, W. T., Devlin, R. C., and Oh, J. "Metalenses at visible wavelengths: Diffraction-limited focusing and subwavelength resolution imaging." In: *Science* 352.6290 (2016), pp. 1190–4 (cit. on p. 112).

[112] Chen, T.-W. et al. "Ultrasensitive fluorescent proteins for imaging neuronal activity." In: *Nature* 499.7458 (2013), pp. 295–300 (cit. on p. 116).

[113] Peng, H., Ruan, Z., Long, F., Simpson, J. H., and Myers, E. W. "V3D enables real-time 3D visualization and quantitative analysis of large-scale biological image data sets." In: *Nat. Biotechnol.* 28.4 (2010), pp. 348–353 (cit. on p. 119).

[114] Poon, T.-C. and Kim, T. *Engineering Optics With Matlab*. World Scientific Publishing Company Incorporated, 2006, p. 249 (cit. on pp. 129, 130).

[115] Plachenov, A. B., Kudashov, V. N., and Radin, A. M. "Simple formula for a Gaussian beam with general astigmatism in a homogeneous medium." In: *Opt. Spectrosc.* 106.6 (2009), pp. 910–912 (cit. on p. 130).

COLOPHON

This document was typeset using the typographical look-and-feel `classicthesis` developed by André Miede. The style was inspired by Robert Bringhurst's seminal book on typography *"The Elements of Typographic Style"*. `classicthesis` is available for both LaTeX and LyX:

https://bitbucket.org/amiede/classicthesis/

Final Version as of October 15, 2016 (`classicthesis`).